Exploring Exotic Atomic and Molecular Collisions at Ultracold Temperatures

by

Brandon P. Ruzic

B.A., University of Illinois, 2009

M.S., University of Colorado, 2012

A thesis submitted to the

Faculty of the Graduate School of the

University of Colorado in partial fulfillment

of the requirements for the degree of

Doctor of Philosophy

Department of Physics

2015

This thesis entitled:
Exploring Exotic Atomic and Molecular Collisions at Ultracold Temperatures
written by Brandon P. Ruzic
has been approved for the Department of Physics

John Bohn

Murray Holland

Date

The final copy of this thesis has been examined by the signatories, and we find that both the content and the form meet acceptable presentation standards of scholarly work in the above mentioned discipline.

Ruzic, Brandon P. (Ph.D., Physics)

Exploring Exotic Atomic and Molecular Collisions at Ultracold Temperatures

Thesis directed by Prof. John Bohn

New experimental techniques have increased the scope of atomic and molecular control at ultracold temperatures. To understand molecular collisions and collisions between atoms with large electronic spin, we extend multichannel quantum defect theory to describe scattering in the case of high-partial-wave angular momentum and long-range anisotropic interactions. The efficiency and accuracy of these calculations facilitate the prediction and characterization of Fano-Feshbach resonances.

Dedication

To my family

Acknowledgements

The completion of this thesis would not have been possible without the support of many people. First and foremost, I would like to thank my advisor, John Bohn. I deeply appreciate the time that he has devoted to my education and growth as a physicist. He truly has a unique combination of patience, creativity, rigor, and enthusiasm that I have been incredibly lucky to enjoy. I sincerely hope our work together is only beginning.

The collaboration between theorists at JILA has been a great pleasure for me. I would like to thank Chris Greene for many helpful discussions and productive collaborations. I have found that most of my scientific conversations with him have directly led to a significant advancement of my research. I also appreciate all of the times that Murray Holland has made my time at JILA more enjoyable through his participation in social activities.

I have enjoyed getting to know many postdoctoral students from whom I have learned a great deal. In particular, I would like to mention Goulven Quéméner, Michael Mayle, James Croft, and Andrew Sykes.

The work presented in chapter 5 of this thesis was performed in close collaboration with Jisha Hazra and Balakrishnan Naduvalath. I value their hard work on the application of multichannel quantum defect theory to molecular collisions, which would not have been possible without them.

For their careful review of my thesis, I thank my thesis committee: Murray Holland, Deborah Jin, Michael Ritzwoller, and Robert Parson.

Last but not least, I am especially grateful for the love and support of my family.

Contents

Chapter

Tables

Table

Figures

Figure

Chapter 1

Introduction

"The further a mathematical theory is developed, the more harmoniously and uniformly does its construction proceed, and unsuspected relations are disclosed between hitherto separated branches of the science.

David Hilbert

1.1 Prologue

In the 4th century B.C., Plato advocated that celestial motion was flawless and, therefore, uniform circular motion could explain all motion in the cosmos through the "Spindle of Necessity" [1]. Plato's sketch of this spindle had eight perfectly circular rings that carried the moon, the sun, the five known planets, and the distant stars around the Earth. The Earth was in the center of the spindle, and divine forces turned its rings, sending the celestial bodies twirling around the Earth, which was at the center of the universe. Plato knew that his simple sketch of the spindle could not adequately describe all celestial motion. Most notably, the planets would occasionally deviate from their steady journeys across the night's sky and exhibit retrograde motion. Plato posed the problem of finding an accurate model of celestial motion that only used uniform circular motion to his contemporary astronomers [2].

Consistent with Plato's pristine picture of the cosmos, Eudoxus of Cnidus developed the first mathematical description of celestial motion [2]. In his model, the celestial bodies were attached to concentric spheres that rotated with constant angular velocities, and the Earth was at the

center of each sphere. This model could explain the vast majority of celestial motion, including the retrograde motion of the planets. He accomplished this by using several concentric spheres to describe the orbit of each celestial body around the Earth. Each celestial body was fixed to a single rotating sphere; the poles of this sphere were attached to a larger concentric sphere that rotated at a different velocity; the poles of that sphere were attached to yet another larger sphere; and so on [3].

However, the apparent brightness of the planets would change, and the Eudoxan model could not account for this because each planet was attached to a sphere with a constant radius. To account for the changing glow of the planets, the ancient astronomers allowed for a minor defect in the Platonic view of planetary motion, suggesting that the planets would slightly deviate from their trajectories described by rotating spheres. Apollonius of Perga eventually created a model in which the planets mainly followed a path described by rotating spheres, but the planets also took additional smaller circular orbits, called epicycles, that were centered on the rotating spheres [2]. These additional orbits were not centered on Earth, allowing the planets to move in the radial direction and change their apparent brightness. In 152 AD, the astronomer Ptolemy used the idea of epicycles to create an accurate model of celestial motion [4]. The necessary complications of this model had brought the notion of flawless celestial motion into question, but the model maintained Plato's original concepts of circular motion and a geocentric view of the universe. Due to the inability of astronomers to make better observations, this model was generally accepted for nearly two millennia [4].

1.2 Discovery of the Quantum Defect

The ancient astronomers taught us that small alterations to physical models could accurately describe observations, without tossing aside the concepts behind the model. The study of atomic and molecular collisions has been no exception to this lesson. A particularly useful example of such an alteration was the quantum defect, and the modern quantum defect has shown a great ability to clarify and numerically simplify an enormous variety of complex collisions. The concept of a

quantum defect came from the semi-classical formulation of quantum mechanics, also known as the "old quantum theory." Niels Bohr and Arnold Sommerfield created an exceptionally accurate model of the hydrogen atom, including its fine structure [5]. However, it was not immediately clear how to extend their model to describe the spectra of atoms with more than one electron. Erwin Schrödinger discovered that he could approximately describe the energy levels of these atoms by allowing the trajectory of an electron in an atom to deviate from its path described by the Bohr-Sommerfield model and then quickly return [6]. He described this deviation in terms of a quantum defect.

In 1913, well before the formulation of modern quantum mechanics, Bohr conjectured a simple model of the atom that was reminiscent of Plato's spindle. In Bohr's model of the atom, the electrons traveled around the nucleus in perfect circles [7, 8], like the rings of Plato's spindle, and these orbits were only allowed to have specific radii. Rutherford had recently fired alpha particles at a sheet of gold foil and discovered that the atom was mostly empty space with a heavy, positively charged nucleus, suggesting that the lighter, negatively charged electrons were orbiting around the nucleus like the planets around the sun [9]. Knowing that these accelerating electrons would emit radiation and quickly collapse into the nucleus, Bohr posited that the electrons occupied stationary states of circular motion and would only emit radiation by jumping between two of these states. He further posited that these states only occurred when the electron's angular momentum was an integer multiple of Planck's constant $\hbar = h/2\pi$. Using these laws, Bohr derived a formula for the energy levels of the hydrogen atom that was in remarkable agreement with the empirical Rydberg series [5],

$$E_n = -R_{\mathrm{H}} hc/n^2, \tag{1.1}$$

where R_{H} is the Rydberg constant, c is the speed of light, and n is an integer $n \geq 1$ that specifies the electron's quantized angular momentum $n\hbar$.

Despite the ability of Bohr's model to describe the Rydberg series of hydrogen and even all hydrogenic ions by including the nuclear charge Z, this model could not describe the fainter fine

structure spectral lines of hydrogen that had already been discovered by Michelson and Morley in 1887. In the years 1915 and 1916, Sommerfield offered an extension of Bohr's model that was able to produce this fine structure by allowing the electrons to move in the radial direction [5]. In his model, the electrons took elliptical orbits around the nucleus, further relating the structure of the atom to the solar system. Instead of simply quantizing angular momentum, these elliptical orbits required the classical action of an electron's orbit around the nucleus to be quantized. In polar coordinates (ϕ,ρ), the integral of an electron's generalized momentum (p_ϕ, p_ρ) over a closed loop around the nucleus had to be equal to an integer (n,n') multiple of $\hbar$. This so called "Bohr-Sommerfield quantization" produced the following allowed energy levels [5],

$$E_{nn'} = -R_{\mathrm{H}}hcZ^2\left(1-\epsilon^2\right)/n^2 \tag{1.2a}$$

$$= -R_{\mathrm{H}}hcZ^2/(n+n')^2, \tag{1.2b}$$

where $\epsilon = \sqrt{1-n^2/(n+n')^2}$ was the eccentricity of the electron's orbit, and the integer n' was in the range $0 \leq n' < n$. When $n' = 0$, the electron's orbit was a circle.

Because the energy levels of hydrogen in Sommerfield's model only depended on the sum of n and n', as seen in equation (1.2b), the elliptical orbits maintained the same discrete spectrum of hydrogen as the circular orbits in Bohr's model, which produced the energy levels in equation (1.1). Additionally, Sommerfield derived a relativistic correction to these energy levels by allowing the perihelion of the elliptical orbits to precess around the nucleus and by including Einstein's relativistic effects [5],

$$E_{nn'} = -\frac{R_{\mathrm{H}}hcZ^2}{n^2}\left(1+\frac{\alpha^2Z^2}{n^2}\left(\frac{n}{n-n'}-\frac{3}{4}\right)\right), \tag{1.3}$$

where α is the fine structure constant. These energy levels accurately described the fine structure of hydrogen by making a small correction to the energy levels in Bohr's model. This correction depended on the value of n' and, therefore, the shape of the electron's orbit.

However, because the Bohr-Sommerfield model did not account for interactions between electrons, it was essentially a model of only the hydrogen atom and hydrogenic ions, which only

have one remaining electron. In 1921, Schrödinger discovered an approximate way to describe more complex atoms in terms of a quantum defect Δ and an effective quantum number $n^* = n + n' - \Delta$ that was not an integer [6]. Using the Bohr-Sommerfield model of the atom, Schrödinger divided the path of an electron around the nucleus into a long-range region and a short-range region. He suggested that an electron at long range was almost entirely screened from the nuclear charge by the other electrons that were in a small region around the nucleus. At long range, an electron followed an orbit of eccentricity ϵ and with the energy in equation (1.2b) with $Z = 1$, but when the electron came close to the nucleus it would deviate from its trajectory and quickly take an additional tighter path around the nucleus with eccentricity ϵ', experiencing the full nuclear charge Z. After completing the tighter path, the electron was flung back out onto its original trajectory, completing the full loop. A similar description of electrons penetrating the atomic core was also given by Bohr around the same time [10].

Schrödinger used this distorted trajectory of an electron to approximate a value of Δ, which was dependent on Z [6]. The effective quantum number n^* implied the following energy levels of an atom,

$$E_{nn'} = -R_{\mathrm{H}} hc / \left(n + n' - \Delta\right)^2 . \tag{1.4}$$

Schrödinger called Δ the "Quantendefekt" in German [6]. This translates to "quantum defect" in English, and he was the first to use this term [11]. Although he only considered $n' \gtrsim 1$, excluding circular orbits ($n' = 0$), he found that the value of Δ was independent of n'. For sodium, he predicted a value of $\Delta \approx .74$, corresponding to a value of $n' - \Delta \approx 1.26$ for $n' = 1$. The number 1.26 was a surprisingly good approximation to what would soon after become known as the s-wave ($l = 0$) quantum defect of sodium $\mu_{(l=0)} = 1.35$ [11].

Guided by these semi-classical models and the high-resolution spectroscopy of atoms, Schrödinger developed a quantum theory of wave mechanics in 1925 [12] and helped formulate modern quantum mechanics. The concept of a quantum defect remained. In light of modern quantum mechanics, it became clear that the valence electrons in atoms have some probability of being inside the atomic

core and that this probability decreases with increasing orbital angular momentum l. The quantum defect μ_l (in modern notation) is simply related to the short-range phase shift $\delta_l = \mu_l \pi$ that an electron accumulates by penetrating into the atomic core, in addition to the long-range phase shift of the Coulomb potential [11]. Hence, the quantum defect is largest for s-wave states ($l = 0$). This concept is widely applicable to the field of atomic physics, and perhaps the most well-known use of the quantum defect is to approximately describe the energy levels of a hydrogenic atom, such as an alkali atom, which has a single electron in its valence shell [11],

$$E_{nl} = -R_{\mathrm{H}} hc/(n - \mu_l)^2, \tag{1.5}$$

where the quantum defect μ_l takes the place of $\Delta - n'$ in equation (1.5).

1.3 Quantum Defect Theory

The key principle behind the quantum defect was Schrödinger's idea of separating the complex short-range physics from the far simpler long-range physics. In 1928, Douglas Hartree laid the foundation for modern quantum defect theory (QDT) [13]. He solved the radial Schrödinger equation for an electron in an alkali atom that was screened from the nuclear charge by a spherical charge distribution of radius r_0. Inside this region, he normalized the inner wave function in a way that was insensitive to small changes in energy. Outside this region, he used the analytically known solutions to the Coulomb potential. Matching these solutions together at r_0, he derived equation (1.5) from the long-range properties of the Coulomb solutions. In the following decades, much interest was generated in QDT through studies that took advantage of the analytically known Coulomb solutions. The work of Bates and Damgaard in 1949 [14] used QDT to provide a powerful method of computing bound to bound transitions in atomic systems, and the work of Burgess and Seaton in 1960 [15] used QDT to explore photoionization in atomic systems.

The work of Gailitis [16] in 1963 considered multiple states of the ionic core and developed a multichannel quantum defect theory (MQDT) that could describe a more elaborate energy dependence than the simple expression in equation (1.5), including atoms with open shells in the

ionic core and scattering resonances. Since the introduction of MQDT, it was extensively developed for the analysis of complex atomic spectra by Ham, Seaton, Fano, and Rau [17–19]. In such multichannel situations the radial Schrödinger equation is replaced by a series of N coupled radial Schrödinger equations, where N is the number of channels. The coupling between weakly bound or quasi-bound states and scattering states allows for sharp scattering resonances, known as Fano-Feshbach resonances. As an aside, the basic treatment of how a bound state autoionizes into a degenerate continuum was first developed by Rice in 1933 [20], and the asymmetry of the resulting spectral line shape was first described by Fano in 1935 [21]. Fano and Feshbach separately elaborated on the description of these resonances around 1960 [22,23], leading to the current name for these so called Fano-Feshbach resonances (FRs).

In the 1970's, the work of Fano [24,25] first generalized MQDT to describe the electronic spectra of molecules, and the work of Jungen explored applications to molecular problems as well [26]. The work of Greene et al. in 1979 [27] made further generalizations of MQDT, breaking away from only using the typical Coulomb potential. This work applied MQDT to problems with $1/r^2$ long-range potentials and problems with no long-range potentials, in addition to the Coulomb potential. These generalizations continued in the 1980's through the works of Greene, Fano, Rau, Mies, Julienne, and Jungen [19, 28–33], who used the generalized form of MQDT to successfully describe, for example, the dipole interaction between an electron or an ion with a polar molecule, the polarization interaction between an electron or an ion with an atom, and the van der Waals interaction between atoms or molecules. More recently, Greene, Bohn, Raoult, Gao, and Hutson (among many others) have fruitfully applied MQDT to atomic and molecular collisions [34–36], and, in particular, cold collisions [37–39].

1.4 Cold Collisions

Today, the constituents of cold gaseous matter continue to grow in variety and complexity far beyond their origins in alkali atoms to encompass open shell atoms, molecules, free radicals, and ions [40]. A detailed understanding of their collision processes is crucial in determining the

properties of these gases and in finding prospects for control of these gases.

However, along with the growing complexity of the atoms and molecules involved, the difficulty of accurate scattering calculations grows as well. High-spin and open-shell atoms contain a multiplicity of internal states, and molecules incorporate rotational and vibrational degrees of freedom. At ultralow temperatures, all of these degrees of freedom must be accounted for because they all describe energies that are typically large compared to translational kinetic energies in the gas. Moreover, anisotropic species are likely to involve angular momentum partial waves far larger than the single value $L = 0$ that often dominates alkali-atom cold collisions. These considerations can lead to enormous complexity, even in seemingly straightforward problems. Consider for example the scattering of Li atoms with ground state Li_2 molecules, which necessitates the simultaneous solution of thousands of coupled Schrödinger equations [41].

It is therefore worthwhile to explore alternative methods of scattering theory that are less computationally intensive, yet still accurate. MQDT is a particularly appealing candidate for this purpose, as it takes into account the natural separation of length and energy scales in a collision problem. In the same that way Schrödinger discovered the quantum defect in 1921, modern MQDT separates the collision problem into a short-range region and a long-range region. At large internuclear separations R, the sensitive dependence of scattering observables on energy and electric or magnetic fields arises from relatively simple interactions between the colliding partners. This simplicity stems from the ability to describe these sensitive dependences using a separate set of reference wave functions for each set of quantum numbers that identify a scattering channel. One can either analytically solve this part of the problem or very quickly produce numerical solutions. At small R, strong coupling between channels demands that all channels are dealt with at once, leading to a numerically challenging and slow part of the calculation. However, in this region, the energy scales driving the physics are far larger than the μK – mK scale of cold collisions. A properly chosen representation of the small-R wave function can then be quite weakly energy dependent over the relevant scales, allowing for simple interpolation in energy and field that greatly reduces computational time.

In recent years, various approaches have been applied to cold collisions with an aim of describing and predicting scattering observables and, in particular, the locations and widths of Fano-Feshbach resonances. For example, recent developments in MQDT and related ideas have stressed the simplicity and analytic behavior of the theory [34, 42–49]. Also, the analysis of long-range s-wave solutions, developed in reference [50], resembles quantum defect ideas to a degree. This analysis adopts semiclassical ideas and creates a good approximation to the long-range field solutions. In parallel developments, the asymptotic bound state method stresses a direct numerical diagonalization in a basis of singlet and triplet states that are coupled by hyperfine and magnetic interactions [51–53]. This method has generated extremely rapid and accurate numerical calculations in these cases.

1.5 Outline

The work presented in this thesis describes a version of MQDT that is easy to implement and that accurately describes scattering calculations, gaining both numerical efficiency and conceptual insights over other types of calculations. Chapters 2 and 3 develop the theoretical framework of this work. In chapter 2, we define a standardization of MQDT that allows the long-range QDT parameters to be independent of the short-range interactions, and we derive analytic expressions for the threshold behavior of these parameters. This unique standardization ensures that the numerically computed reference wave functions are maximally linearly independent at long-range, even in the case of high partial waves, where a large classically forbidden region at ultracold collision energies can cause the numerical reference wave functions to lose their linear independence. In chapter 3, we extend MQDT to incorporate long-range anisotropic interactions that are typically ignored in applications of MQDT. We accomplish this by using a unique distorted wave approximation that generates perturbed scattering observables in terms of parameters that are weakly dependent on energy and field, retaining the accuracy and the numerical efficiency of MQDT.

Chapters 4 and 5 provide examples of our formulation of MQDT. These examples illustrate the accuracy and efficiency of MQDT and our extensions of the method. Simultaneously, these

examples explore the properties of exotic atomic and molecular cold collisions. In chapter 4, we use alkali-atom collisions as a test bed for this formulation of MQDT, and we explore a few examples of alkali-atom collisions in detail, providing an extensive characterization of Fano-Feshbach resonances in these systems. We also demonstrate the principles of the perturbative MQDT method in this chapter, and we explore the ability of the perturbative MQDT method to incorporate the effects of strong magnetic dipole-dipole interactions. In chapter 5, we provide the modifications to MQDT that cold molecular scattering and cold chemistry require. As an example, we apply this method to non-reactive and reactive molecular collisions. We demonstrate that the efficiency and some conceptual simplifications of atomic MQDT carry over to the case of molecular scattering.

Chapter 2

Multichannel Quantum Defect Theory

This chapter contains material in reference [54].

2.1 Introduction

This chapter describes how to retain the analytic structure of Multichannel Quantum Defect Theory (MQDT) and simultaneously perform numerically exact scattering calculations. On the one hand, MQDT describes both the long-range physics and the short-range physics in terms of simple parameters. We derive analytic expressions for the long-range parameters in the limit of small collision energy, and the short-range parameters are nearly independent of energy and field. This treatment of the short-range physics eschews a repeated numerical calculation of the short-range wave functions and, therefore, leads to numerically efficient scattering calculations. On the other hand, our implementation of MQDT is numerically exact, even in the case of realistic long-range potentials that are not purely of $-C_6/R^6$ character and that possess high centrifugal angular momentum.

The accuracy of MQDT relies on the availability of a pair of accurate, linearly independent reference wave functions in each channel. Generating these wave functions can become problematic in cases of high partial wave angular momentum and extremely low collision energy, where there exists a substantial region of classically forbidden motion under a centrifugal barrier. Such a barrier is problematic because two reference wave functions that are perfectly linearly independent prior to entering the barrier can often become approximately linearly dependent (hence useless to the

theory) under and beyond this barrier. Previously, defining an additional set of linearly independent reference wave functions beyond a classical barrier has allowed for this type of difficulty to be reduced by matching the two sets of reference wave functions under the barrier [37, 55, 56].

Our main focus here is to determine reference wave functions in a way that maximizes their linear independence, even under the centrifugal barrier, and to develop an MQDT method in terms of these reference wave functions. In chapter 4, we apply this method to the scattering of alkali atoms for which reasonably accurate Hamiltonians exist. The long-range interactions in these systems include contributions from C_8/R^8 and C_{10}/R^{10} in addition to the usual C_6/R^6. MQDT reproduces the full numerical calculation of scattering observables quite accurately with orders of magnitude less computational effort. In particular, this version of MQDT accurately reproduces magnetic field Fano-Feshbach resonances, even those that reside in high-partial-wave states.

2.2 Scattering in the MQDT Picture

Two colliding atoms or molecules experience the potential energy $V(R)$, where R is the internuclear separation and $V(R)$ is an operator that includes spin. We expand the wave function in a basis of scattering channels that correspond to the internal states of the particles and their partial-wave quantum number L,

$$\psi(R,\Omega) = R^{-1}\sum_{i=1}^{N}\Phi_i(\Omega)\psi_i(R). \tag{2.1}$$

The symbol Ω represents all angular coordinates and internal degrees of freedom. The index i labels the scattering channels, and N is the number of channels. This wave function satisfies a set of coupled radial Schrödinger equations involving the full potential matrix $V(R)$,

$$\sum_{j=1}^{N}\left[\left(-\frac{\mathrm{d}^2}{\mathrm{d}R^2}+\frac{L_j(L_j+1)}{R^2}\right)\delta_{ij}+V_{ij}(R)\right]\psi_j^{(\alpha)}(R) = E_i\psi_i^{(\alpha)}(R), \tag{2.2}$$

where $E_i = E - E_i^{\mathrm{thresh}}$ is the asymptotic kinetic energy in channel i, E is the total energy, and E_i^{thresh} is the threshold energy of the i-th channel. The collision energy is the asymptotic kinetic energy in the incident channel $E_{i=\mathrm{inc}} = E - E_{i=\mathrm{inc}}^{\mathrm{thresh}}$. The symbol δ_{ij} is the Kronecker delta function.

The superscript α labels linearly independent solutions to equation (2.2) at a total energy E. Here and throughout the rest of this thesis (unless otherwise specified), R is in units of β, and all energies are in units of $E_\beta = \hbar^2/2\mu\beta^2$, where μ is the reduced mass. The form of $V(R)$ at long range suggests the value of β through the relation $-\hbar^2/2\mu\beta^2 = V_{ii}(\beta)$ for a convenient channel i.

For example, in the collision of ^{40}K + ^{87}Rb, which we discuss in later sections, the isotropic potential $-C_6/R^6$ accurately characterizes $V(R)$ at long range. The natural unit of length is the van der Waals length $\beta = (2\mu C_6/\hbar^2)^{1/4} = 143.9\ a_0$, and $E_\beta = 152.7\ \mu$K, where a_0 is the Bohr radius. In this example, we only consider collisions between s-wave atoms, which both have zero internal orbital angular momentum $\vec{l} = 0$. We describe each atom by its electronic spin $\vec{s}$ and by its nuclear spin $\vec{i}$. We choose the scattering-channel basis $|f_{\rm K}, m_{f_{\rm K}}\rangle\,|f_{\rm Rb}, m_{f_{\rm Rb}}\rangle\,|L, M_L\rangle$, where $\vec{f} = \vec{s} + \vec{i}$ is the total spin of each atom. In the presence of an external magnetic field, the scattering channels are eigenstates of the following Hamiltonian,

$$H^{\rm thresh} = \sum_{j=1}^{2} A_j \vec{s}_j \cdot \vec{i}_j + (g_{s,j} s_{z,j} + g_{i,j} i_{z,j})\,\mu_{\rm B} B, \tag{2.3}$$

which includes the hyperfine interaction and the Zeeman interaction with an external magnetic field $\vec{B} = B\hat{z}$. The threshold energies $E_i^{\rm thresh}$ are the eigenvalues of $H^{\rm thresh}$. The index j labels the two atoms, A is the hyperfine constant, g_s is the electronic gyromagnetic ratio, g_i is the nuclear gyromagnetic ratio, and $\mu_{\rm B}$ is the Bohr magneton. We find it convenient to choose the zero of energy such that $E_{i=\rm inc}^{\rm thresh} = 0$, causing the collision energy to equal the total energy.

When the total energy E is greater than the lowest threshold energy, a continuum of physical scattering solutions exists. One can calculate scattering observables at E by solving equation (2.2) subject to physical scattering boundary conditions. A physical scattering solution at E vanishes at the origin in all channels and asymptotically vanishes in all closed channels. The i-th channel is said to be closed if it has a negative asymptotic kinetic energy $E_i < 0$. Conversely, the i-th channel is said to be open if $E_i \geq 0$. For a given total energy E, there are $N_{\rm o}$ open channels, and there are $N_{\rm o}$ linearly independent physical scattering solutions to equation (2.2).

We represent a particular set of physical scattering solutions by the matrix $\Psi_{ij}(R) = \psi_i^{(j)}(R)$,

where i runs from 1 to N and j runs from 1 to N_o. Hence, the columns of $\Psi(R)$ represent N_o linearly independent wave functions with energy E, and each row of $\Psi(R)$ corresponds to a unique channel. In each channel i, $\Psi(R)$ has the following boundary conditions at $R = 0$,

$$\Psi_{ij}(0) = 0. \tag{2.4}$$

Asymptotically, $\Psi(R)$ has the following, standard boundary conditions. In each open channel i,

$$\Psi_{ij}(R) \xrightarrow{R\to\infty} \frac{1}{2i\sqrt{k_i}} \left(e^{-i(k_i R - L_i \pi/2)} \delta_{ij} - e^{i(k_i R - L_i \pi/2)} S^{\mathrm{phys}}_{ij} \right), \tag{2.5}$$

where $k_i = \sqrt{E_i}$. In each closed channel i,

$$\Psi_{ij}(R) \xrightarrow{R\to\infty} 0. \tag{2.6}$$

This set of equations defines the physical scattering matrix S^{phys}, which contains all the information necessary to compute scattering observables, including resonance behavior and threshold effects. As an aside, when the total energy E is less than the lowest threshold energy, physical solutions only exist at a set of total energies E_λ that correspond to bound state wave functions. At a bound state energy E_λ, there are zero open channels, and the bound state wave function has the boundary conditions in the set of equations (2.4) and (2.6) in all channels.

One accurate way to determine S^{phys} is the full-close coupling (FCC) method. The $N \times N$ log-derivative matrix $Y(R) = \frac{\mathrm{d}\Psi(R)}{\mathrm{d}R}\Psi^{-1}(R)$ represents the log-derivative of N linearly independent solutions to equation (2.2) that have vanishing boundary conditions at the origin. This matrix has the boundary conditions $Y_{ij}(R) \to \infty\delta_{ij}$ in the limit $R \to 0$. Numerically, we achieve the $R \to 0$ boundary conditions on $Y(R)$ by simply filling the diagonal elements of $Y(R)$ with the same very large number and by filling the off-diagonal elements of $Y(R)$ with zero at $R \approx 0$. The FCC calculation propagates $Y(R)$ from $R \approx 0$ to the limit $R \to \infty$, and the open channels of $Y(\infty)$ describe the standard, physical scattering matrix S^{phys}. This calculation is a numerically accurate method of solving the scattering problem; however, it also tends to be quite time-consuming for large N, as the computational time scales as N^3 [57].

MQDT offers a more efficient way to determine S^{phys}. Beyond some intermediate distance R_{m}, MQDT breaks the full potential $V(R)$ into two parts: an isotropic long-range potential $V^{\text{lr}}(R)$ and the remaining potential $V'(R)$,

$$V_{ij}(R) = V^{\text{lr}}(R)\delta_{ij} + V'_{ij}(R). \tag{2.7}$$

For many problems, such as atoms and molecules interacting via van der Waals potentials, the coupling between channels of $V(R)$ is weak beyond R_{m}, and the potential $V'(R)$ makes a relatively small contribution. The value of R_{m} and the form of $V^{\text{lr}}(R)$ depend on the scattering partners. For non-polar atoms and molecules, the long-range potential takes the form,

$$V^{\text{lr}}(R) = -C_6/R^6 - C_8/R^8 - C_{10}/R^{10}. \tag{2.8}$$

For alkali-atom collisions, $V^{\text{lr}}(R)$ is typically a good approximation to the full potential beyond $R_{\text{m}} \approx 30 - 50\ a_0$.

The primary goal of MQDT is to represent S^{phys} in terms of a set of parameters that are smooth in energy and applied fields. This allows for the efficient calculation of narrow scattering features by interpolating the smooth parameters instead of performing a separate calculation at every energy and field of interest. MQDT achieves this representation of S^{phys} by separately describing the short-range physics and the long-range physics of the scattering problem.

2.2.1 Reference Wave Functions and the Short-range K-matrix

In the region $R \leq R_{\text{m}}$, we describe the short-range physics by giving the log-derivative matrix $Y(R) = \frac{\mathrm{d}\Psi(R)}{\mathrm{d}R}\Psi^{-1}(R)$ the same boundary conditions near the origin as in the FCC calculation, such that $Y(R)$ represents the log-derivative of N independent solutions to equation (2.2) with vanishing boundary conditions at the origin. Unlike the FCC calculation, we do not propagate $Y(R)$ to the limit $R \to \infty$. We only propagate $Y(R)$ up to R_{m}. Beyond R_{m}, we describe the long-range physics by taking advantage of the simple form of the potential energy $V(R)$ when $V'(R) = 0$. In this case, equation (2.2) reduces to the single-channel radial Schrödinger equation involving the

long-range isotropic reference potential $V^{\rm lr}(R)$,

$$\left(-\frac{\mathrm{d}^2}{\mathrm{d}R^2}+\frac{L_i(L_i+1)}{R^2}+V^{\rm lr}(R)-E_i\right)\left\{\begin{array}{c}\hat{f}_i(R)\\ \\ \hat{g}_i(R)\end{array}\right\}=0, \tag{2.9}$$

where $\hat{f}(R)$ and $\hat{g}(R)$ are two linearly independent single-channel reference wave functions. As long as $\hat{f}(R)$ and $\hat{g}(R)$ are linearly independent, we can represent any long-range solution as a linear combination of these reference wave functions.

At the matching radius $R_{\rm m}$, we match the short-range solutions and the long-range solutions together. We accomplish this matching by defining a wave function matrix $M(R)$ that has the log-derivative boundary condition $Y(R)=\frac{\mathrm{d}M(R)}{\mathrm{d}R}M^{-1}(R)$ at $R_{\rm m}$. This boundary condition allows $M(R)$ to vanish at the origin in all channels, regardless of the normalization we choose for $M(R)$. We represent $M(R)$ at $R\geq R_{\rm m}$ as a linear combination of the reference wave functions $\hat{f}(R)$ and $\hat{g}(R)$,

$$M_{ij}(R)=\hat{f}_i(R)\delta_{ij}-\hat{g}_i(R)K^{\rm sr}_{ij}. \tag{2.10}$$

This equation defines the $N\times N$ matrix $K^{\rm sr}$. Since we have the freedom to choose a particular normalization of $M(R)$ without changing its log-derivative at $R_{\rm m}$, we force the coefficient in front of $\hat{f}(R)$ in equation (2.10) to equal the $N\times N$ identity matrix so that $M(R)$ has the same normalization as $\hat{f}(R)$ at $R_{\rm m}$.

Tying together the normalization of $M(R)$ and $\hat{f}(R)$ allows us to optimally design the smoothness of $K^{\rm sr}$ in energy and field by choosing the boundary conditions of $\hat{f}(R)$ and $\hat{g}(R)$. We choose to give these reference wave functions a WKB-like normalization at $R_{\rm x}<<1$ [28, 29, 34],

$$\hat{f}_i(R)=\frac{1}{\sqrt{k_i(R)}}\sin(\int_{R_{\rm x}}^{R}k_i(R')\mathrm{d}R'+\phi_i)\quad\text{at } R=R_{\rm x} \tag{2.11a}$$

$$\hat{g}_i(R)=-\frac{1}{\sqrt{k_i(R)}}\cos(\int_{R_{\rm x}}^{R}k_i(R')\mathrm{d}R'+\phi_i)\quad\text{at } R=R_{\rm x}, \tag{2.11b}$$

where $k_i(R)=\sqrt{E_i-V^{\rm lr}(R)}$. The set of equations (2.11) and their full radial first-derivatives define $\hat{f}(R)$ and $\hat{g}(R)$. We obtain these reference wave functions by numerically solving equation (2.9) subject to these boundary conditions.

We define the channel-dependent phase ϕ_i at $R_{\rm x}$, and we discuss the choice of this phase in detail in section 2.4. We must choose the location $R_{\rm x}$ to be small enough such that the asymptotically closed channels are locally open at $R_{\rm x}$ in the reference potential $V^{\rm lr}(R)$. A channel is said to be locally open at R when the kinetic energy in the channel is positive at R. In this case, the kinetic energy $E_i - V^{\rm lr}(R_{\rm x})$ must be greater than zero in all channels, allowing one to use the WKB-like boundary conditions in the set of equations (2.11). The choice of $R_{\rm x} = 0.1$ allows a range of E_i that is suitable for typical ultracold alkali-atom collisions.

In order to determine $K^{\rm sr}$, we numerically propagate $\hat{f}(R)$ and $\hat{g}(R)$ from their boundary conditions at $R_{\rm x}$ to the location $R_{\rm m}$. We choose $R_{\rm m}$ at a location where all channels of $V(R)$ remain locally open. At such a location, the colliding atoms or molecules have a large kinetic energy that dominates the small collision energies of ultracold scattering. This kinetic energy also dominates the typical Zeeman (Stark) energy shift due to an applied magnetic (electric) field. Since the WKB-like normalization depends on the local wave vector $k_i(R)$ in each channel i, the reference wave functions, and therefore $M(R)$, are weakly dependent on energy and applied fields at $R_{\rm m}$. Moreover, these wave functions are energy-analytic across threshold. Ideally, this gives $K^{\rm sr}$ a weak dependence on energy and field as well, even when a channel crosses threshold. We show examples of $K^{\rm sr}$ as a function of energy and field in chapters 4 and 5.

Using our representation of $M(R)$ in terms of $\hat{f}(R)$ and $\hat{g}(R)$ in equation (2.10), we match the log-derivative of $M(R)$ to $Y(R)$ at $R_{\rm m}$ and solve for $K^{\rm sr}$,

$$K^{\rm sr} = \left(Y(R)\hat{g}(R) - \frac{{\rm d}\hat{g}(R)}{{\rm d}R} \right)^{-1} \left(Y(R)\hat{f}(R) - \frac{{\rm d}\hat{f}(R)}{{\rm d}R} \right) \Bigg|_{R=R_{\rm m}} . \tag{2.12}$$

We use this equation to numerically determine $K^{\rm sr}$. In equation (2.12) we promote $\hat{f}(R)$ and $\hat{g}(R)$ to $N \times N$ diagonal matrices.

2.2.2 The QDT Parameters

The matrix $K^{\rm sr}$ and the linearly independent reference wave functions $\hat{f}(R)$ and $\hat{g}(R)$ contain all the information necessary to calculate scattering observables. The quantum defect theory of

reference [34] defines the four QDT parameters η, $\mathcal{A}$, $\mathcal{G}$, and $\beta_{\rm QDT}$ that describe the asymptotic behavior of the wave functions $\hat{f}(R)$ and $\hat{g}(R)$. These parameters are weakly dependent on energy and field and completely describe the long-range physics. The notation in this thesis only differs from the notation of reference [34] by the use of γ instead of $\beta_{\rm QDT}$, where $\cot\gamma = \tan\beta_{\rm QDT}$ (Note: We have added the subscript "QDT" to avoid confusion between the parameter $\beta_{\rm QDT}$ and the length scale β). The introduction of γ emphasizes its relationship with $\mathcal{G}$, and section 2.3 demonstrates this relationship.

As we will demonstrate in section 2.3, the calculation of $S^{\rm phys}$ requires two linearly independent, energy-normalized wave functions at large R in each open channel and the bound state wave function in each closed channel. To this end, we define the two open-channel reference wave functions $f(R)$ and $g(R)$ by their asymptotic normalization and phase. For $E_i > 0$,

$$f_i(R) \xrightarrow{R\to\infty} \frac{1}{\sqrt{k_i}}\sin(k_iR - L_i\pi/2 + \eta_i) \tag{2.13a}$$

$$g_i(R) \xrightarrow{R\to\infty} -\frac{1}{\sqrt{k_i}}\cos(k_iR - L_i\pi/2 + \eta_i), \tag{2.13b}$$

where $k_i = \sqrt{E_i}$ is the asymptotic limit of $k_i(R)$. The normalization factor of $1/\sqrt{k_i}$ defines the energy-normalization of $f(R)$ and $g(R)$. Equation (2.13a) defines the parameter η. The reference wave functions $f(R)$ and $g(R)$ have an asymptotic phase shift of η from the spherical Bessel functions $j_L(kR)$ and $n_L(kR)$,

$$j_{L_i}(k_iR) \xrightarrow{R\to\infty} \frac{\sin(k_iR - L_i\pi/2)}{k_iR} \tag{2.14a}$$

$$n_{L_i}(k_iR) \xrightarrow{R\to\infty} -\frac{\cos(k_iR - L_i\pi/2)}{k_iR}. \tag{2.14b}$$

We use the parameters $\mathcal{A}$ and $\mathcal{G}$ to create a Wronskian-preserving transformation between the reference wave functions $\hat{f}(R)$ and $\hat{g}(R)$ and the reference wave functions $f(R)$ and $g(R)$ for $E_i > 0$,

$$\begin{pmatrix} f_i(R) \\ g_i(R) \end{pmatrix} = \begin{pmatrix} \mathcal{A}_i^{1/2} & 0 \\ \mathcal{A}_i^{-1/2}\mathcal{G}_i & \mathcal{A}_i^{-1/2} \end{pmatrix} \begin{pmatrix} \hat{f}_i(R) \\ \hat{g}_i(R) \end{pmatrix}. \tag{2.15}$$

This transformation defines the parameters $\mathcal{A}$ and $\mathcal{G}$. The parameter $\mathcal{A}$ is responsible for the

energy-normalization of $f(R)$ and $g(R)$, and the parameter $\mathcal{G}$ accounts for the different phase that $\hat{f}(R)$ and $\hat{g}(R)$ accumulate in $V^{\rm lr}(R)$ when $E_i > 0$.

For $E_i < 0$, the parameter γ determines the linear combination of $\hat{f}(R)$ and $\hat{g}(R)$ that vanishes as $R \to \infty$. We represent this linear combination by the reference wave function $\chi^-(R)$. For $E_i < 0$,

$$\chi_i^-(R) = \hat{f}_i(R)\sin\gamma_i + \hat{g}_i(R)\cos\gamma_i \xrightarrow{R\to\infty} \propto e^{-\kappa_i R}, \tag{2.16}$$

where $\kappa_i(R) = ik(R)$ and $\kappa_i(R)$ assumes its asymptotic value $\kappa_i = \sqrt{|E_i|}$ in equation (2.16). This equation defines γ.

We simply calculate the four MQDT parameters in terms of several Wronskians that involve the asymptotic limit of $\hat{f}(R)$ and $\hat{g}(R)$,

$$\tan\eta = \left.\frac{W\left((kR)j_L(kR), \hat{f}(R)\right)}{W\left((kR)n_L(kR), \hat{f}(R)\right)}\right|_{R\to\infty} \tag{2.17a}$$

$$\mathcal{A}^{-1} = \left.\frac{W\left((kR)j_L(kR), \hat{f}(R)\right)^2 + W\left((kR)n_L(kR), \hat{f}(R)\right)^2}{k}\right|_{R\to\infty} \tag{2.17b}$$

$$\mathcal{G} = -\left.\frac{W\left(g(R), \hat{g}(R)\right)}{W\left(g(R), \hat{f}(R)\right)}\right|_{R\to\infty} \tag{2.17c}$$

$$\tan\gamma = -\left.\frac{W\left(e^{-\kappa R}, \hat{g}(R)\right)}{W\left(e^{-\kappa R}, \hat{f}(R)\right)}\right|_{R\to\infty}, \tag{2.17d}$$

where $W\left(y_1(R), y_2(R)\right)$ is the Wronskian with respect to R of any two functions $y_1(R)$ and $y_2(R)$,

$$W\left(y_1, y_2\right) = y_1(R)\frac{\mathrm{d}y_2(R)}{\mathrm{d}R} - y_2(R)\frac{\mathrm{d}y_1(R)}{\mathrm{d}R}. \tag{2.18}$$

Additionally, although $S^{\rm phys}$ does not depend on the sign of $\mathcal{A}^{1/2}$, we can calculate $\mathcal{A}^{1/2}$ from η and the asymptotic limit of a Wronskian,

$$\mathcal{A}^{-1/2} = -\csc\eta W\left((kR)j_L(kR), \hat{f}(R)\right)\Big|_{R\to\infty}. \tag{2.19}$$

2.3 Zeroth-Order MQDT

Typical applications of MQDT simply set $V'(R) = 0$ beyond $R_{\rm m}$. We refer to the choice of $V'(R) = 0$ as "zeroth-order" MQDT. In chapter 3, we develop an extension of MQDT that includes the effects of $V'(R)$ beyond $R_{\rm m}$ using perturbation theory. In this section, we describe the zeroth-order MQDT calculation, following reference [54]. Note that the same ideas and notations re-appear in chapter 3. Since $V'(R) = 0$ in this section, we denote $M(R)$ as $M^{(0)}(R)$ beyond $R_{\rm m}$, where the zero superscript on $M^{(0)}(R)$ emphasizes that this wave function matrix only solves equation (2.2) when $V'(R) = 0$. We use the zero superscript in the same manner throughout the rest of this thesis.

When $V'(R) = 0$ beyond $R_{\rm m}$, $V^{\rm lr}(R)$ is a complete representation of the full potential beyond $R_{\rm m}$. Thus, the reference wave functions $\hat{f}(R)$ and $\hat{g}(R)$, as well as the representation of $M^{(0)}(R)$ in equation (2.10), are numerically exact solutions to equation (2.2) in the region $R_{\rm m} \leq R < \infty$. We compactly represent the asymptotic behavior of the reference wave functions in terms of the four weakly energy-dependent QDT parameters: η, $\mathcal{A}$, $\mathcal{G}$, and γ. The QDT parameters and $K^{\rm sr}$ fully specify the asymptotic normalization and phase of $M^{(0)}(R)$, providing all of the information required to calculate scattering observables. We demonstrate below that we can use $K^{\rm sr}$ and the QDT parameters to efficiently compute $S^{\rm phys}$ in three steps.

Because we separately handle the open channels and the closed channels in these steps, we partition the wave function matrices $\hat{f}(R)$ and $\hat{g}(R)$ into open (P) channels and closed (Q) channels. The matrices $\hat{f}_{\rm P}(R)$ and $\hat{g}_{\rm P}(R)$ are $N_{\rm o} \times N_{\rm o}$ diagonal matrices whose diagonal elements consist of the open-channel reference wave functions $\hat{f}(R)$ and $\hat{g}(R)$, respectively. The matrices $\hat{f}_{\rm Q}(R)$, $\hat{g}_{\rm Q}(R)$, and $\chi^{-}_{\rm Q}(R)$ are $N_{\rm c} \times N_{\rm c}$ diagonal matrices whose diagonal elements consists of the closed-channel reference wave functions $\hat{f}(R)$, $\hat{g}(R)$, and $\chi^{-}(R)$, respectively, where $N_{\rm c}$ is the number of closed channels. Likewise, we promote the QDT parameters to diagonal matrices of the appropriate sizes. The matrices $\mathcal{A}$, $\mathcal{G}$, and η are $N_{\rm o} \times N_{\rm o}$ diagonal matrices whose diagonal elements consist of the open-channel QDT parameters $\mathcal{A}$, $\mathcal{G}$, and η, respectively. The matrix γ is an $N_{\rm c} \times N_{\rm c}$ diagonal

matrix whose diagonal elements consist of the closed-channel QDT parameter γ. We also use these same matrices in chapter 3.

2.3.1 Closed Channel Elimination

First, we use the closed-channel QDT parameter γ to transform $M^{(0)}(R)$ into the $N \times N_{\rm o}$ physical wave function matrix $\hat{F}^{(0)}(R)$. We demand that this physical wave function matrix vanishes as $R \to 0$ in all channels, and we demand that it vanishes as $R \to \infty$ in the asymptotically closed channels. We enforce both of these boundary conditions on $\hat{F}^{(0)}(R)$ by performing the linear transformation $\hat{F}^{(0)}(R) = M^{(0)}(R)B$, where B is an $N \times N_{\rm o}$ constant matrix. This transformation forms $\hat{F}^{(0)}(R)$ by taking linear combinations of the columns of $M^{(0)}(R)$, which all vanish at the origin. Therefore, $\hat{F}^{(0)}(R)$ must also be zero at the origin, regardless of the value of B. The constant B specifies the $N_{\rm o}$ particular linear combinations of the columns of $M^{(0}(R)$ that asymptotically vanish in the closed channels. Since both $\hat{F}^{(0)}(R)$ and $M^{(0)}(R)$ are solutions to equation (2.2) in the region $R_{\rm m} \leq R < \infty$ when $V'(R) = 0$, this transformation and the determination of B can take place at any location $R \geq R_{\rm m}$.

We can find a representation of $\hat{F}^{(0)}(R)$ in terms of only $K^{\rm sr}$ and the QDT parameter γ. To achieve this, we write $\hat{F}^{(0)}(R)$ as a linear combination of $\hat{f}(R)$ and $\hat{g}(R)$ in all channels. We represent the open channels of $\hat{F}^{(0)}(R)$ by the $N_{\rm o} \times N_{\rm o}$ matrix $\hat{F}^{(0)}_{\rm P}$,

$$\hat{F}^{(0)}_{\rm P}(R) = \hat{f}_{\rm P}(R) - \hat{g}_{\rm P}(R)\tilde{K}. \tag{2.20}$$

This equation defines the $N_{\rm o} \times N_{\rm o}$ matrix $\tilde{K}$. The normalization of $\hat{F}^{(0)}(R)$ does not affect the vanishing boundary conditions on $\hat{F}^{(0)}(R)$ at the origin or asymptotically. Therefore, we simply give $\hat{F}^{(0)}_{\rm P}(R)$ a WKB-like normalization by forcing the coefficient in front of $\hat{f}_{\rm P}(R)$ in equation (2.20) to equal the $N_{\rm o} \times N_{\rm o}$ identity matrix. In order to enforce the asymptotic boundary conditions on the closed channels of $\hat{F}(R)$, we force them to be proportional to $\chi^{-}(R)$ of equation (2.16). We

represent the closed channels of $\hat{F}^{(0)}(R)$ by the $N_\mathrm{c} \times N_\mathrm{o}$ matrix $\hat{F}^{(0)}_\mathrm{Q}(R)$,

$$\hat{F}^{(0)}_\mathrm{Q}(R) = \left(\hat{f}_\mathrm{Q}(R) + \hat{g}_\mathrm{Q}(R)\cot\gamma\right) C \tag{2.21a}$$

$$= \chi^{-}_\mathrm{Q}(R)\csc\gamma C. \tag{2.21b}$$

Equation (2.21a) defines the $N_\mathrm{c} \times N_\mathrm{o}$ matrix C.

We solve for the constants $\tilde{K}$ and C in terms of the energy-smooth and field-smooth quantities K^sr and γ. Using the expression for $M^{(0)}(R)$ in equation (2.10), we write the following expression for $\hat{F}^{(0)}(R)$ in terms of B and K^sr,

$$\hat{F}^{(0)}(R) = \left(\hat{f}(R) - \hat{g}(R)K^\mathrm{sr}\right) B. \tag{2.22}$$

Repartitioning $M^{(0)}(R)$ and B into open (P) channels and closed (Q) channels, we have the following expression for $\hat{F}^{(0)}(R)$ beyond R_m in terms of K^sr and B. In block notation,

$$\begin{pmatrix} \hat{F}^{(0)}_\mathrm{P}(R) \\ \hat{F}^{(0)}_\mathrm{Q}(R) \end{pmatrix} = \begin{pmatrix} \hat{f}_\mathrm{P}(R) - \hat{g}_\mathrm{P}(R)K^\mathrm{sr}_\mathrm{PP} & -\hat{g}_\mathrm{P}(R)K^\mathrm{sr}_\mathrm{PQ} \\ -\hat{g}_\mathrm{Q}(R)K^\mathrm{sr}_\mathrm{QP} & \hat{f}_\mathrm{Q}(R) - \hat{g}_\mathrm{Q}(R)K^\mathrm{sr}_\mathrm{QQ} \end{pmatrix} \begin{pmatrix} B_\mathrm{P} \\ B_\mathrm{Q} \end{pmatrix}. \tag{2.23}$$

We substitute the expression for $\hat{F}^{(0)}_\mathrm{P}(R)$ in equation (2.20) and the expression for $\hat{F}^{(0)}_\mathrm{Q}(R)$ in equation (2.21a) into equation (2.23), and we equate the coefficients in front of $\hat{f}(R)$ and $\hat{g}(R)$ on both sides of this equation. This produces the following complete set of equations for $\tilde{K}$ and C,

$$\mathcal{I} = B_\mathrm{P} \tag{2.24a}$$

$$\tilde{K} = K^\mathrm{sr}_\mathrm{PP}B_\mathrm{P} + K^\mathrm{sr}_\mathrm{PQ}B_\mathrm{Q} \tag{2.24b}$$

$$C = B_\mathrm{Q} \tag{2.24c}$$

$$-\cot\gamma C = K^\mathrm{sr}_\mathrm{QP}B_\mathrm{P} + K^\mathrm{sr}_\mathrm{QQ}B_\mathrm{Q}, \tag{2.24d}$$

where $\mathcal{I}$ is the $N_\mathrm{o} \times N_\mathrm{o}$ identity matrix. We solve these equations for $\tilde{K}$ and C,

$$C = -\left(K^\mathrm{sr}_\mathrm{QQ} + \cot\gamma\right)^{-1} K^\mathrm{sr}_\mathrm{QP} \tag{2.25a}$$

$$\tilde{K} = K^\mathrm{sr}_\mathrm{PP} - K^\mathrm{sr}_\mathrm{PQ}\left(K^\mathrm{sr}_\mathrm{QQ} + \cot\gamma\right)^{-1} K^\mathrm{sr}_\mathrm{QP}. \tag{2.25b}$$

Therefore, $\tilde{K}$ and C provide a representation of $\hat{F}^{(0)}(R)$ beyond $R_{\rm m}$ in terms of $K^{\rm sr}$ and γ. Despite the energy-smooth and field-smooth behavior of $K^{\rm sr}$ and γ, the matrix $\tilde{K}$ can be a resonant function of energy or field. This resonant behavior analytically appears in the matrix inverse in equation (2.25b).

2.3.2 Energy Normalization

Second, we use the QDT parameters $\mathcal{A}$ and $\mathcal{G}$ to transform $\hat{F}^{(0)}(R)$ into the $N \times N_{\rm o}$ energy-normalized wave function matrix $F^{(0)}(R)$. Similar to the construction of $\hat{F}^{(0)}(R)$, we demand that the $N_{\rm o}$ columns of $F^{(0)}(R)$ represent physical solutions that vanish as $R \to 0$ in all channels and vanish as $R \to \infty$ in all closed channels, but we also demand that these solutions are energy-normalized. Hence, we simply perform the transformation $F^{(0)}(R) = \hat{F}^{(0)}(R)\mathcal{N}$, where $\mathcal{N}$ is an $N_{\rm o} \times N_{\rm o}$ matrix. Since $\hat{F}^{(0)}(R)$ already represents the $N_{\rm o}$ solutions with physical boundary conditions, the transformation constant $\mathcal{N}$ merely specifies the energy-normalization of $F^{(0)}(R)$. This transformation and the determination of $\mathcal{N}$ can occur at any location $R \geq R_{\rm m}$.

In order to achieve the energy-normalization of $F^{(0)}(R)$, we write the open channels of $F^{(0)}(R)$ in terms of the energy-normalized reference wave functions $f(R)$ and $g(R)$ of equation (2.13). We represent the open channels of $F^{(0)}(R)$ by the matrix $F_{\rm P}^{(0)}(R)$,

$$F_{\rm P}^{(0)}(R) = f_{\rm P}(R) - g_{\rm P}(R)K. \tag{2.26}$$

This equation defines the $N_{\rm o} \times N_{\rm o}$ matrix K. The matrices $f_{\rm P}(R)$ and $g_{\rm P}(R)$ are $N_{\rm o} \times N_{\rm o}$ diagonal matrices filled with the open channel reference wave functions $f(R)$ and $g(R)$, respectively. In equation (2.26), we demand that the coefficient in front of $f_{\rm P}(R)$ is equal to the $N_{\rm o} \times N_{\rm o}$ identity matrix so that $F_{\rm P}^{(0)}(R)$ has the same energy-normalization as $f_{\rm P}(R)$.

In order to find a representation of $F_{\rm P}^{(0)}(R)$ in terms of $K^{\rm sr}$ and the QDT parameters, we represent $F_{\rm P}^{(0)}(R)$ as a linear combination of $\hat{f}_{\rm P}(R)$ and $\hat{g}_{\rm P}(R)$. We use the transformation in equation (2.15) to write equation (2.26) in terms of $\hat{f}(R)$ and $\hat{g}(R)$, and we substitute the resulting expression for $F_{\rm P}^{(0)}(R)$ and the expression for $\hat{F}_{\rm P}^{(0)}(R)$ in equation (2.20) into the open channels of

the transformation $F^{(0)}(R) = \hat{F}^{(0)}(R)\mathcal{N}$. Equating the coefficients in front of $\hat{f}_{\rm P}(R)$ and $\hat{g}_{\rm P}(R)$ on both sides of this equation, we derive the following expressions for $\mathcal{N}$ and K,

$$\mathcal{N} = \left(\mathcal{I} + \mathcal{G}\tilde{K}\right)^{-1} \mathcal{A}^{1/2} \tag{2.27a}$$

$$K = \mathcal{A}^{1/2}\tilde{K}\left(\mathcal{I} + \mathcal{G}\tilde{K}\right)^{-1} \mathcal{A}^{1/2}. \tag{2.27b}$$

Since $\tilde{K}$ is known in terms of $K^{\rm sr}$ and γ in equation (2.25b), K provides a representation of $F^{(0)}_{\rm P}(R)$ beyond $R_{\rm m}$ in terms of energy-smooth and field-smooth quantities.

2.3.3 The Scattering Matrix

Finally, we use the QDT parameter η to transform $F^{(0)}(R)$ into $\Psi(R)$ of equation (2.5). This requires a simple renormalization of $F^{(0)}(R)$,

$$\Psi(R) = F(R)(\mathcal{I} - iK)^{-1} e^{i\eta}. \tag{2.28}$$

We write the standard, physical scattering matrix $S^{\rm phys}$ of equation (2.5) in terms of K and η,

$$S^{\rm phys} = e^{i\eta}\frac{\mathcal{I} + iK}{\mathcal{I} - iK}e^{i\eta}. \tag{2.29}$$

This equation for $S^{\rm phys}$, equation (2.27b) for K, and equation (2.25b) for $\tilde{K}$ demonstrate that the matrix $K^{\rm sr}$ and the four QDT parameters contain all of the information needed to compute all scattering observables.

As we demonstrate in section 2.5, the QDT parameters are smooth functions of energy. Because the Zeeman or Stark effect shifts the threshold energy of the scattering channels, the QDT parameters are also smooth functions of field. Ideally, $K^{\rm sr}$ is a smooth function of energy and field as well. In practice, we numerically determine $K^{\rm sr}$ and the QDT parameters over a wide range of energy and field with a coarse spacing in energy and field, and we interpolate their values. We then use the three equations (2.25b), (2.27b), and (2.29) to efficiently generate $S^{\rm phys}$ over this whole range by means of simple MQDT algebra. For clarity, we rewrite this set of equations below,

$$\tilde{K} = K^{\rm sr}_{\rm PP} - K^{\rm sr}_{\rm PQ}(K^{\rm sr}_{\rm QQ} + \cot\gamma)^{-1}K^{\rm sr}_{\rm QP} \tag{2.30a}$$

$$K = \mathcal{A}^{1/2}\tilde{K}\left(\mathcal{I} + \mathcal{G}\tilde{K}\right)^{-1}\mathcal{A}^{1/2} \tag{2.30b}$$

$$S^{\text{phys}} = e^{i\eta}\frac{\mathcal{I} + iK}{\mathcal{I} - iK}e^{i\eta}. \tag{2.30c}$$

2.4 Standardizing MQDT

Since the QDT parameters clearly depend on the particular choice of reference wave functions, standardizing this choice allows the QDT parameters for a particular long-range potential to be tabulated once and for all and defines a simple procedure to find K^{sr} [34]. In general, the boundary conditions in equation (2.11) define an infinite family of reference wave functions — one set for each value of ϕ_i. This section identifies a value of ϕ_i that guarantees both the maximal numerical stability of the QDT parameters as well as their smooth, analytic energy behavior. Moreover, since we use ϕ_i to apply the boundary conditions in equation (2.11), the calculation of this phase must be numerically stable — even at high L — to be useful.

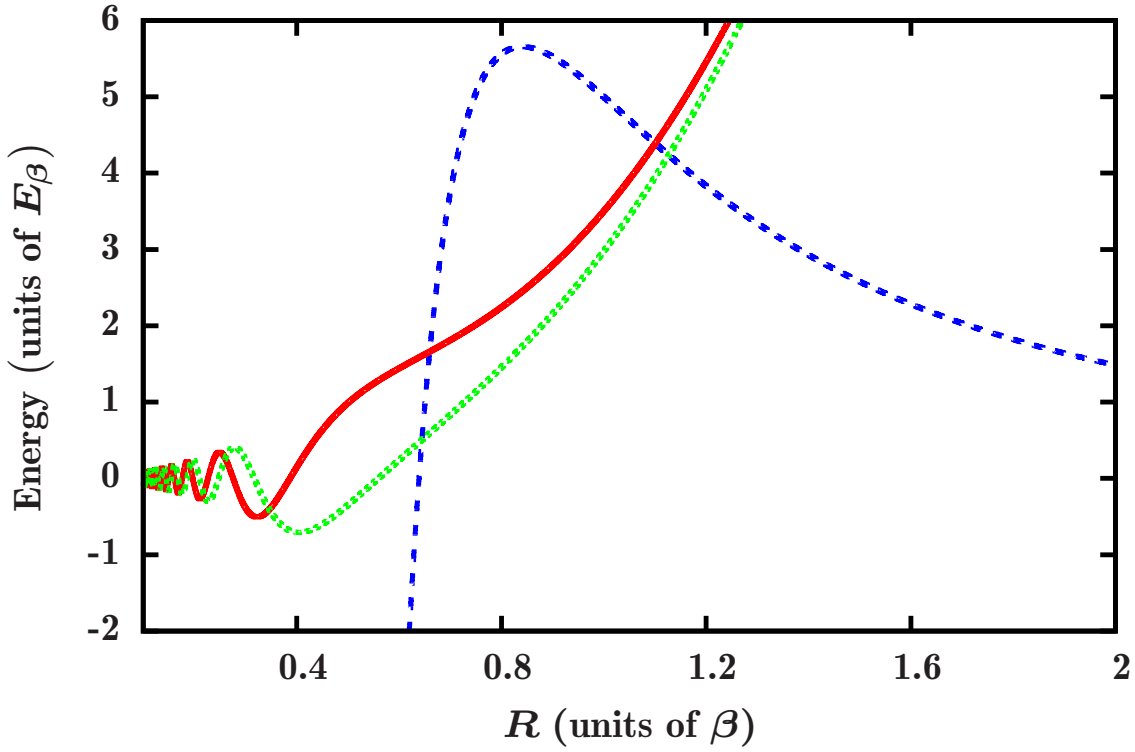

(a) $\hat{f}(R)$ and $\hat{g}(R)$ lose independence.

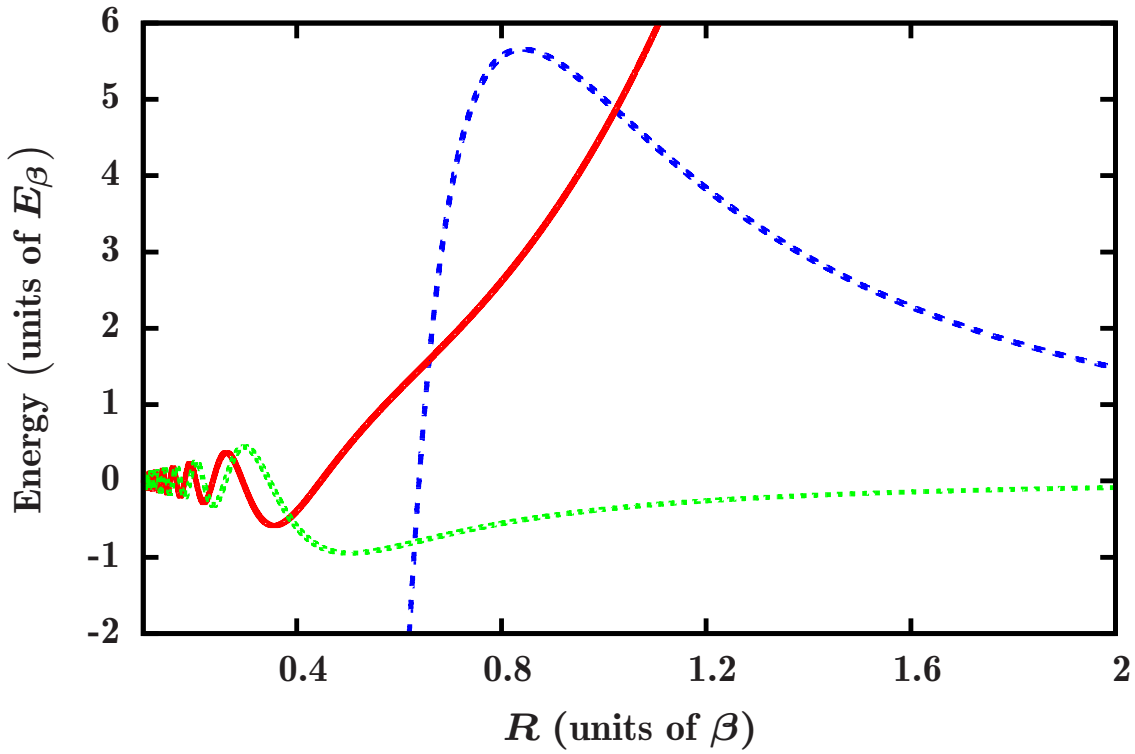

(b) $\hat{f}(R)$ and $\hat{g}(R)$ maintain independence.

Figure 2.1: The reference wave functions $\hat{f}(R)$ (red solid curve) and $\hat{g}(R)$ (green dotted curve) are shown for $E_i \approx 6.547 \times 10^{-3}$ in the long-range potential $V^{\rm lr} = -1/R^6$ (blue dashed curve) with $L = 2$. At short range, $\hat{f}(R)$ and $\hat{g}(R)$ are linearly independent. Under the classical barrier, these functions (a) lose their independence when $\hat{f}(R)$ is chosen to asymptotically coincide with $\chi_0^+(R)$ at zero energy and (b) retain their independence when $\hat{g}(R)$ is chosen to asymptotically coincide with $\chi_0^-(R)$ at zero energy.

In the manner of reference [34], we standardize the QDT parameters by letting one of the reference wave functions asymptotically coincide (up to a normalization) with a particular wave function at *zero* energy. The choice of this standard, zero-energy wave function, therefore, identifies a particular value of ϕ_i and determines a particular $\hat{f}(R)$ and $\hat{g}(R)$ at zero energy. We then obtain the energy dependence of $\hat{f}(R)$ and $\hat{g}(R)$ from their WKB-like boundary conditions in equation (2.11). In principle, any value of ϕ_i is equally valid as long as $\hat{f}(R)$ and $\hat{g}(R)$ remain linearly independent at long range. However, at ultracold energies, motion under a classical centrifugal barrier can often cause a pair of reference wave functions to become numerically linearly dependent. It is our goal to find the value of ϕ_i that leads (in the limit of zero energy) to maximally linearly independent reference wave functions under and beyond this barrier.

For all long-range potentials $V^{\rm lr}(R)$ that fall off faster than $1/R^2$, one can uniquely specify a zero-energy wave function in $V^{\rm lr}(R)$ as a particular asymptotic linear combination of R^{L+1} and R^{-L}, which are zero-energy free-particle wave functions. Likewise, for all long-range potentials that are asymptotically dominated by $-1/R^6$, the asymptotic limit of every zero-energy wave function in $V^{\rm lr}(R)$ is a particular linear combination of the two zero-energy solutions $\chi_0^+(R)$ and $\chi_0^-(R)$ in the long-range potential $V^{\rm lr} = -1/R^6$. We define these analytically known zero-energy solutions below and give their asymptotic behavior in terms of R^{L+1} and R^{-L} [58],

$$\chi_0^+(R) = \sqrt{R} J_{-\frac{1}{4}(2L+1)}(1/2R^2) \xrightarrow{R\to\infty} \propto R^{L+1} \tag{2.31a}$$

$$\chi_0^-(R) = \sqrt{R} J_{\frac{1}{4}(2L+1)}(1/2R^2) \xrightarrow{R\to\infty} \propto R^{-L}. \tag{2.31b}$$

The zero subscripts on $\chi_0^+(R)$ and $\chi_0^-(R)$ emphasize that these are solutions at exactly zero energy. Here, $J_\nu(x)$ is the Bessel function of the first kind. For $L > 0$, these solutions take their asymptotic form under the classical barrier at $R \gtrsim 1$. From the set of equations (2.31), we see that $\chi_0^+(R)$ rapidly grows as R increases, and it becomes much larger than $\chi_0^-(R)$. Hence, in all long-range potentials that are dominated by $-1/R^6$, all zero-energy wave functions are greatly dominated by the contribution from $\chi_0^+(R)$ and start to resemble $\chi_0^+(R)$ under the barrier — numerically losing their linear independence – except for wave functions that are directly proportional to $\chi_0^-(R)$.

Figure 2.1(a) shows $\hat{f}(R)$ and $\hat{g}(R)$ in the long-range potential $V^{\rm lr} = -1/R^6$ with an energy of $E_i \approx 6.547 \times 10^{-3}$. This energy corresponds to 1 μK for ^{40}K + ^{87}Rb when $C_6 = 4.300 \times 10^3$ in atomic units. Here, we chose $\hat{f}(R)$ to asymptotically coincide with $\chi_0^+(R)$ at zero energy. The boundary conditions in equation (2.11) ensure the maximal independence of $\hat{f}(R)$ and $\hat{g}(R)$ at short range, but they both resemble $\chi_0^+(R)$ in the classically forbidden region $R \gtrsim 1$. While we choose $\hat{f}(R)$ to grow like R^{L+1} under the classical barrier, $\hat{g}(R)$ also quickly begins to grow in a similar way. Hence, this choice for $\hat{f}(R)$ leads to a set of reference wave functions that exhibit increasing linear dependence as the collision energy approaches zero and the classical barrier grows. In fact, $\hat{g}(R)$ always asymptotically diverges at zero energy except for a unique value of ϕ_i.

Since only $\chi_0^-(R)$ remains numerically linearly independent from $\chi_0^+(R)$ in the limit $R \to \infty$, letting $\hat{g}(R)$ asymptotically coincide with $\chi_0^-(R)$ at zero energy guarantees that the zero-energy limit of $\hat{g}(R)$ is maximally independent from $\hat{f}(R)$ not only at short range but also well into the classically forbidden region. Moving away from zero energy causes $\hat{g}(R)$ to gain a contribution from $\chi_0^+(R)$ asymptotically, but the classically forbidden region becomes smaller. Figure 2.1(b) shows that this choice for $\hat{g}(R)$ leads to reference wave functions that are linearly independent at both short range and long range — even at ultracold energies and high L. Hence, these reference wave functions are ideal for a numerical calculation of the QDT parameters at ultracold energies.

In order to implement this standardization, one must determine the value of ϕ_i that is used to define $\hat{f}(R)$ and $\hat{g}(R)$. For long-range potentials in which the zero-energy solutions are known analytically at all R, this value of ϕ_i is easily derived using the values of $\chi_0^+(R)$ and/or $\chi_0^-(R)$ at $R_{\rm x}$. However, since even the zero-energy solutions are only known analytically for a limited number of power law potentials, numerically calculating ϕ_i allows the use of the true long-range potential for a given scattering problem.

To this end, the zero-energy reference wave functions for $\phi_i = 0$ are numerically propagated from their boundary conditions at $R_{\rm x} << 1$ to large $R >> 1$ where $V^{\rm lr}(R)$ takes a simple form. At $R >> 1$, the zero-energy reference wave functions are well approximated by linear combinations of solutions that are known analytically, and $\tan\phi_i$ is a simple ratio of two Wronskians. For

example, the value of $\tan\phi_i$ that lets $\hat{f}(R)$ asymptotically coincide with $\chi_0^+(R)$ at zero energy is given by,

$$\tan\phi_i \xrightarrow{R\to\infty} \frac{W\left(\chi_0^+(R), \hat{f}_{(\phi_i=0)}(R)\right)}{W\left(\chi_0^+(R), \hat{g}_{(\phi_i=0)}(R)\right)}. \tag{2.32a}$$

An alternative choice allows $\hat{g}(R)$ to asymptotically coincide with $\chi_0^-(R)$ at zero energy, and this value of $\tan\phi_i$ is given by,

$$\tan\phi_i \xrightarrow{R\to\infty} -\frac{W\left(\chi_0^-(R), \hat{g}_{(\phi_i=0)}(R)\right)}{W\left(\chi_0^-(R), \hat{f}_{(\phi_i=0)}(R)\right)}. \tag{2.32b}$$

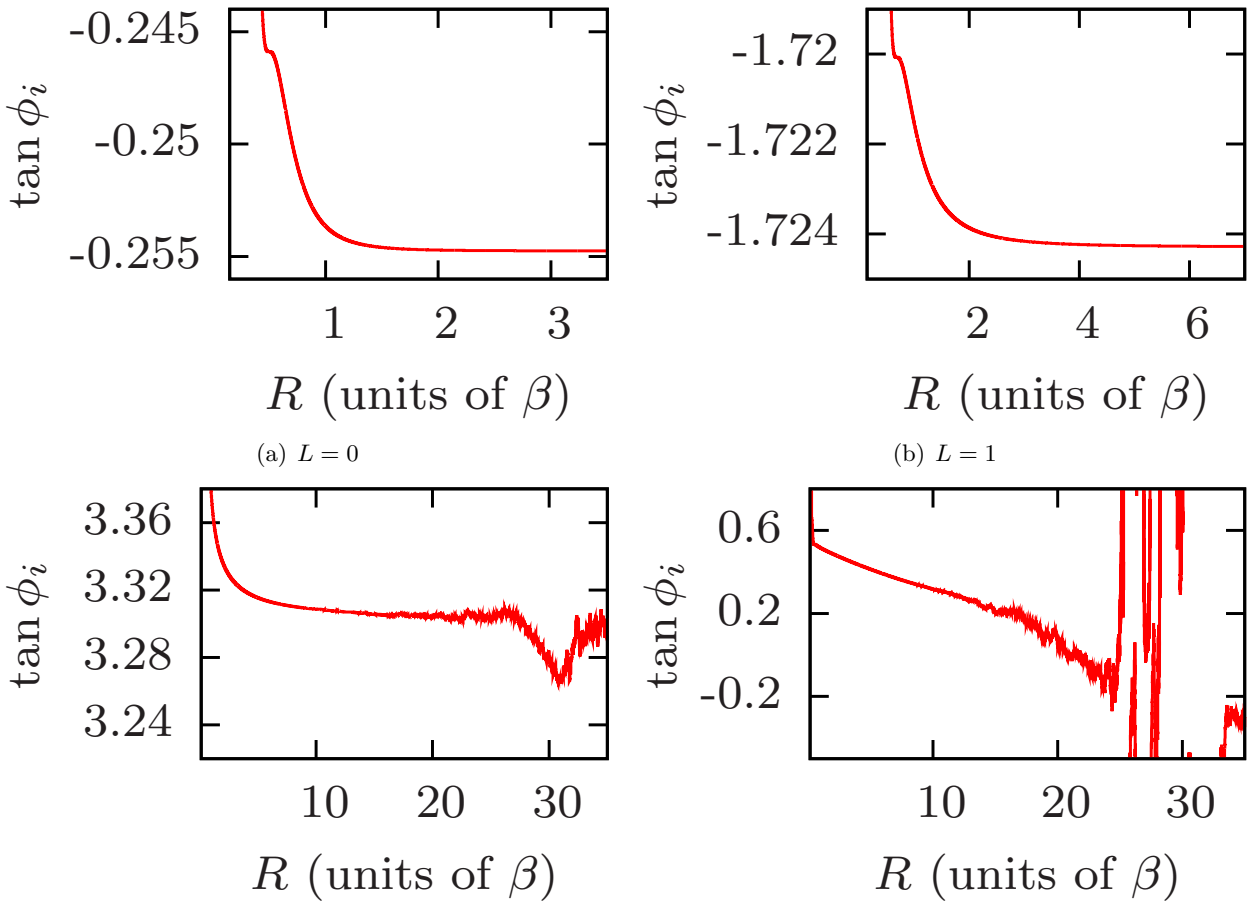

(a) $L = 0$ (b) $L = 1$

(c) $L = 2$ (d) $L = 3$

Figure 2.2: The convergence of $\tan\phi_i$ with R is shown when $L = 0 - 3$. The reference wave function $\hat{f}(R)$ is chosen to asymptotically coincide with $\chi_0^+(R)$ at zero energy in a long-range potential of the form $V^{\rm lr} = -C_6/R^6 - C_8/R^8 - C_{10}/R^{10}$, and $R_{\rm x} = 0.1$.

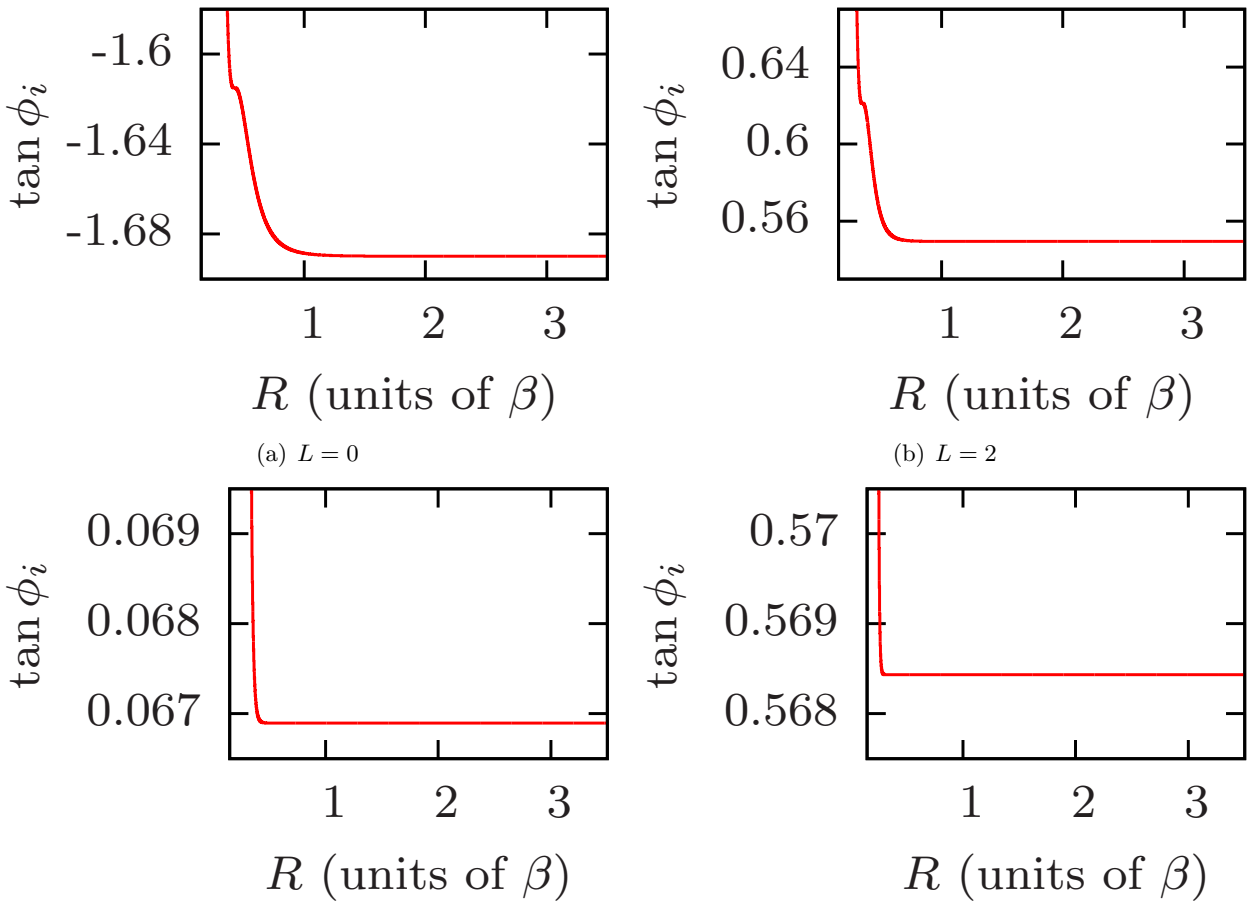

(a) $L = 0$ (b) $L = 2$

(c) $L = 10$ (d) $L = 20$

Figure 2.3: The convergence of $\tan\phi_i$ with R is shown when $L = 0$, 2, 10, and 20. The reference wave function $\hat{g}(R)$ is chosen to asymptotically coincide with $\chi_0^-(R)$ at zero energy in a long-range potential of the form $V^{\rm lr}(R) = -C_6/R^6 - C_8/R^8 - C_{10}/R^{10}$, and $R_{\rm x} = 0.1$.

The stable calculation of ϕ_i requires the linear independence of the reference wave functions $\hat{f}_{(\phi_i=0)}(R)$ and $\hat{g}_{(\phi_i=0)}(R)$. As they each asymptotically represent a particular linear combination of $\chi_0^+(R)$ and $\chi_0^-(R)$, their linear independence relies on their different, and quickly vanishing, contributions from $\chi_0^-(R)$. Hence, they can easily lose their linear independence as R grows, causing the calculation of ϕ_i to become unstable. For example, figure 2.2 demonstrates the difficulty of numerically calculating ϕ_i by showing the numerically computed ratio of Wronskians in equation (2.32a) for several values of L. These calculations use a long-range potential of the form $V^{\mathrm{lr}}(R) = -C_6/R^6 - C_8/R^8 - C_{10}/R^{10}$, where the dispersion coefficients are $C_6 = 4.300 \times 10^3$, $C_8 = 4.823 \times 10^5$, and $C_{10} = 6.181 \times 10^7$ in atomic units. These values are realistic for collisions of K + Rb [59].

Figure 2.2 shows that the calculation of $\tan\phi_i$, at least for $L = 0$, converges quickly after the separation $R = 1$, where the terms $-C_8/R^8$ and $-C_{10}/R^{10}$ of the long-range potential become dominated by the term $-C_6/R^6$. However, as L increases, a larger value of R is required to converge this calculation, and figure 2.2 shows that a converged calculation of $\tan\phi_i$ is not numerically stable for $L > 1$. Section 2.4.1 explores this instability and determines that, for $L > 1$, finite numerical noise eventually dominates the asymptotic contribution to each reference wave function from $\chi_0^-(R)$, causing the calculation of $\tan\phi_i$ to be unstable. If we cannot even stably compute ϕ_i, calculating the QDT parameters is hopeless.

However, section 2.4.1 also shows that this instability vanishes if $\hat{g}(R)$ is chosen to asymptotically coincide with $\chi_0^-(R)$ at zero energy — the same choice as in figure 2.1(b). For *only* this choice of $\hat{g}(R)$, the calculation of ϕ_i does not require finding the asymptotic contribution to $\hat{f}_{(\phi_i=0)}(R)$ and $\hat{g}_{(\phi_i=0)}(R)$ from $\chi_0^-(R)$. Hence, in this case, the calculation of $\tan\phi_i$ is numerically stable for all L. In contrast to figure 2.2, figure 2.3 shows the numerically computed ratio of Wronskians in equation (2.32b), demonstrating that this calculation of $\tan\phi_i$ stably converges with R. These calculations use the same long-range potential as the calculations in figure 2.2 and include much larger values of L.

The calculations of $\tan\phi_i$ in figure 2.3 converge more rapidly as L increases. This trend

is intuitive because, as L grows, the classical turning point at zero energy moves inward, causing $\chi_0^-(R)$ to become increasingly distinct from all other solutions. Moreover, these calculations of $\tan\phi_i$ are stable out to large $R \gtrsim 10^3$. This allows for a more consistent calculation of the QDT parameters because the value of R at which ϕ_i is actually determined can equal the value of R that is necessary for a well-converged calculation of the QDT parameters. Although either $\hat{f}(R)$ or $\hat{g}(R)$ could asymptotically coincide with $\chi_0^-(R)$ at zero energy, choosing $\hat{g}(R)$ for this role defines our standardization because the QDT parameters acquire appealing qualities. Section 2.5 explores these qualities.

2.4.1 Instability of ϕ_i

In this section, we consider the calculation of the phase ϕ_i that defines the reference wave functions $\hat{f}(R)$ and $\hat{g}(R)$ in equation (2.11). The phase ϕ_i describes the particular linear combination of $\hat{f}_{(\phi_i=0)}(R)$ and $\hat{g}_{(\phi_i=0)}(R)$ that coincides with a wave function of our choice at zero energy. We choose this wave function according to its asymptotic behavior and define our reference wave functions at R_x. Therefore, we can determine ϕ_i by numerically propagating $\hat{f}_{(\phi_i=0)}(R)$ and $\hat{g}_{(\phi_i=0)}(R)$ from their boundary conditions at R_x to large R. However, numerical error causes this propagation to become unstable in the presence of a centrifugal barrier; hence, the numerical calculation of ϕ_i can also become unstable.

For example, we consider the $-1/R^6$ potential. In this potential, every zero-energy wave function is a linear combination of the analytically known wave functions in equation (2.31) at all R. These wave functions have well-known asymptotic behaviors and are exact solutions at all R. Therefore, their behavior at R_x determines ϕ_i without any numerical propagation. Nevertheless, we can still attempt to numerically determine ϕ_i by propagating the wave functions $\hat{f}_{(\phi_i=0)}(R)$ and $\hat{g}_{(\phi_i=0)}(R)$ from their boundary conditions at R_x to large R. By studying the deviation of our numerically determined value of ϕ_i from the analytically known value, we characterize the numerical instability of this calculation. Moreover, we identify a robust method for avoiding this instability that is easily generalized to any potential that asymptotically decays faster than $1/R^2$.

We write the zero-energy wave functions $\hat{f}_{(\phi_i=0)}(R)$ and $\hat{g}_{(\phi_i=0)}(R)$ in terms of the analytic wave functions in equation (2.31) by defining a 2×2 constant matrix c,

$$\hat{f}_{(\phi_i=0)}(R) = c_{11}\chi_0^+(R) + c_{12}\chi_0^-(R) \tag{2.33a}$$

$$\hat{g}_{(\phi_i=0)}(R) = c_{21}\chi_0^+(R) + c_{22}\chi_0^-(R). \tag{2.33b}$$

If we choose to let $\hat{f}(R)$ coincide with $\chi_0^+(R)$ at zero energy, we can derive an expression for $\tan\phi_i$ in terms of the elements of c by using equation (2.32a),

$$\tan\phi_i = \frac{c_{11}W\left(\chi_0^+(R),\chi_0^+(R)\right) + c_{12}W\left(\chi_0^+(R),\chi_0^-(R)\right)}{c_{21}W\left(\chi_0^+(R),\chi_0^+(R)\right) + c_{22}W\left(\chi_0^+(R),\chi_0^-(R)\right)} = \frac{c_{12}}{c_{22}}. \tag{2.34}$$

However, numerically achieving this value of $\tan\phi_i$ is not guaranteed. We can track numerical error by considering the difference between a particular analytic solution and the same solution determined numerically. To this end, we expand the zero-energy wave functions $\chi_0^+(R)$ and $\chi_0^-(R)$ in powers of R at large R,

$$\chi_0^+(R) \xrightarrow{R>>1} \approx R^{L+1} + bR^{L-3} \tag{2.35a}$$

$$\chi_0^-(R) \xrightarrow{R>>1} \approx R^{-L}, \tag{2.35b}$$

where b is a known constant. The normalization of these wave functions is chosen such that $W(\chi_0^-(R),\chi_0^+(R)) = 2L+1$. We then define two numerically determined wave functions $\chi_0^{+'}(R)$ and $\chi_0^{-'}(R)$ that have the same boundary conditions at R_{x} as the analytic solutions $\chi_0^+(R)$ and $\chi_0^-(R)$, respectively. Moreover, we demand that $\chi_0^{+'}(R)$ and $\chi_0^{-'}(R)$ have the exact same asymptotic normalization as their analytic counterparts.

Numerical error causes the wave functions $\chi_0^{+'}(R)$ and $\chi_0^{-'}(R)$ to differ from the analytic solutions in two ways. First, only the leading order terms in their asymptotic expansions agree exactly. Hence, the asymptotic expansion of $\chi_0^{+'}(R)$ has a coefficient b' in its second highest order term that differs slightly from the coefficient b in equation (2.35a). Thus, we represent the numerical error by the constant $\delta \approx b - b'$. Second, the numerical wave functions become slightly different linear combinations of the analytic solutions, such that $\chi_0^{+'}(R)$ gains a contribution from $\chi_0^-(R)$

that is proportional to the error δ. The wave function $\chi_0^{-'}(R)$ differs from $\chi_0^{-}(R)$ in analogous ways, and we expand both of the numerical wave functions in powers of R at large R,

$$\chi_0^{+'}(R) \xrightarrow{R>>1} \approx R^{L+1} + b' R^{L-3} + \delta R^{-L} \tag{2.36a}$$

$$\chi_0^{-'}(R) \xrightarrow{R>>1} \approx R^{-L} + \delta \left(R^{L+1} + b R^{L-3} \right). \tag{2.36b}$$

The presence of numerical error also changes the wave functions $\hat{f}_{(\phi_i=0)}(R)$ and $\hat{g}_{(\phi_i=0)}(R)$. We call these numerically determined wave functions $\hat{f}'_{(\phi_i=0)}(R)$ and $\hat{g}'_{(\phi_i=0)}(R)$, and they lead to the numerically determined phase ϕ'_i. We define $\hat{f}'_{(\phi_i=0)}(R)$ and $\hat{g}'_{(\phi_i=0)}(R)$ by their boundary conditions at R_{x}. Therefore, these functions are exactly equal to the functions in equation (2.33) at R_{x}, but they take a slightly different form at large R. We approximate their large-R behavior as the following,

$$\hat{f}'_{(\phi_i=0)}(R) \xrightarrow{R>>1} c_{11}\chi_0^{+'}(R) + c_{12}\chi_0^{-'}(R) \tag{2.37}$$

$$\hat{g}'_{(\phi_i=0)}(R) \xrightarrow{R>>1} c_{21}\chi_0^{+'}(R) + c_{22}\chi_0^{-'}(R). \tag{2.38}$$

Substituting these wave functions into equation (2.32a) leads to an equation for $\tan\phi'_i$ that depends on the product δR^{2L-3} at large R,

$$\tan\phi'_i \xrightarrow{R>>1} \frac{c_{11} W\left(\chi_0^{+}(R), \chi_0^{+'}(R)\right) + c_{12} W\left(\chi_0^{+}(R), \chi_0^{-'}(R)\right)}{c_{21} W\left(\chi_0^{+}(R), \chi_0^{+'}(R)\right) + c_{22} W\left(\chi_0^{+}(R), \chi_0^{-'}(R)\right)} \tag{2.39a}$$

$$= \frac{c_{11} 4\delta R^{2L-3} - c_{12}(2L+1)}{c_{21} 4\delta R^{2L-3} - c_{22}(2L+1)} \tag{2.39b}$$

$$\xrightarrow{R\to\infty} \frac{c_{11}}{c_{21}} \quad \text{for } L > 1 \text{ and } \delta \neq 0. \tag{2.39c}$$

For $L > 1$, the large-R limit of this equation for $\tan\phi'_i$ approaches the wrong value c_{11}/c_{21} if δ is non-zero. Performing the actual numerical calculation of $\tan\phi'_i$ also produces this same wrong value c_{11}/c_{21}.

Since the value of $\tan\phi_i$ depends on the constants c_{12} and c_{22} and because the terms of equation (2.39b) that contain c_{12} and c_{22} are dominated by numerical error at large R when $L > 1$, we deduce that finding the contribution to $\hat{f}_{(\phi_i=0)}(R)$ and $\hat{g}_{(\phi_i=0)}(R)$ from $\chi_0^{-}(R)$ at large R is

numerically challenging when $L > 1$. In fact, letting either $\hat{f}(R)$ or $\hat{g}(R)$ — at zero energy — coincide with any wave function that has a contribution from $\chi_0^+(R)$ leads to an equation for $\tan\phi_i$ that depends on the constants c_{12} and c_{22}, and the same numerical instability exists. However, if we instead let $\hat{f}(R)$ or $\hat{g}(R)$ coincide with $\chi_0^-(R)$ at zero energy, using the numerical wave functions $\hat{f}'_{(\phi_i=0)}(R)$ and $\hat{g}'_{(\phi_i=0)}(R)$ at large R leads to an equation for $\tan\phi_i'$ that reduces to the analytic value of $\tan\phi_i$ for all L.

For example, by letting $\hat{g}(R)$ coincide with $\chi_0^-(R)$ at zero energy, we derive an expression for $\tan\phi_i$. Substituting the exact expressions for $\hat{f}_{(\phi_i=0)}(R)$ and $\hat{g}_{(\phi_i=0)}(R)$ into equation (2.32b) yields the following equation for $\tan\phi_i$,

$$\tan\phi_i = -\frac{c_{21}W\left(\chi_0^-(R),\chi_0^+(R)\right)+c_{22}W\left(\chi_0^-(R),\chi_0^-(R)\right)}{c_{11}W\left(\chi_0^-(R),\chi_0^+(R)\right)+c_{12}W\left(\chi_0^-(R),\chi_0^-(R)\right)} = -\frac{c_{21}}{c_{11}}. \tag{2.40}$$

Using the numerical wave functions $\hat{f}'_{(\phi_i=0)}(R)$ and $\hat{g}'_{(\phi_i=0)}(R)$ at large R leads to the following equations for $\tan\phi_i'$,

$$\tan\phi_i' = -\frac{c_{21}W\left(\chi_0^-(R),\chi_0^{+\prime}(R)\right)+c_{22}W\left(\chi_0^-(R),\chi_0^{-\prime}(R)\right)}{c_{11}W\left(\chi_0^-(R),\chi_0^{+\prime}(R)\right)+c_{12}W\left(\chi_0^-(R),\chi_0^{-\prime}(R)\right)} \tag{2.41a}$$

$$\xrightarrow{R>>1} -\frac{c_{21}+c_{22}\delta}{c_{11}+c_{12}\delta} \tag{2.41b}$$

$$\approx -\frac{c_{21}}{c_{11}} \quad \text{for all } L \text{ and } \delta << 1. \tag{2.41c}$$

Here, $\tan\phi_i'$ does not depend on R in the region $R >> 1$, and $\tan\phi_i'$ approaches the approximately correct value $-c_{21}/c_{11}$ even if the numerical error is finite. Of course an accurate value of $\tan\phi_i'$ requires the numerical error to be small ($c_{22}\delta << c_{21}$ and $c_{12}\delta << c_{11}$), but the divergence seen in equation (2.39b) does not appear. In this case, $\tan\phi_i$ does not depend on the constants c_{12} and c_{22}. Therefore, finding the contribution to $\hat{f}_{(\phi=0)}(R)$ and $\hat{g}_{(\phi=0)}(R)$ from $\chi_0^-(R)$ at large R is not necessary, and the numerical instability of calculating $\tan\phi_i$ vanishes.

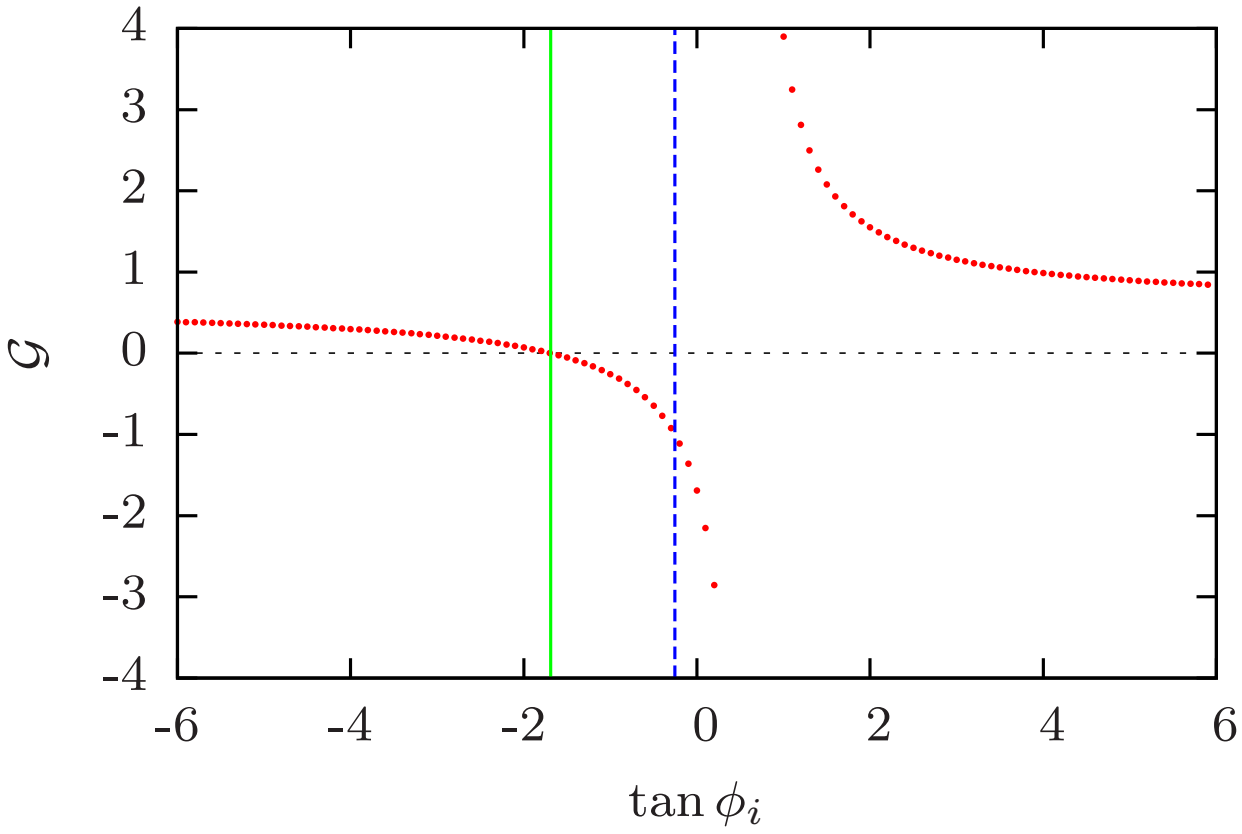

Figure 2.4: This graph shows the QDT parameter $\mathcal{G}$ (red dots) as a function of $\tan\phi_i$. The vertical lines represent the value of $\tan\phi_i$ when $\hat{f}(R)$ asymptotically coincides with $\chi_0^+(R)$ at zero energy (blue dashed line) and when $\hat{g}(R)$ asymptotically coincides with $\chi_0^-(R)$ at zero energy (green solid line). For this calculation, $V^{\rm lr} = -C_6/R^6 - C_8/R^8 - C_{10}/R^{10}$, where the dispersion coefficients are appropriate for K + Rb; $E_i \approx 6.547 \times 10^{-4}$, which corresponds to 100 nK; $L = 0$; and $R_{\rm x} = 0.1$.

2.5 Calculating QDT parameters

Having specified ϕ_i in equation (2.11), the values of the QDT parameters $\mathcal{A}$, η, $\mathcal{G}$, and γ unambiguously follow from the set of equations (2.17). Of particular importance is the parameter $\mathcal{G}$. The zero-energy limit of $\mathcal{G}$,

$$\mathcal{G} = -\frac{W\left(g(R), \hat{g}(R)\right)}{W\left(g(R), \hat{f}(R)\right)}\bigg|_{R\to\infty} \xrightarrow{E_i\to 0} -\frac{W\left(\chi_0^-(R), \hat{g}(R)\right)}{W\left(\chi_0^-(R), \hat{f}(R)\right)}\bigg|_{R\to\infty}, \tag{2.42}$$

is intimately related to the value of ϕ_i in equation (2.32b). Clearly, if $\phi_i = 0$ in equation (2.42), the zero-energy limit of $\mathcal{G}$ is the exact same value as $\tan\phi_i$ in equation (2.32b). Section 2.4.1 shows that evaluating equation (2.32b) is stable independent of the phase ϕ_i given to the reference wave functions. Therefore, the zero-energy limit of $\mathcal{G}$ is numerically stable. Figure 2.4 shows the calculation of $\mathcal{G}$ at 100 nK as a function of the zero-energy phase ϕ_i.

For a given R_{x}, figure 2.4 shows that there is a unique value of ϕ_i (indicated by the green vertical solid line) for which $\mathcal{G}$ vanishes at zero energy. This value of ϕ_i corresponds with letting $\hat{g}(R)$ asymptotically coincide with $\chi_0^-(R)$ at zero energy; therefore, the condition $\mathcal{G} = 0$ at zero energy defines our standardization. As evident from equations (2.15) and (2.13), the vanishing of $\mathcal{G}$ guarantees the maximal linear independence of $\hat{f}(R)$ and $\hat{g}(R)$ at long range. Hence, although a different standardization could guarantee that the zero-energy limit of $\mathcal{G}$ is well behaved (e.g., the blue vertical dashed line in figure 2.4), our standardization is the *only* choice that leads to maximally linearly independent reference wave functions at long range in the limit of zero energy.

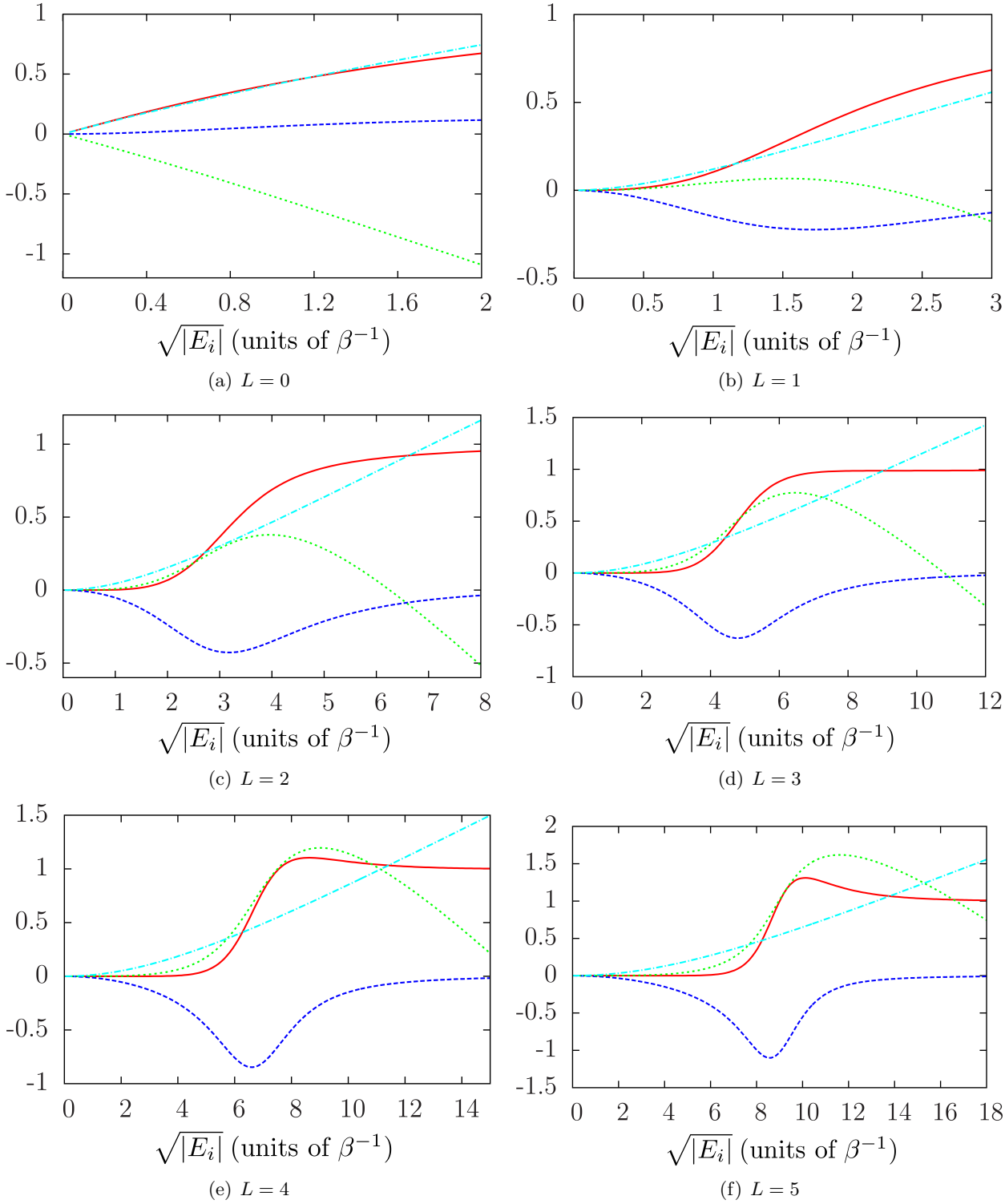

(a) $L = 0$ (b) $L = 1$ (c) $L = 2$ (d) $L = 3$ (e) $L = 4$ (f) $L = 5$

Figure 2.5: Each panel of this figure shows the QDT parameters $\mathcal{A}$ (red solid curve), $\mathcal{G}$ (blue dashed curve), η (green dotted curve), and γ (cyan dashed-dotted curve) for the realistic KRb model potential $V^{\rm lr}(R) = -C_6/R^6 - C_8/R^8 - C_{10}/R^{10}$. The panels (a – f) plot the QDT parameters for the partial waves $L = 0 - 5$, respectively. The horizontal axis of each graph is $\sqrt{|E_i|}$, where we merely use the absolute value of E_i in order to plot γ and the positive energy parameters together.

Applying our standardization, figure 2.5 illustrates the energy dependence of the various QDT parameters for the realistic KRb model potential $V^{\rm lr}(R) = -C_6/R^6 - C_8/R^8 - C_{10}/R^{10}$, where the dispersion coefficients are the same as in section 2.4. This graph uses the quantity $\sqrt{|E_i|}$ on the horizontal axis. We merely use the absolute value of E_i in order to plot γ and the positive energy parameters together. We present the QDT parameters in natural van der Waals units, where $\beta = (2\mu C_6/\hbar^2)^{1/4} = 143.9\ a_0$ and $E_\beta = 152.7\ \mu$K. Each panel represents the result for a different partial wave L. Note that a greater energy range is shown for higher L. In all cases, the calculation is numerically stable, even in the threshold limit. These functions are smooth; therefore, they are easy to interpolate. In contrast to reference [37], our QDT parameters are weak functions of energy for all L. Using these parameters, one can efficiently characterize high-L Fano-Feshbach resonances and shape resonances in collisions of K + Rb.

One striking feature, unique to our parameterization, is that all of the QDT parameters vanish as powers of E_i in the limit $E_i \to 0$. In this threshold limit, the QDT parameters are well approximated by simple analytic formulas. For alkali atoms, where $-C_8/R^8$ and $-C_{10}/R^{10}$ make small corrections to $-C_6/R^6$, we derive these formulas using the potential $-C_6/R^6$ alone. We provide a detailed derivation of these formulas in section 2.6, and we summarize the results below. The analytic formulas for the threshold behavior of the QDT parameters are conveniently parameterized in terms of a set of generalized, standard scattering lengths $\bar{a}_L$,

$$\bar{a}_L = \left(\frac{\pi 2^{-(2L+3/2)}}{\Gamma(L/2+5/4)\Gamma(L+1/2)} \right)^{2/(2L+1)}, \tag{2.43}$$

where $\Gamma(x)$ is the gamma function [58]. Here, we give the threshold behavior of all four QDT

parameters,

$$\mathcal{A}^{1/2} \xrightarrow{k\to 0} -(\bar{a}_L k)^{L+1/2} \tag{2.44a}$$

$$\eta \xrightarrow{k\to 0} (-1)^{L+1}(\bar{a}_L k)^{2L+1} + \frac{3\pi\Gamma(L-3/2)}{32\Gamma(L+7/2)}k^4 \tag{2.44b}$$

$$\mathcal{G} \xrightarrow{k\to 0} (-1)^{L+1}(\bar{a}_L k)^{4L+2} - \frac{k^2}{(2L+3)(2L-1)} \tag{2.44c}$$

$$\gamma \xrightarrow{\kappa\to 0} \begin{cases} \bar{a}_0\kappa & \text{for } L=0 \\ \frac{\kappa^2}{(2L+3)(2L-1)} & \text{for } L>0. \end{cases} \tag{2.44d}$$

These formulas agree well with the numerical results for the exact long-range potential when $E_i \lesssim 1$.

Analytic equations for standard scattering lengths, such as equation (2.43), have been derived before in the literature. For example, $\bar{a}_0$, which is the scattering length of our reference wave function $\hat{f}(R)$, coincides with the semiclassical scattering length of Gribakin and Flambaum for the potential $-C_6/R^6$ [60]. Likewise, using an exact solution that was expressed using continued fractions [61–63], Gao performed a similar analytic treatment of the near-threshold QDT parameters for the potential $-C_6/R^6$. To do so, he identified a set of standard constants $\bar{a}_{sL,\mathrm{Gao}}$ that are related to our equation (2.43) via $\bar{a}_{sL,\mathrm{Gao}} = (\bar{a}_L)^{2L+1}$. While the treatments are equivalent, our parameters $\bar{a}_L$ have units of length. Moreover, our standard and universal reference wave functions have a universal form for the corresponding phase shift in equation (2.44b).

Gao conceives of a hierarchy of reference wave functions distinguished by a short-range quantum defect parameter μ^c [44]. Our implementation of QDT introduces alternative short-range phases ϕ_i in equation (2.11). Our particular choice for ϕ_i gives our reference wave function $\hat{f}(R)$ a particular set of scattering lengths $\bar{a}_L$. Using equation (10) of reference [63] and the zero-energy limit of equation (33) of reference [63], our choice corresponds to,

$$\mu^c = 1/2 + L/4. \tag{2.45}$$

Equation (2.45) gives an explicit connection between the analytic formulas of Gao and our formulation of QDT for the potential $-C_6/R^6$.

Moreover, a similar formulation of QDT in reference [47] derives the threshold behavior of three positive energy parameters for a reference potential with an arbitrary scattering length a. These parameters are easily related to our QDT parameters for the special case of $L = 0$. Expressed in our notation, the results of reference [47] read,

$$\eta_{(L=0)} \xrightarrow{k\to 0} -ak \tag{2.46}$$

$$\mathcal{A}_{(L=0)} \xrightarrow{k\to 0} \bar{a}_0 k \left(1 + (a/\bar{a}_0 - 1)^2\right) \tag{2.47}$$

$$\mathcal{G}_{(L=0)} \xrightarrow{k\to 0} 1 - a/\bar{a}_0. \tag{2.48}$$

If $a = \bar{a}_0$ here, these formulas are consistent with the threshold behavior of our set of QDT parameters in equation (2.44).

Although section 2.6 explicitly derives the QDT parameter threshold behavior for only the potential $-1/R^6$, this analysis implies simple extensions of equation (2.44) for any potential with the form $-1/R^n$, where n is an integer and $n > 2$. The zero-energy solution $\chi_0^-(R)$ is well defined (and known analytically) for any potential of this kind,

$$\chi_0^-(R) = \sqrt{R} J_\nu \left(\frac{R^{-(2L+1)/2\nu}}{(2L+1)/2\nu} \right) \xrightarrow{R\to\infty} \propto R^{-L}, \tag{2.49}$$

where $\nu = (2L+1)/(n-2)$. Hence, for any potential that is asymptotically dominated by $-C_n/R^n$ and for all L, our standardization uniquely specifies the zero-energy limit of $\hat{f}(R)$ and $\hat{g}(R)$, and the analysis of section 2.6 is repeatable. As a consequence of our standardization of QDT, all of the QDT parameters go to zero in the limit $E_i \to 0$, and the reference wave functions $\hat{f}(R)$ and $\hat{g}(R)$ have a maximal linear independence at zero energy — even for this more general potential.

2.6 Threshold Behavior of the QDT parameters

The QDT parameters $\mathcal{A}$, η, $\mathcal{G}$, and γ connect the reference wave functions $\hat{f}(R)$ and $\hat{g}(R)$ to well-known solutions in the limit $R \to \infty$, as described in section 2.3. By considering a simple long-range potential, we can represent the zero-energy limit of $\hat{f}(R)$ and $\hat{g}(R)$ in terms of analytically known zero-energy solutions. However, these zero-energy solutions are inadequate to describe the

large-R behavior of $\hat{f}(R)$ and $\hat{g}(R)$ at non-zero energies. When the energy is small, we derive accurate corrections to the zero-energy wave functions via perturbation theory, and we use this accurate representation of $\hat{f}(R)$ and $\hat{g}(R)$ at small energies to derive simple expressions for the threshold behavior of the QDT parameters. We accomplish this by matching the perturbative expressions for $\hat{f}(R)$ and $\hat{g}(R)$ near zero energy to the energy-dependent wave functions $f(R)$ and $g(R)$ (above threshold) or to the function $e^{-\kappa R}$ (below threshold).

2.6.1 Zero-Energy Solutions

For the simple long-range potential $-C_6/R^6$, the radial Schrödinger equation has the following form,

$$-\frac{\mathrm{d}^2\psi(R)}{\mathrm{d}R^2} + \frac{L(L+1)\psi(R)}{R^2} - \frac{\psi(R)}{R^6} = E\psi(R). \tag{2.50}$$

We can analytically solve this equation at $E = 0$. Here, the internuclear separation R is in units of the natural length scale $\beta = (2\mu C_6/\hbar^2)^{1/4}$ of the potential $-C_6/R^6$, and the energy E is in units of the natural energy scale $E_\beta = \hbar^2/2\mu\beta^2$, where μ is the reduced mass. We describe particular solutions to equation (2.50) at zero energy in terms of two linearly independent solutions $\chi_0^+(R)$ and $\chi_0^-(R)$,

$$\chi_0^+(R) = \sqrt{R}J_{-\frac{1}{4}(2L+1)}(1/2R^2) \xrightarrow{R\to\infty} \frac{2^{L+1/2}R^{L+1}}{\Gamma(3/4 - L/2)} \tag{2.51a}$$

$$\chi_0^-(R) = \sqrt{R}J_{\frac{1}{4}(2L+1)}(1/2R^2) \xrightarrow{R\to\infty} \frac{2^{-(L+1/2)}R^{-L}}{\Gamma(L/2 + 5/4)}, \tag{2.51b}$$

where $J_\nu(x)$ is the Bessel function of the first kind.

For all energies, we define two linearly independent reference wave functions $\hat{f}(R)$ and $\hat{g}(R)$ with the following boundary conditions at $R_\mathrm{x} << 1$,

$$\hat{f}(R) = \frac{1}{\sqrt{k(R)}}\sin\Big(\int_{R_\mathrm{x}}^{R} k(R')\mathrm{d}R' + \phi\Big) \quad \text{at } R = R_\mathrm{x} \tag{2.52a}$$

$$\hat{g}(R) = -\frac{1}{\sqrt{k(R)}}\cos\Big(\int_{R_\mathrm{x}}^{R} k(R')\mathrm{d}R' + \phi\Big) \quad \text{at } R = R_\mathrm{x}. \tag{2.52b}$$

Here, ϕ is a phase that is constant in R and energy, and $k(R) = \sqrt{E + 1/R^6}$. The set of equations (2.52) and their full radial derivatives define $\hat{f}(R)$ and $\hat{g}(R)$.

We demand that $\hat{g}(R)$ coincides (up to a normalization) with the solution $\chi_0^-(R)$ at zero energy. Hence, we write $\hat{f}(R)$ and $\hat{g}(R)$ in terms of $\chi_0^+(R)$ and $\chi_0^-(R)$ at zero energy by defining two constants of normalization N_1 and N_2 and a constant phase α,

$$\hat{f}(R, E=0) = N_2 \left(\chi_0^+(R) + \tan\alpha \chi_0^-(R)\right) \tag{2.53a}$$

$$\hat{g}(R, E=0) = N_1 \chi_0^-(R). \tag{2.53b}$$

By considering the small-R limit of our zero-energy solutions and reference wave functions,

$$\chi_0^+(R) \xrightarrow{R<<1} \frac{2}{\sqrt{\pi}} R^{3/2} \sin\left(-\frac{1}{2R^2} - \frac{L\pi}{4} + \frac{5\pi}{8}\right) \tag{2.54a}$$

$$\chi_0^-(R) \xrightarrow{R<<1} -\frac{2}{\sqrt{\pi}} R^{3/2} \cos\left(-\frac{1}{2R^2} + \frac{L\pi}{4} - \frac{5\pi}{8}\right) \tag{2.54b}$$

$$\hat{f}(R, E=0) \xrightarrow{R<<1} R^{3/2} \sin\left(-\frac{1}{2R^2} + \frac{1}{2R_{\mathrm{x}}^2} + \phi\right) \tag{2.54c}$$

$$\hat{g}(R, E=0) \xrightarrow{R<<1} -R^{3/2} \cos\left(-\frac{1}{2R^2} + \frac{1}{2R_{\mathrm{x}}^2} + \phi\right), \tag{2.54d}$$

we use the sets of equations (2.52) and (2.53) to determine the four unknown constants,

$$N_1 = \frac{\sqrt{\pi}}{2} \tag{2.55a}$$

$$\phi = -\frac{1}{2R_{\mathrm{x}}^2} + \frac{L\pi}{4} - \frac{5\pi}{8} \tag{2.55b}$$

$$\tan\alpha = (-1)^{L+1} \sin\left(\frac{2L+1}{4}\pi\right) \tag{2.55c}$$

$$N_2 = -\frac{\sqrt{\pi}}{2\sin\left(\frac{2L+1}{4}\pi\right)}. \tag{2.55d}$$

2.6.2 Perturbation Theory

At zero energy, we have exact expressions for the wave functions $\hat{f}(R)$ and $\hat{g}(R)$; however, it is not immediately obvious whether or not the zero-energy wave functions are good approximations at large $R >> 1$ and small energy $E << 1$. At small energy, both $\hat{f}(R)$ and $\hat{g}(R)$ grow with R before reaching their asymptotic limits, but only $\hat{f}(R)$ grows at exactly zero energy. Since $\hat{f}(R)$ has a contribution from $\chi_0^+(R)$ and $\chi_0^-(R)$ at zero energy, matching $\hat{f}(R)$ to finite-energy wave

functions is straightforward. However, $\hat{g}(R)$ only has a contribution from $\chi_0^-(R)$ at zero energy, and the contribution to $\hat{g}(R)$ from $\chi_0^+(R)$ at small energy is unknown. In order to match our zero-energy wave functions onto growing, finite-energy wave functions at large R, we must find the contribution to $\hat{g}(R)$ from $\chi_0^+(R)$. This is accomplished by performing a perturbation in E.

Because we plan to match wave functions at finite R, we choose a Green's function which preserves the boundary conditions of $\hat{g}(R)$ at $R_{\rm x}$ [64],

$$G(R,R') = \begin{cases} 0 & \text{if } R < R' \\ \frac{\chi_0^+(R)\chi_0^-(R') - \chi_0^-(R)\chi_0^+(R')}{(N_1 N_2)^{-1}} & \text{if } R > R'. \end{cases} \tag{2.56}$$

Hence, there is an integral equation for $\hat{g}(R)$ at small energy,

$$\begin{aligned} \hat{g}(R, E << 1) =& \hat{g}(R, E=0) + E\int_0^R G(R,R')\hat{g}(R', E=0)\mathrm{d}R' && \text{(2.57a)} \\ =& N_1\chi_0^-(R) + EN_1^2N_2\chi_0^+(R)\int_0^R (\chi_0^-(R'))^2\mathrm{d}R' \\ & - EN_1^2N_2\chi_0^-(R)\int_0^R \chi_0^+(R')\chi_0^-(R')\mathrm{d}R', && \text{(2.57b)} \end{aligned}$$

where we have used equation (2.53b) to replace $\hat{g}(R)$ at zero energy. We analytically solve these integrals and expand them in powers of R at large R,

$$\int_0^R (\chi_0^-(R'))^2\mathrm{d}R' \xrightarrow{R>>1} \frac{4}{(2L+3)(2L-1)\pi} - \frac{2^{-(2L+1)}R^{1-2L}}{(2L-1)\Gamma(5/4+L/2)^2} \tag{2.58a}$$

$$\int_0^R \chi_0^-(R')\chi_0^+(R')\mathrm{d}R' \xrightarrow{R>>1} \frac{4\cos\left(\frac{2L+1}{4}\pi\right)}{(2L+3)(2L-1)\pi} + \frac{2\sin\left(\frac{2L+1}{4}\pi\right)R^2}{(2L+1)\pi}. \tag{2.58b}$$

By using this correction to the zero-energy $\hat{g}(R)$ and by approximating $\hat{f}(R)$ with its zero-energy limit, we have complete descriptions of the reference wave functions at large R and small energy,

$$\hat{f}(R) \xrightarrow[E<<1]{R>>1} N_2\left(\frac{2^{L+1/2}R^{L+1}}{\Gamma(3/4-L/2)} + \tan\alpha\frac{2^{-(L+1/2)}R^{-L}}{\Gamma(5/4+L/2)}\right) \tag{2.59a}$$

$$\begin{aligned} \hat{g}(R) \xrightarrow[E<<1]{R>>1}& N_1\frac{2^{-(L+1/2)}R^{-L}}{\Gamma(5/4+L/2)} \\ & + EN_1^2N_2\left(\frac{2^{L+5/2}R^{L+1}}{\Gamma(3/4-L/2)(2L+3)(2L-1)\pi} - \frac{2^{-L+1/2}\sin\left(\frac{2L+1}{4}\pi\right)R^{-L+2}}{\Gamma(5/4+L/2)(2L-1)\pi}\right) \\ & - EN_1^2N_2\left(\frac{2^{-L+3/2}\cos(\frac{2L+1}{4}\pi)R^{-L}}{\Gamma(5/4+L/2)(2L+3)(2L-1)\pi}\right). \end{aligned} \tag{2.59b}$$

2.6.3 Matching Wave Functions

The QDT parameters connect $\hat{f}(R)$ and $\hat{g}(R)$ with $f(R)$, $g(R)$, and $e^{-\kappa R}$. Since we have analytic expressions for all of these wave functions at large R and small energy, we use the definitions of the QDT parameters in section 2.3 to solve for their threshold behavior. Moreover, by expanding these wave functions in powers of R and comparing like terms, we derive simple formulas. We can use the asymptotic expansions of $\hat{f}(R)$ and $\hat{g}(R)$ at small energy in equations (2.59a) and (2.59b), but we still need to find similar expansions of $f(R)$ and $g(R)$ in this same parameter regime: $R >> 1$ and $E << 1$.

At large R, we write $f(R)$ and $g(R)$ in terms of spherical Bessel functions using equations (2.14) and (2.13),

$$f(R) \xrightarrow{R\to\infty} \frac{kR}{\sqrt{k}} \left(j(kR)\cos\eta - n(kR)\sin\eta\right) \tag{2.60a}$$

$$g(R) \xrightarrow{R\to\infty} \frac{kR}{\sqrt{k}} \left(n(kR)\cos\eta + j(kR)\sin\eta\right). \tag{2.60b}$$

The small-argument expansions of the spherical Bessel functions unveil the behavior of $f(R)$ and $g(R)$ at large R and small energy such that $kR << 1$,

$$f(R) \xrightarrow[kR<<1]{R>>1} \frac{1}{\sqrt{k}} \frac{(kR)^{L+1}}{(2L+1)!!}\cos\eta + \frac{1}{\sqrt{k}} \frac{(2L-1)!!}{(kR)^{L}}\sin\eta \tag{2.61a}$$

$$g(R) \xrightarrow[kR<<1]{R>>1} -\frac{1}{\sqrt{k}} \frac{(2L-1)!!}{(kR)^{L}}\cos\eta \left(1 + \frac{(kR)^2}{4L-2}\right) + \frac{1}{\sqrt{k}} \frac{(kR)^{L+1}}{(2L+1)!!}\sin\eta, \tag{2.61b}$$

where $k = \sqrt{E}$. We see that $f(R)$ has a term proportional to R^{L+1} and a term proportional to R^{-L}. Hence, we compare this function with $\hat{f}(R)$ term by term. The equation for $f(R)$ in equation (2.15),

$$\mathcal{A}^{-1/2} f(R) = \hat{f}(R), \tag{2.62}$$

leads to equations for the QDT parameters $\mathcal{A}$ and η,

$$\mathcal{A}^{1/2} = \frac{\Gamma(3/4 - L/2)k^{L+1/2}\cos\eta}{N_2 2^{L+1/2}(2L+1)!!} \tag{2.63a}$$

$$\sin\eta = \frac{N_2 \tan\alpha 2^{-(L+1/2)}\mathcal{A}^{1/2}k^{L+1/2}}{\Gamma(L/2+5/4)(2L-1)!!}, \tag{2.63b}$$

where matching powers of R^{L+1} leads to equation (2.63a) and matching powers of R^{-L} leads to equation (2.63b).

From equation (2.63) we find that $\tan\eta \propto k^{2L+1}$. Thus, for small k, we use the small-angle approximation, $\sin\eta \approx \eta$ and $\cos\eta \approx 1$, and we define the generalized scattering length $\bar{a}_L$,

$$\bar{a}_L = \left(\frac{\pi 2^{-(2L+3/2)}}{\Gamma(L/2+5/4)\Gamma(L+1/2)} \right)^{2/(2L+1)}. \tag{2.64}$$

We then rewrite our expressions for $\mathcal{A}$ and η in terms of $\bar{a}_L$,

$$\mathcal{A}^{1/2} = -(\bar{a}_L k)^{L+1/2} \tag{2.65a}$$

$$\eta = (-1)^{L+1}(\bar{a}_L k)^{2L+1}. \tag{2.65b}$$

Here, we have used the relations $(2n-1)!! = 2^n\Gamma(1/2+n)/\sqrt{\pi}$, where n is an integer, and $\sin(\pi z) = \pi/\Gamma(1-z)\Gamma(z)$ with $z = (2L+1)/4$. For $L > 1$ and small k, we know that the phase shift is dominated by a long-range phase shift proportional to k^4 [65], but the derivation above only yields the short-range contribution to the phase shift because we are matching wave functions under the centrifugal barrier. Since we know the long-range contribution analytically, we simply correct our expression for η by adding these contributions together,

$$\eta = (-1)^{L+1}(\bar{a}_L k)^{2L+1} + \frac{3\pi\Gamma(L-3/2)}{32\Gamma(L+7/2)}k^4. \tag{2.66}$$

The length scale $\bar{a}_L$ helps to greatly reduce the amount of unnecessary constants in the derivation of the remaining QDT parameters $\mathcal{G}$ and γ. Hence, we write our wave functions in terms of $\bar{a}_L$. At large R, the zero-energy solutions become,

$$\chi_0^+(R) \xrightarrow{R>>1} -\frac{1}{N_2}\sqrt{\bar{a}_L}\frac{(R/\bar{a}_L)^{L+1}}{(2L+1)!!} \tag{2.67a}$$

$$\chi_0^-(R) \xrightarrow{R>>1} \frac{1}{N_1}\sqrt{\bar{a}_L}\frac{(2L-1)!!}{(R/\bar{a}_L)^{L}}, \tag{2.67b}$$

and we have simple expressions for $\hat{f}(R)$ and $\hat{g}(R)$ at large R and small energy,

$$\hat{f}(R) \xrightarrow[E<<1]{R>>1} -\sqrt{\bar{a}_L}\frac{(R/\bar{a}_L)^{L+1}}{(2L+1)!!} + (-1)^L\sqrt{\bar{a}_L}\frac{(2L-1)!!}{(R/\bar{a}_L)^L} \tag{2.68a}$$

$$\begin{aligned}\hat{g}(R) \xrightarrow[E<<1]{R>>1} &\sqrt{\bar{a}_L}\frac{(2L-1)!!}{(R/\bar{a}_L)^L}\left(1+\frac{ER^2}{4L-2}+\frac{(-1)^L E}{(2L+3)(2L-1)}\right)\\ &-\frac{E}{(2L+3)(2L-1)}\sqrt{\bar{a}_L}\frac{(R/\bar{a}_L)^{L+1}}{(2L+1)!!}.\end{aligned} \tag{2.68b}$$

We derive the threshold behavior of the QDT parameter $\mathcal{G}$ by using the equation for $g(R)$ in equation (2.15),

$$\mathcal{A}^{1/2}g(R) = \hat{g}(R) + \mathcal{G}\hat{f}(R). \tag{2.69}$$

In this equation, we substitute $\hat{g}(R)$ and $g(R)$ with their expansions in equations (2.68b) and (2.61b), respectively, and we replace $\mathcal{A}$ by its threshold value in equation (2.65a). Thus, in the limit of large R and small, positive energy such that $kR << 1$, we separately evaluate the left hand side and right hand side of equation (2.69),

$$\mathcal{A}^{1/2}g(R) \xrightarrow[kR<<1]{R>>1} \sqrt{\bar{a}_L}\frac{(2L-1)!!}{(R/\bar{a}_L)^L}\left(1+\frac{(kR)^2}{4L-2}\right) + (-1)^L(\bar{a}_L k)^{4L+2}\sqrt{\bar{a}_L}\frac{(R/\bar{a}_L)^{L+1}}{(2L+1)!!} \tag{2.70a}$$

$$\begin{aligned}\hat{g}(R)+\mathcal{G}\hat{f}(R) \xrightarrow[kR<<1]{R>>1} &\sqrt{\bar{a}_L}\frac{(2L-1)!!}{(R/\bar{a}_L)^L}\left(1+\frac{(kR)^2}{4L-2}+\frac{(-1)^L k^2}{(2L+3)(2L-1)}+(-1)^L\mathcal{G}\right)\\ &-\sqrt{\bar{a}_L}\frac{(R/\bar{a}_L)^{L+1}}{(2L+1)!!}\left(\frac{k^2}{(2L+3)(2L-1)}+\mathcal{G}\right),\end{aligned} \tag{2.70b}$$

where $E = k^2$. Hence, the first two terms on the left hand side exactly cancel the first two terms on the right hand side, leading to the following equation,

$$\begin{aligned}(-1)^L(\bar{a}_L k)^{4L+2}\frac{(R/\bar{a}_L)^{L+1}}{(2L+1)!!} =& -\frac{(R/\bar{a}_L)^{L+1}}{(2L+1)!!}\left(\frac{k^2}{(2L+3)(2L-1)}+\mathcal{G}\right)\\ &+(-1)^L\frac{(2L-1)!!}{(R/\bar{a}_L)^L}\left(\frac{k^2}{(2L+3)(2L-1)}+\mathcal{G}\right).\end{aligned} \tag{2.71}$$

At large $R >> 1$, the terms proportional to R^{L+1} on the right hand side dominate the terms proportional to R^{-L} for all L and all k, independent of $\mathcal{G}$; therefore, neglecting the terms of order R^{-L} in this equation gives the threshold behavior of $\mathcal{G}$,

$$\mathcal{G} = (-1)^{L+1}(\bar{a}_L k)^{4L+2} - \frac{k^2}{(2L+3)(2L-1)}. \tag{2.72}$$

We derive the threshold behavior of γ in a way that is similar to the derivation of $\mathcal{G}$. Here, instead of matching to $g(R)$, we match the small-energy limit of $\hat{f}(R)$ and $\hat{g}(R)$ to the function $e^{-\kappa R}$ at large R. We again try to match wave functions at large R and small energy such that $\kappa R << 1$. Using equation (2.16), we define a constant of proportionality D,

$$\tan\gamma_i \hat{f}_i(R) + \hat{g}_i(R) \xrightarrow{R>>1} De^{-\kappa_i R}. \tag{2.73}$$

Using equation (2.68) for $\hat{f}(R)$ and $\hat{g}(R)$ and using the expansion of $e^{-\kappa R}$ in the limit $\kappa R << 1$, we arrive at the following equation,

$$\begin{aligned} D\sum_{n=0}^{\infty}\frac{(-\kappa R)^n}{n!} = &-\sqrt{\bar{a}_L}\frac{(R/\bar{a}_L)^{L+1}}{(2L+1)!!}\left(-\frac{\kappa^2}{(2L+3)(2L-1)}+\tan\gamma\right) \\ &+\sqrt{\bar{a}_L}\frac{(2L-1)!!}{(R/\bar{a}_L)^L}\left(1-\frac{(\kappa R)^2}{4L-2}-\frac{(-1)^L\kappa^2}{(2L+3)(2L-1)}+(-1)^L\tan\gamma\right), \end{aligned} \tag{2.74}$$

where $E=-\kappa^2$.

For $L=0$, we take the expansion of $e^{-\kappa R}$ out to first order in κ ($n=1$), and we neglect terms of order κ^2,

$$D(1-\kappa R) = \sqrt{\bar{a}_0}\left(1+\tan\gamma-\tan\gamma R/\bar{a}_0\right). \tag{2.75}$$

Matching constant terms and terms of order R leads to the following two equations with two unknowns,

$$D = \sqrt{\bar{a}_0}\left(1+\tan\gamma\right) \tag{2.76a}$$

$$-D\kappa = -\tan\gamma/\sqrt{\bar{a}_0}. \tag{2.76b}$$

Hence,

$$D = \frac{\tan\gamma}{\sqrt{\bar{a}_0}\kappa} \tag{2.76c}$$

$$\tan\gamma = \frac{1}{1-\bar{a}_0\kappa}, \tag{2.76d}$$

and we have a simple formula for $\tan\gamma$ in the threshold limit $\kappa << 1$ when $L=0$,

$$\tan\gamma = \bar{a}_0\kappa \quad \text{for } L=0. \tag{2.77}$$

For $L > 0$, we immediately see that matching powers of R in equation (2.74) is problematic due to the terms of order R^{-L} on the right hand side. Therefore, instead of matching in the limit $\kappa R << 1$, we simply let the wave functions take their asymptotic forms as $R \to \infty$, where $\kappa R >> 1$ even though $\kappa << 1$. That is, $e^{-\kappa R} \to 0$, and $\hat{f}(R)$ and $\hat{g}(R)$ are still well approximated by their expressions in equation (2.68). At large $R >> 1$, these wave functions are dominated by their contributions from R^{L+1}. Even the contribution to $\hat{g}(R)$ from R^{-L+2} is dominated by the contribution from R^{L+1} for $L > 0$, and equation (2.73) takes the simple form below,

$$0 = -\sqrt{\bar{a}_L}\frac{(R/\bar{a}_L)^{L+1}}{(2L+1)!!}\left(-\frac{\kappa^2}{(2L+3)(2L-1)} + \tan\gamma\right). \tag{2.78}$$

Hence, we have the following simple formulas for the threshold behavior of γ,

$$\gamma = \begin{cases} \bar{a}_0\kappa & \text{for } L = 0 \\ \frac{\kappa^2}{(2L+3)(2L-1)} & \text{for } L > 0. \end{cases} \tag{2.79}$$

2.7 Summary

We have identified a choice of reference wave functions that allows QDT to describe high-partial-wave cold collisions. Our specific standardization of reference wave functions has produced a numerically stable calculation of high-partial-wave QDT parameters that are smooth in energy and magnetic field. Simple power laws describe all of these parameters at ultracold energies, and we have derived accurate expressions for these parameters in the threshold regime for potentials dominated by $-C_6/R^6$ at long range.

Chapter 3

Perturbative Multichannel Quantum Defect Theory

3.1 Introduction

Previous applications of MQDT successfully describe atomic collisions [29,34], including collisions of high orbital angular momentum L [54]. These studies mostly neglect long-range anisotropic interactions, as they are usually ignored within MQDT. However, it should be straightforward to perturbatively include them, along the lines formulated in references [37,66–68], for instance. Some studies utilize a distorted wave approximation to, for example, include coupling between energetically open channels [37], include non-adiabatic coupling to distant closed channels [69], or describe laser assisted photoassociation [70]. Since a Fano-Feshbach resonance (FR) occurs when the collision energy is nearly degenerate with a bound molecular state, the resonance positions can strongly depend on energetically closed scattering channels and their coupling to either other closed or open channels. Hence, we develop a distorted wave approximation that treats all channels on an equal footing.

For the perturbative MQDT calculation, we have the same goal as in chapter 2. We seek to accurately compute scattering observables in terms of quantities that are weakly dependent on energy and applied fields. In chapter 2, we accomplished this goal by writing the potential $V(R)$ in two parts beyond $R_{\rm m}$, and we use that same form of the potential in this chapter. Beyond $R_{\rm m}$,

$$V_{ij}(R) = V_i^{\rm lr}(R) + V'_{ij}(R). \tag{3.1}$$

In chapter 2, we let $V'(R) = 0$ beyond $R_{\rm m}$, and we accurately represented the asymptotic am-

plitude and phase of $M^{(0)}(R)$ of equation (2.10) in terms of the energy-smooth and field-smooth quantities $K^{\rm sr}$ and the QDT parameters. In this chapter, we consider the case when $V'(R)$ is not negligible beyond $R_{\rm m}$, and we do not set it equal to zero. In this case, $M^{(0)}(R)$ is not an exact solution to equation (2.2) beyond $R_{\rm m}$. Therefore, unlike chapter 2, $K^{\rm sr}$ and the QDT parameters do not contain all of the information needed to compute scattering observables. We instead determine scattering observables in the full potential $V(R)$ via perturbation theory, where $V'(R)$ is the perturbing potential.

One could formulate a perturbation theory in terms of a perturbation on the standard, physical scattering matrix $S^{\rm phys}$, which represents physical energy-normalized wave functions. This method has proven to be an accurate way to account for some perturbative long-range effects, as in reference [37], for example. However, the resonant structure of $S^{\rm phys}$ is difficult to handle in perturbation theory. In particular, the influence of the closed channel elements of the perturbing potential can significantly shift the positions of scattering resonances. These shifts can easily amount to large changes in $S^{\rm phys}$ that are not perturbative.

Instead, we directly perturb $K^{\rm sr}$ to most accurately account for the influence of $V'(R)$ beyond $R_{\rm m}$, including the shifts in resonance positions. We expect such a perturbation to be more accurate than directly perturbing $S^{\rm phys}$ because a small shift in $K^{\rm sr}$ can represent a large change in $S^{\rm phys}$. One can see from the set of equations (2.30) that $K^{\rm sr}_{\rm QQ} + \cot\gamma$ determines the positions of poles in $S^{\rm phys}$, which correspond to the positions of FRs, and a small change in $K^{\rm sr}$ can shift the position of those resonances. As we demonstrate in section 4.4, the closed channel elements of the perturbation $V'(R)$ can shift the positions of FRs well beyond the widths of those resonances, amounting to a large change in $S^{\rm phys}$.

Moreover, directly perturbing $K^{\rm sr}$ allows us to maintain the numerical efficiency of MQDT. Just as $K^{\rm sr}$ gains its weak dependence on energy and field because it represents the WKB-like normalized wave function matrix $M(R)$ at $R_{\rm m}$, we demand that the perturbed short-range K-matrix $K^{\rm sr'}$ also represents a WKB-like normalized wave function. Below, we derive an approximation to the perturbed scattering matrix $S^{\rm phys'}$ in terms of $K^{\rm sr'}$ and other quantities that are

weakly dependent on energy and field. To avoid confusion with chapter 2, we mark the reused symbols for B, C, $\mathcal{N}$, all constant K-matrices, and the physical S-matrix with a prime to denote the "perturbed" version.

3.2 The Green's Function Method

Unlike in chapter 2, we cannot accurately describe the long-range physics by solving equation (2.9) when $V'(R) \neq 0$. Instead, we use the Green's function method to propagate $M(R)$ from its boundary conditions at $R_{\rm m}$ to $R \geq R_{\rm m}$. Since we know the exact behavior of $M(R)$ at $R_{\rm m}$ ($M(R) = M^{(0)}(R)$ at $R_{\rm m}$), we choose a channel-dependent outward-propagating Green's function that preserves the value of a solution and its derivative at $R_{\rm m}$ [64],

$$G_i^{(+)}(R,R') = \begin{cases} 0 & \text{if } R < R' \\ \hat{f}_i(R)\hat{g}_i(R') - \hat{g}_i(R)\hat{f}_i(R') & \text{if } R > R'. \end{cases} \tag{3.2}$$

The Green's function $G^{(+)}(R,R')$ solves the following differential equation in the region $R_{\rm m} \leq R < \infty$,

$$\left(-\frac{{\rm d}^2}{{\rm d}R^2} + \frac{L_i(L_i+1)}{R^2} + V_i^{\rm lr}(R) - E_i\right) G_i^{(+)}(R,R') = \delta(R-R'). \tag{3.3}$$

An integral equation describes $M(R)$ beyond $R_{\rm m}$,

$$M_{ij}(R) = M_{ij}^{(0)}(R) - \int_{R_{\rm m}}^{\infty} G_i^{(+)}(R,R') \sum_k^N V'_{ik}(R') M_{kj}(R') {\rm d}R'. \tag{3.4}$$

Using the expression for $G^{(+)}(R,R')$ in equation (3.2) and the expression for $M^{(0)}(R)$ in equation (2.10), we explicitly rewrite equation (3.4) in terms of the reference wave functions $\hat{f}(R)$ and $\hat{g}(R)$ and their radially dependent coefficients,

$$\begin{aligned} M_{ij}(R) =& \hat{f}_i(R)\delta_{ij} - \hat{g}_i(R)K_{ij}^{\rm sr} \\ &- \hat{f}_i(R) \int_{R_{\rm m}}^{R} \hat{g}_i(R') \sum_k^N V'_{ik}(R') M_{kj}(R') {\rm d}R' \\ &+ \hat{g}_i(R) \int_{R_{\rm m}}^{R} \hat{f}_i(R') \sum_k^N V'_{ik}(R') M_{kj}(R') {\rm d}R'. \end{aligned} \tag{3.5}$$

Taking the full first radial derivative of this equation, we have the following expression for the derivative of $M(R)$,

$$\begin{aligned}\frac{\mathrm{d}M_{ij}(R)}{\mathrm{d}R} =& \frac{\mathrm{d}\hat{f}_i(R)}{\mathrm{d}R}\delta_{ij} - \frac{\mathrm{d}\hat{g}_i(R)}{\mathrm{d}R}K_{ij}^{\mathrm{sr}} \\ &- \frac{\mathrm{d}\hat{f}_i(R)}{\mathrm{d}R}\int_{R_\mathrm{m}}^{R}\hat{g}_i(R')\sum_k^N V'_{ik}(R')M_{kj}(R')\mathrm{d}R' \\ &+ \frac{\mathrm{d}\hat{g}_i(R)}{\mathrm{d}R}\int_{R_\mathrm{m}}^{R}\hat{f}_i(R')\sum_k^N V'_{ik}(R')M_{kj}(R')\mathrm{d}R'. \end{aligned} \tag{3.6}$$

Note that equations (3.5) and (3.6) have the same form, except that the reference wave functions outside of the integrals in equation (3.5) are replaced by their derivatives in equation (3.6). Therefore, if a wave function has a similar integral representation in the rest of this chapter, we simply write an equation for the wave function as a short-handed notation that represents the wave function and its derivative in the analogous form.

Because the reference wave functions $\hat{f}(R)$ and $\hat{g}(R)$ are solutions to equation (2.9) and because $M(R)$ is a set of solutions to equation (2.2), $M(R)$ is not a constant linear combination of reference wave functions in the region $R \geq R_\mathrm{m}$ when $V'(R) \neq 0$. Although $M^{(0)}(R)$ may approximately represent $M(R)$ beyond R_m when $V'(R)$ is small, this representation cannot be exact. In the full potential $V(R)$, the reference wave functions $\hat{f}(R)$ and $\hat{g}(R)$ and the two radially dependent matrices $I(R)$ and $J(R)$ exactly represent $M(R)$ beyond R_m,

$$M_{ij}(R) = \hat{f}_i(R)I_{ij}(R) - \hat{g}_i(R)J_{ij}(R). \tag{3.7}$$

Coefficients of this type are familiar in the variable phase formulation of scattering [71]. From equations (3.5) and (3.6), we deduce integral equations for $I(R)$ and $J(R)$,

$$I_{ij}(R) = \delta_{ij} - \int_{R_\mathrm{m}}^{R}\hat{g}_i(R')\sum_k^N V'_{ik}(R')M_{kj}(R')\mathrm{d}R' \tag{3.8a}$$

$$J_{ij}(R) = K_{ij}^{\mathrm{sr}} - \int_{R_\mathrm{m}}^{R}\hat{f}_i(R')\sum_k^N V'_{ik}(R')M_{kj}(R')\mathrm{d}R'. \tag{3.8b}$$

In scattering theory, it is not the separate matrices $I(R)$ and $J(R)$ that are of particular importance. Rather, it is their ratio $\mathcal{K}(R) = J(R)I(R)^{-1}$ that determines scattering observables.

In terms of $\mathcal{K}(R)$, $M(R)$ takes the following form,

$$M(R) = \left(\hat{f}(R) - \hat{g}(R)\mathcal{K}(R)\right) I(R). \tag{3.9}$$

Using the derivatives of $I(R)$ and $J(R)$ in the set of equations (3.8), we derive a differential equation for $\mathcal{K}(R)$ in the region $R \geq R_{\mathrm{m}}$,

$$\begin{aligned}
\frac{\mathrm{d}\mathcal{K}(R)}{\mathrm{d}R} =& \frac{\mathrm{d}J(R)}{\mathrm{d}R} I(R)^{-1} + J(R)\frac{\mathrm{d}(I^{-1}(R))}{\mathrm{d}R} && \text{(3.10a)}\\
=& \frac{\mathrm{d}J(R)}{\mathrm{d}R} I^{-1}(R) - \mathcal{K}(R)\frac{\mathrm{d}I(R)}{\mathrm{d}R} I^{-1}(R) && \text{(3.10b)}\\
=& -\left(\hat{f}(R) - \hat{g}(R)\mathcal{K}(R)\right)^{T} V'(R) \left(\hat{f}(R) - \hat{g}(R)\mathcal{K}(R)\right). && \text{(3.10c)}
\end{aligned}$$

Integrating equation (3.10c) gives an integral equation for $\mathcal{K}(R)$ in the region $R \geq R_{\mathrm{m}}$,

$$\mathcal{K}(R) = K^{\mathrm{sr}} - \int_{R_{\mathrm{m}}}^{R} \left(\hat{f}(R') - \hat{g}(R')\mathcal{K}(R')\right)^{T} V'(R') \left(\hat{f}(R') - \hat{g}(R')\mathcal{K}(R')\right) \mathrm{d}R'. \tag{3.11}$$

Hence, the quantity $\mathcal{K}(R)$ is best understood as a radially dependent short-range K-matrix, and we consider K^{sr} to be a boundary condition on $\mathcal{K}(R)$ at R_{m}. Equations (3.5) and (3.11) are exact, and they form the starting point for perturbation theory.

3.3 The Distorted Wave Approximation

In this section, we use the distorted wave approximation to derive an approximate expression for the perturbed physical scattering matrix $S^{\mathrm{phys}'}$. Just as the unperturbed scattering matrix only depends on K^{sr} and the QDT parameters, which can be easily interpolated over a wide range of energy and applied fields, we aim to write $S^{\mathrm{phys}'}$ in terms of a perturbed short-range K-matrix and other quantities that weakly depend on energy and field.

3.3.1 The Near Zone

The most straightforward way to derive an expression for $S^{\mathrm{phys}'}$ in terms of a short-range K-matrix is to use equation (3.11) to propagate $\mathcal{K}(R)$ through the entire range of the potential $V'(R)$ and write $S^{\mathrm{phys}'}$ in terms of the asymptotic value of $\mathcal{K}(R)$. We can simply obtain the distorted

wave approximation for $\mathcal{K}(R)$ in the region $R \geq R_{\rm m}$ by replacing $\mathcal{K}(R')$ inside the integral on the right hand side of equation (3.11) by $K^{\rm sr}$,

$$\mathcal{K}(R) \approx K^{\rm sr} - \int_{R_{\rm m}}^{R} \left(\hat{f}(R') - \hat{g}(R')K^{\rm sr}\right)^T V'(R') \left(\hat{f}(R') - \hat{g}(R')K^{\rm sr}\right) {\rm d}R'. \tag{3.12}$$

Because $\mathcal{K}(R)$ is equal to $K^{\rm sr}$ at $R \geq R_{\rm m}$ when $V'(R) = 0$, equation (3.12) is a standard first-order distorted wave approximation. This approximation for $\mathcal{K}(R)$ is equivalent to approximating $\hat{f}(R') - \hat{g}(R')\mathcal{K}(R')$ inside the integral on the right hand side of equation (3.11) by $M^{(0)}(R')$. More compactly, we write this approximation to $\mathcal{K}(R)$ in terms of $M^{(0)}(R')$,

$$\mathcal{K}(R) \approx K^{\rm sr} - \int_{R_{\rm m}}^{R} M^{(0)T}(R')V'(R')M^{(0)}(R'){\rm d}R'. \tag{3.13}$$

However, the approximation to $\mathcal{K}(R)$ in equation (3.13) exponentially diverges in the limit $R \to \infty$. This divergence occurs because, for a general $K^{\rm sr}$, $M^{(0)}(R)$ exponentially diverges in the classically forbidden region of the asymptotically closed channels. Such a divergence produces a correction to $K^{\rm sr}$ that does not converge in the limit $R \to \infty$ and quickly becomes too big to be considered perturbative in any sense. Note that the integral on the right hand side of equation (3.13) is divergent for any closed-channel perturbation that decays as a power of R beyond $R_{\rm m}$, independent of the magnitude of the perturbation.

Therefore, we only use equation (3.13), as written, to propagate $\mathcal{K}(R)$ in the short-range region where all channels remain locally open. This region is located between the matching radius $R_{\rm m}$ and the smallest outer classical turning point $R_{{\rm t}_i}$ of any asymptotically closed channel i. We order these turning points from 1 to $N_{\rm c}$ according to their increasing magnitude, making $R_{\rm t_1}$ the smallest one. Hence, we use equation (3.13) to write the approximate value of $\mathcal{K}(R)$ at $R_{\rm t_1}$,

$$\mathcal{K}(R_{\rm t_1}) \approx K^{\rm sr} - \int_{R_{\rm m}}^{R_{\rm t_1}} M^{(0)T}(R')V'(R')M^{(0)}(R'){\rm d}R'. \tag{3.14}$$

3.3.2 The Danger Zone

To account for the influence of $V'(R)$ beyond $R_{\rm t_1}$ in terms of quantities that weakly depend on energy and applied fields, we devise a alternative perturbation theory that does not involve integrals

over exponentially divergent wave functions, while simultaneously casting this perturbation in terms of a perturbed short-range K-matrix $K^{\mathrm{sr}'}$. We accomplish this by finding the particular linear combination of $\hat{f}(R)$ and $\hat{g}(R)$ that represents $\hat{F}(R)$ in the region $R \geq R_{\mathrm{t}_1}$. Analogous to $\hat{F}^{(0)}(R)$ of chapter 2, the columns of $\hat{F}(R)$ represent a set of solutions to equation (2.2) that vanish at the origin in all channels and also asymptotically vanish in the closed channels. We construct $\hat{F}(R)$ by taking linear combinations of the columns of $M(R)$ via the transformation $\hat{F}(R) = M(R)B'$, where B' plays the same role as B of chapter 2.

Unlike $M^{(0)}(R)$ of chapter 2, the wave function matrix $M(R)$ is not a constant linear combination of reference wave functions beyond R_{t_1} when $V'(R) \neq 0$. Therefore, we must perform the transformation $\hat{F}(R) = M(R)B'$ at a specific location in the region $R \geq R_{\mathrm{t}_1}$, and we call this location the elimination radius R_{e}. Analogous to the transformation $\hat{F}^{(0)}(R) = M^{(0)}(R)B$ of chapter 2.3, the transformation $\hat{F}(R) = M(R)B'$ needs to enforce asymptotically vanishing boundary conditions on the closed channels of $\hat{F}(R)$, even though $V'(R)$ may influence the behavior of $\hat{F}(R)$ beyond R_{e}. Hence, we set the closed-channel elements of $V'(R)$ to zero beyond R_{e}, eliminating the closed channels from the scattering problem. This allows the linear combination of reference wave functions that represents the closed channels of $\hat{F}(R)$ at R_{e} to accurately represent their asymptotic behavior as well. We represent the closed channels of $\hat{F}(R)$ by the $N_{\mathrm{c}} \times N_{\mathrm{o}}$ matrix $\hat{F}_{\mathrm{Q}}(R)$, and we enforce asymptotically vanishing boundary conditions on the closed channels of $\hat{F}(R)$ by demanding that $\hat{F}_{\mathrm{Q}}(R)$ is proportional to $\chi^{-}_{\mathrm{Q}}(R)$ at R_{e}. Therefore, the discussion that follows is similar to chapter 2, except that we use perturbed wave functions to accommodate $V'(R)$.

In order to represent $\hat{F}(R)$ at R_{e} in terms of quantities that weakly depend on energy and field, we write $\hat{F}(R)$ at R_{e} as a linear combination of $\hat{f}(R)$ and $\hat{g}(R)$ in each channel. We represent the open channels of $\hat{F}(R)$ by the $N_{\mathrm{o}} \times N_{\mathrm{o}}$ matrix $\hat{F}_{\mathrm{P}}(R)$, and we demand that $\hat{F}_{\mathrm{P}}(R)$ has the following form at R_{e},

$$\hat{F}_{\mathrm{P}}(R) = \hat{f}_{\mathrm{P}}(R) - \hat{g}_{\mathrm{P}}(R)\tilde{K}' \quad \text{at } R = R_{\mathrm{e}}. \tag{3.15}$$

This equation defines the $N_{\mathrm{o}} \times N_{\mathrm{o}}$ matrix $\tilde{K}'$. In the closed channels, we demand that $\hat{F}_{\mathrm{Q}}(R)$ is

proportional to $\chi_{\rm Q}^{-}(R)$ at $R_{\rm e}$,

$$\hat{F}_{\rm Q}(R) = \left(\hat{f}_{\rm Q}(R) + \hat{g}_{\rm Q}(R)\cot\gamma\right)C' \quad \text{at } R = R_{\rm e} \tag{3.16a}$$

$$= \chi_{\rm Q}^{-}(R)\csc\gamma C' \quad \text{at } R = R_{\rm e}. \tag{3.16b}$$

This equation defines the $N_{\rm c} \times N_{\rm o}$ matrix C'. Even though the set of equations (3.16) defines C' at $R_{\rm e}$, this linear combination of $\hat{f}(R)$ and $\hat{g}(R)$ represents $\hat{F}_{\rm Q}(R)$ at $R \geq R_{\rm e}$ because we have set all closed-channel elements of $V'(R)$ to zero beyond $R_{\rm e}$. Equations (3.15) and (3.16) have the same form as equations (2.20) and (2.21) of chapter 2, except that the perturbed constants C' and $\tilde{K}'$ replace C and $\tilde{K}$.

Because the set of equations (3.15) and (3.16) define C' and $\tilde{K}'$ at $R_{\rm e}$, we must determine the behavior of $\hat{F}(R)$ at $R_{\rm e}$ in order to solve for C' and $\tilde{K}'$. The transformation $\hat{F}(R) = M(R)B'$ describes the behavior of $\hat{F}(R)$ in terms of $M(R)$, and we know the exact boundary conditions of $M(R)$ at $R_{\rm m}$. Hence, we can determine the behavior of $\hat{F}(R)$ at $R_{\rm e}$ by using the Green's function method of section 3.2 to propagate $M(R)$ in the region $R_{\rm m} \leq R \leq R_{\rm e}$. In fact, since we can use the approximation to $\mathcal{K}(R_{\rm t_1})$ in equation (3.14), we only need to propagate $M(R)$ in the region $R_{\rm t_1} \leq R \leq R_{\rm e}$ in order to solve for C' and $\tilde{K}'$.

Similar to the propagation of $\mathcal{K}(R)$ beyond $R_{\rm t_1}$, using equation (3.5) to propagate $M(R)$ from $R_{\rm t_1}$ to $R_{\rm e}$ leads to an approximate representation of $\hat{F}(R)$ at $R_{\rm e}$ in terms of integrals that exponentially diverge with increasing $R_{\rm e}$. In order to devise a perturbation theory that avoids these divergences, we demonstrate the nature of the divergence we encounter when using equation (3.5). Explicitly writing equation (3.5) in terms of $I(R_{\rm t_1})$ and $J(R_{\rm t_1})$ produces the following equation,

$$\begin{aligned} M(R) =& \hat{f}(R)I(R_{\rm t_1}) - \hat{g}(R)J(R_{\rm t_1}) \\ &- \hat{f}(R)\int_{R_{\rm t_1}}^{R} \hat{g}(R')V'(R')M(R'){\rm d}R' \\ &+ \hat{g}(R)\int_{R_{\rm t_1}}^{R} \hat{f}(R')V'(R')M(R'){\rm d}R'. \end{aligned} \tag{3.17}$$

We make the standard distorted wave approximation by replacing $M(R')$ inside the integrals on the right hand side of equation (3.17) by $\hat{f}(R')I(R_{\rm t_1}) - \hat{g}(R')J(R_{\rm t_1})$. Because $I(R')$ and $J(R')$

are not constant functions of R', the resulting equation for $M(R)$ is only approximately correct. Plugging this approximation for $M(R)$ into the transformation $\hat{F}(R) = M(R)B'$ at $R_{\rm e}$ produces the following approximate representation of $\hat{F}(R)$ at $R_{\rm e}$,

$$\begin{aligned}\hat{F}(R) \approx & \left(\hat{f}(R)I(R_{\rm t_1}) - \hat{g}(R)J(R_{\rm t_1})\right)B' \\ & - \hat{f}(R)\int_{R_{\rm t_1}}^{R_{\rm e}} \hat{g}(R')V'(R')\left(\hat{f}(R')I(R_{\rm t_1}) - \hat{g}(R')J(R_{\rm t_1})\right)B'\mathrm{d}R' \\ & + \hat{g}(R)\int_{R_{\rm t_1}}^{R_{\rm e}} \hat{f}(R')V'(R')\left(\hat{f}(R')I(R_{\rm t_1}) - \hat{g}(R')J(R_{\rm t_1})\right)B'\mathrm{d}R' \quad \text{at } R = R_{\rm e}, \end{aligned} \tag{3.18}$$

where we bring the constant B' inside the integrals over R'.

Setting $\hat{F}(R)$ in equation (3.18) equal to $\hat{F}(R)$ in the set of equations (3.15 - 3.16) produces a set of equations for B', C' and $\tilde{K}'$. At $R_{\rm e}$, the transformation $\hat{F}(R) = M(R)B'$ has the following form,

$$\hat{F}(R) = \left(\hat{f}(R)I(R_{\rm e}) - \hat{g}(R)J(R_{\rm e})\right)B' \quad \text{at } R = R_{\rm e}. \tag{3.19}$$

Hence, equation (3.16) demands that the closed channels of $\left(\hat{f}(R)I(R_{\rm e}) - \hat{g}(R)J(R_{\rm e})\right)B'$ are proportional to $\chi_{\rm Q}^{-}(R)$. However, the matrix $\left(\hat{f}(R')I(R_{\rm t_1}) - \hat{g}(R')J(R_{\rm t_1})\right)B'$ appears inside the integrals on the right hand side of equation (3.18). Because $I(R_{\rm t_1}) \neq I(R_{\rm e})$ and $J(R_{\rm t_1}) \neq J(R_{\rm e})$ when $V'(R) \neq 0$, the closed channels of $\left(\hat{f}(R')I(R_{\rm t_1}) - \hat{g}(R')J(R_{\rm t_1})\right)B'$ are not proportional to $\chi_{\rm Q}^{-}(R')$ and, therefore, exponentially diverge in the limit $R' \to \infty$. This causes the integrals on the right hand side of equation (3.18) and, therefore, the quantities B', C' and $\tilde{K}'$ to exponentially diverge as $R_{\rm e}$ increases. Because of this divergence, we devise an alternative method of perturbation theory in the region $R_{\rm t_1} \leq R \leq R_{\rm e}$.

To avoid exponentially divergent integrals, we take advantage of the fact that the representation of $\hat{F}(R)$ in equation (3.19) vanishes in closed channels as $R_{\rm e}$ increases. Using this property of $\hat{F}(R)$, we derive a distorted wave approximation for $\hat{F}(R)$ that eliminates the divergences introduced by $M(R)$. Because we demand that the representation of $\hat{F}(R)$ at $R_{\rm e}$ vanishes as $R_{\rm e}$ increases, we introduce a channel-dependent inward-propagating Green's function $G^{(-)}(R, R')$ that preserves

the value of a solution and its derivative at $R_{\rm e}$,

$$G_i^{(-)}(R,R') = \begin{cases} \hat{f}_i(R)\hat{g}_i(R') - \hat{g}_i(R)\hat{f}_i(R') & \text{if } R < R' \\ 0 & \text{if } R > R', \end{cases} \tag{3.20}$$

which is similar to the outward-propagating Green's function $G^{(+)}(R,R')$ in equation (3.2).

Using $G^{(-)}(R,R')$ instead of $G^{(+)}(R,R')$ leads to the following integral equation for $M(R)$,

$$\begin{aligned} M(R) =& \hat{f}(R)I(R_{\rm e}) - \hat{g}(R)J(R_{\rm e}) \\ & - \hat{f}(R)\int_{R_{\rm e}}^{R} \hat{g}(R')V'(R')M(R')\mathrm{d}R' \\ & + \hat{g}(R)\int_{R_{\rm e}}^{R} \hat{f}(R')V'(R')M(R')\mathrm{d}R'. \end{aligned} \tag{3.21}$$

We use equation (3.21) to propagate $M(R)$ from its boundary conditions at $R_{\rm e}$ (which we don't know) to $R_{\rm t_1} \leq R_{\rm e}$. We make the standard distorted wave approximation by replacing $M(R')$ inside the integral on the right hand side of equation (3.21) by $\hat{f}(R')I(R_{\rm e}) - \hat{g}(R')J(R_{\rm e})$. Using the transformation $\hat{F}(R) = M(R)B'$ at $R_{\rm e}$ produces the following approximate representation of $\hat{F}(R)$ at $R_{\rm e}$,

$$\begin{aligned} \hat{F}(R) \approx & \left(\hat{f}(R)I(R_{\rm t_1}) - \hat{g}(R)J(R_{\rm t_1})\right)B' \\ & - \hat{f}(R)\int_{R_{\rm t_1}}^{R_{\rm e}} \hat{g}(R')V'(R')\left(\hat{f}(R')I(R_{\rm e}) - \hat{g}(R')J(R_{\rm e})\right)B'\mathrm{d}R' \\ & + \hat{g}(R)\int_{R_{\rm t_1}}^{R_{\rm e}} \hat{f}(R')V'(R')\left(\hat{f}(R')I(R_{\rm e}) - \hat{g}(R')J(R_{\rm e})\right)B'\mathrm{d}R' \quad \text{at } R = R_{\rm e}, \end{aligned} \tag{3.22}$$

where we bring the constant B' inside the integrals over R' and reverse the order of the limits of integration from their order in equation (3.21). Unlike equation (3.18), which involves integrals over the quantity $\left(\hat{f}(R')I(R_{\rm t_1}) - \hat{g}(R')J(R_{\rm t_1})\right)B'$, equation (3.22) involves integrals over the quantity $\left(\hat{f}(R')I(R_{\rm e}) - \hat{g}(R')J(R_{\rm e})\right)B'$. Since the closed channels of $\left(\hat{f}(R')I(R_{\rm e}) - \hat{g}(R')J(R_{\rm e})\right)B'$ exponentially decay with increasing R', they do not cause the integrals in equation (3.22) to diverge as $R_{\rm e}$ increases.

Although B' eliminates the divergent behavior of the matrix $\hat{f}(R')I(R_{\rm e}) - \hat{g}(R')J(R_{\rm e})$, which appears inside the integrals on the right hand side of equation (3.22), $\hat{f}(R')$ and $\hat{g}(R')$ separately

appear to the left of $V'(R')$ in these integrals, and the closed channels of these reference wave functions exponentially diverge as well. However, appendix A uses equation (3.22) to derive an approximate set of equations for B', C', and $\tilde{K}'$, and this set of equations shows that $\tilde{K}'$ only depends on asymptotically convergent integrals to first order in $V'(R)$. Because we derive all scattering observables from $\tilde{K}'$, we neglect the exponentially divergent integrals that lead to second order contributions to $\tilde{K}'$.

Appendix A further approximates the behavior of $\hat{F}(R)$ at $R_{\rm e}$ in order to approximately express this behavior in terms of a symmetric, perturbed short-range K-matrix $K^{\rm sr'}$ that weakly depends on energy and applied fields. We define $K^{\rm sr'}$ to be the value of $\mathcal{K}(R)$ at $R_{\rm e}$,

$$K^{\rm sr'} = \mathcal{K}(R_{\rm e}) = J(R_{\rm e})I(R_{\rm e})^{-1}. \tag{3.23}$$

In terms of $K^{\rm sr'}$, $\hat{F}(R)$ takes the following form at $R_{\rm e}$,

$$\hat{F}(R) = \left(\hat{f}(R) - \hat{g}(R)K^{\rm sr'}\right) I(R_{\rm e})B' \quad \text{at } R = R_{\rm e}. \tag{3.24}$$

To derive $\tilde{K}'$ in terms of $K^{\rm sr'}$, we match two different representations of $\hat{F}(R)$ together at $R_{\rm e}$. For this matching, we set the representation of $\hat{F}(R)$ in equations (3.15) and (3.16) equal to the representation of $\hat{F}(R)$ in equation (3.24). Because these representations of $\hat{F}(R)$ have the same form as the representations of $\hat{F}^{(0)}(R)$ in equations (2.20), (2.21), and (2.22), $\tilde{K}'$ has the same form as $\tilde{K}$ in equation (2.25b), except that we replace $K^{\rm sr}$ by its perturbed version $K^{\rm sr'}$,

$$\tilde{K}' = K^{\rm sr'}_{\rm PP} - K^{\rm sr'}_{\rm PQ}(K^{\rm sr'}_{\rm QQ} + \cot\gamma)^{-1}K^{\rm sr'}_{\rm QP}. \tag{3.25}$$

This equation defines the essential relationship between $\tilde{K}'$ and $K^{\rm sr'}$. Even though the quantity $K^{\rm sr'}$ and the QDT parameter γ are both weakly dependent on energy and field, they simply describe the resonant behavior of $\tilde{K}'$ through the matrix inverse in equation (3.25). The roots of $\det\left(K^{\rm sr'}_{\rm QQ} + \cot\gamma\right)$ approximately determine the positions of resonances.

Appendix A approximates $K^{\rm sr'}$ by deriving expressions for $I(R_{\rm e})$ and $J(R_{\rm e})$ that produce an approximate representation of $\hat{F}(R)$ at $R_{\rm e}$. Equation (A.24) of appendix A writes this approximation to $K^{\rm sr'}$ in terms of $K^{\rm sr}$ and the modified wave function matrix $\tilde{M}^{(0)}(R)$. We rewrite this

equation below,

$$K^{\mathrm{sr}'} \approx \mathcal{K}(R_{\mathrm{t}_1}) - \int_{R_{\mathrm{t}_1}}^{R_{\mathrm{e}}} \tilde{M}^{(0)T}(R')V'(R')\tilde{M}^{(0)}(R')\mathrm{d}R', \tag{3.26}$$

where equation (A.23) of appendix A defines $\tilde{M}^{(0)}(R)$. We rewrite this equation below,

$$\tilde{M}^{(0)}(R) = \begin{pmatrix} \hat{f}_{\mathrm{P}}(R) - \hat{g}_{\mathrm{P}}(R)K^{\mathrm{sr}}_{\mathrm{PP}} & -\hat{g}_{\mathrm{P}}(R)K^{\mathrm{sr}}_{\mathrm{PQ}} \\ -\chi^{-}_{\mathrm{Q}}(R)\cos\gamma K^{\mathrm{sr}}_{\mathrm{QP}} & \chi^{-}_{\mathrm{Q}}(R)\left(\sin\gamma - \cos\gamma K^{\mathrm{sr}}_{\mathrm{QQ}}\right) \end{pmatrix}. \tag{3.27}$$

Equation (3.27) shows that $\tilde{M}^{(0)}(R)$ is proportional to $\chi^{-}_{\mathrm{Q}}(R)$ in the closed channels. Therefore, the closed channels of $\tilde{M}^{(0)}(R)$ exponentially vanish in the limit $R \to \infty$, and the integral in equation (3.26) converges with increasing R_{e}, producing a finite expression for $K^{\mathrm{sr}'}$ in the limit $R_{\mathrm{e}} \to \infty$. Equation (3.27) also shows that we can easily construct $\tilde{M}^{(0)}(R)$ from $M^{(0)}(R)$ by replacing $\hat{g}_{\mathrm{Q}}(R)$ with $\chi^{-}_{\mathrm{Q}}(R)\cos\gamma$ and by replacing $\hat{f}_{\mathrm{Q}}(R)$ with $\chi^{-}_{\mathrm{Q}}(R)\sin\gamma$.

Substituting the approximation for $\mathcal{K}(R_{\mathrm{t}_1})$ in equation (3.14) into equation (3.26) produces the following approximation for $K^{\mathrm{sr}'}$,

$$K^{\mathrm{sr}'} \approx K^{\mathrm{sr}} - \int_{R_{\mathrm{m}}}^{R_{\mathrm{t}_1}} M^{(0)T}(R')V'(R')M^{(0)}(R')\mathrm{d}R' - \int_{R_{\mathrm{t}_1}}^{R_{\mathrm{e}}} \tilde{M}^{(0)T}(R')V'(R')\tilde{M}^{(0)}(R')\mathrm{d}R'. \tag{3.28}$$

This approximation for $K^{\mathrm{sr}'}$ is equivalent to approximating $\mathcal{K}(R)$ at R_{e} by replacing the quantity $\hat{f}(R') - \hat{g}(R')\mathcal{K}(R')$ inside the integral on the right hand side of equation (3.11) by $M^{(0)}(R')$ in the region $R_{\mathrm{m}} \le R \le R_{\mathrm{t}_1}$ and by the modified wave function matrix $\tilde{M}^{(0)}(R')$ in the region $R_{\mathrm{t}_1} \le R \le R_{\mathrm{e}}$. We do not expect this approximation for $K^{\mathrm{sr}'}$ to be numerically close to the approximation for $\mathcal{K}(R_{\mathrm{e}})$ implied by equation (3.13) because equation (3.13) is a poor approximation beyond R_{t_1}.

We use equation (3.28) to approximate $K^{\mathrm{sr}'}$ in the example problem of section 4.4, producing accurate scattering observables. In the example problem of section 4.4, which considers low-partial-wave collisions between alkali atoms, all of the outer turning points of the closed channels are close together. Other scattering problems, however, may have closed-channel turning points that are separated by a large distance. In particular, scattering problems with high partial waves or ro-vibrational excitations may benefit from an alternative approximation.

To account for such scattering problems, we develop a simple modification to the approximation for $K^{\mathrm{sr}'}$ in equation (3.26) that may achieve a higher accuracy. In this alternative approximation, we divide the region $R_{\mathrm{t}_1} \leq R \leq R_{\mathrm{e}}$ into segments separated by the successive closed channel turning points. We enumerate these segments by the index α, which runs from 1 to $N_{\mathrm{c}} - 1$. We define each segment α to be the region $R_{\mathrm{t}_\alpha} \leq R \leq R_{\mathrm{t}_{\alpha+1}}$.

In this alternative method, we evolve $\mathcal{K}(R)$ by approximating $\hat{f}(R') - \hat{g}(R')\mathcal{K}(R')$ inside the integral on the right hand side of equation (3.11) by a different version of $\tilde{M}^{(0)}(R')$ in each segment of the region $R_{\mathrm{t}_1} \leq R \leq R_{\mathrm{e}}$. Similar to the construction of $\tilde{M}^{(0)}(R)$ from $M^{(0)}(R)$, we construct $\tilde{M}^{(0)}_\alpha(R)$ from $M^{(0)}(R)$ by replacing $\hat{g}_i(R)$ with $\chi_i^-(R)\cos\gamma_i$ and by replacing $\hat{f}_i(R)$ with $\chi_i^-(R)\sin\gamma_i$. However, we only make these replacements in the asymptotically closed channels i that are also locally closed in segment α of this region. Hence, $K^{\mathrm{sr}'}$ takes the following form,

$$K^{\mathrm{sr}'} = K^{\mathrm{sr}} - \int_{R_{\mathrm{m}}}^{R_{\mathrm{t}_1}} M^{(0)T} V' M^{(0)} \mathrm{d}R' - \sum_{\alpha=1}^{N_{\mathrm{c}}-1} \int_{R_{\mathrm{t}_\alpha}}^{R_{\mathrm{t}_{\alpha+1}}} \tilde{M}^{(0)T}_\alpha V' \tilde{M}^{(0)}_\alpha \mathrm{d}R' - \int_{R_{\mathrm{t}_{N_{\mathrm{c}}}}}^{R_{\mathrm{e}}} \tilde{M}^{(0)T} V' \tilde{M}^{(0)} \mathrm{d}R'. \tag{3.29}$$

Conveniently, the closed-channel reference wave functions that are exponentially divergent beyond their outer classical turning points do not appear in the integral from R_{t_1} to R_{e} in equation (3.28) or equation (3.29). Hence, we can choose R_{e} anywhere in the region $R \geq R_{\mathrm{t}_1}$ without introducing integrals over exponentially divergent wave functions in the closed channels. However, open channels that are near threshold and have a centrifugal barrier play an important role in ultracold collisions. When such a channel exists, the open channels of the WKB-like normalized matrix $\tilde{M}^{(0)}(R)$ experience a rapid power-law growth under the centrifugal barrier. Similar to the propagation of $\mathcal{K}(R)$ beyond R_{t_1}, the rapid growth of $\tilde{M}^{(0)}(R)$ in the classically forbidden region under a centrifugal barrier leads to an approximation to $K^{\mathrm{sr}'}$ that quickly becomes too large to be considered perturbative in any sense, unless the perturbation $V'(R)$ is exactly zero in these channels. Therefore, we do not take the limit $R_{\mathrm{e}} \to \infty$, even though $K^{\mathrm{sr}'}$ does converge in this limit.

Instead, we must carefully choose the location $R_{\rm e}$ for each scattering problem. Ideally, we can increase $R_{\rm e}$ well beyond $R_{\rm t_1}$ and obtain a clear convergence in the closed channels of $K^{\rm sr'}$ before the open-channel elements of $K^{\rm sr'}$ grow out of control. This allows the matrix inverse of $K^{\rm sr'}_{\rm QQ} + \cot\gamma$ to describe the strongly resonant behavior of $S^{\rm phys'}$, analogous to how the matrix inverse of $K^{\rm sr}_{\rm QQ} + \cot\gamma$ describes the resonant behavior of $S^{\rm phys}$ in the set of equations (2.30). Maintaining this structure creates a maximally accurate perturbation on the position of resonances in terms of quantities that weakly depend on energy and field. We strive to increase $R_{\rm e}$ until we fully account for the influence of the closed-channel elements of $V'(R)$, keeping in mind that a smaller value of $R_{\rm e}$ may be required for certain problems, and we neglect the closed-channel elements of $V'(R)$ beyond $R_{\rm e}$.

In general, the outer classical turning point of a closed channel i has a value $R_{\rm t_i} \lesssim 1$. Beyond $R_{\rm t_i}$, the decaying amplitude of $\chi_i^-(R)$ in the classically forbidden region of channel i quickly diminishes the effect of $V'_{ij}(R)$ on the approximation for $K^{\rm sr'}$ in equation (3.28), where j is any channel. The open channel wave functions, however, have a significant amplitude well beyond the outer classical turning points of the closed channels. Hence, $R_{\rm e}$ creates a clear separation between our treatment of the short-range physics and our treatment of the long-range physics. The choice of $R_{\rm e} = 1$ is appropriate in this sense. In fact, we find that the choice of $R_{\rm e} = 1$ achieves an accurate approximation to scattering observables in the example problem of section 4.4.

3.3.3 The Far Zone

By performing the transformation $\hat{F}(R) = M(R)B'$ at $R_{\rm e}$ and by neglecting the closed-channel elements of $V'(R)$ beyond $R_{\rm e}$, we have effectively removed the closed channels from the scattering problem for $R > R_{\rm e}$. Beyond $R_{\rm e}$, we devise a perturbation theory that accurately accounts for the influence of the open-channel elements of $V'(R)$, while simultaneously maintaining the simple form of MQDT. Here, we derive an expression for $S^{\rm phys'}$ in terms of a perturbed energy-normalized K-matrix K'. We also write K' in terms of quantities that are weakly dependent on energy and field.

The matrix K' represents the asymptotic amplitude and phase of the wave function ma-

trix $F(R)$. Similar to $\hat{F}(R)$, $F(R)$ vanishes at the origin in all channels and asymptotically vanishes in the closed channels. However, unlike $\hat{F}(R)$, $F(R)$ is also energy-normalized. The energy-normalization of $F(R)$ forces the amplitude of $F(R)$ to remain fixed in the limit $R \to \infty$, and tunneling through the classically forbidden region under a centrifugal barrier causes the amplitude of $F(R)$ to shrink. Therefore, unlike the approximation for $K^{\mathrm{sr}'}$ in equation (3.28), which depends on the WKB-like normalized matrix $\tilde{M}(R)$, a perturbation theory for K' that depends on an energy-normalized wave function can remain perturbative, even when a large classically forbidden region exists in an open channel. Performing perturbation theory in terms of energy-normalized wave functions is natural from the point of view of Born-approximation treatments of scattering.

In order to obtain the energy-normalization of $F(R)$, we write the open channels of $F(R)$ in terms of the energy-normalized reference wave functions $f(R)$ and $g(R)$. We represent the open channels of $F(R)$ by the $N_{\mathrm{o}} \times N_{\mathrm{o}}$ matrix $F_{\mathrm{P}}(R)$,

$$F_{\mathrm{P}}(R) = f_{\mathrm{P}}(R) - g_{\mathrm{P}}(R)Z(R). \tag{3.30}$$

This equation defines the $N_{\mathrm{o}} \times N_{\mathrm{o}}$ matrix $Z(R)$. Here, we demand that the coefficient in front of $f_{\mathrm{P}}(R)$ is equal to the $N_{\mathrm{o}} \times N_{\mathrm{o}}$ identity matrix, forcing $F_{\mathrm{P}}(R)$ to have the same energy-normalization as $f_{\mathrm{P}}(R)$.

We find the equation of motion for $Z(R)$ by substituting the exact expression for $M(R)$ in equation (3.5), which uses the outward propagating Green's function $G^{(+)}(R, R')$, into the transformation $\hat{F}(R) = M(R)B'$. Explicitly writing the open channels of this equation in terms of $\tilde{K}'$ and neglecting the closed-channel elements of $V'(R)$ beyond R_{e} produces the following equation for $\hat{F}_{\mathrm{P}}(R)$ in the region $R \geq R_{\mathrm{e}}$,

$$\begin{aligned}\hat{F}_{\mathrm{P}}(R) =& \hat{f}_{\mathrm{P}}(R) - \hat{g}_{\mathrm{P}}(R)\tilde{K}' - \hat{f}_{\mathrm{P}}(R)\int_{R_{\mathrm{e}}}^{R} \hat{g}_{\mathrm{P}}(R')V'_{\mathrm{PP}}(R')\hat{F}_{\mathrm{P}}(R')\mathrm{d}R' \\ &+ \hat{g}_{\mathrm{P}}(R)\int_{R_{\mathrm{e}}}^{R} \hat{f}_{\mathrm{P}}(R')V'_{\mathrm{PP}}(R')\hat{F}_{\mathrm{P}}(R')\mathrm{d}R'. \end{aligned} \tag{3.31}$$

We then invert the relationship between the set of reference wave functions $\hat{f}(R)$ and $\hat{g}(R)$ and the set of reference wave functions $f(R)$ and $g(R)$ in equation (2.15), and we rewrite equation (3.31)

in terms of $f(R)$ and $g(R)$. This produces the following equation for $\hat{F}_{\rm P}(R)$ in the region $R \geq R_{\rm e}$,

$$\begin{aligned}\hat{F}_{\rm P}(R) =& f_{\rm P}(R)\mathcal{A}^{-1/2}\left(\mathcal{I}+\mathcal{G}\tilde{K}'\right) - g_{\rm P}(R)\mathcal{A}^{1/2}\tilde{K}' - f_{\rm P}(R)\int_{R_{\rm e}}^{R} g_{\rm P}(R')V'_{\rm PP}(R')\hat{F}_{\rm P}(R'){\rm d}R' \\ &+ g_{\rm P}(R)\int_{R_{\rm e}}^{R} f_{\rm P}(R')V'_{\rm PP}(R')\hat{F}_{\rm P}(R'){\rm d}R', \end{aligned} \tag{3.32}$$

where we find the relationship $\hat{f}(R)\hat{g}(R') - \hat{g}(R)\hat{f}(R') = f(R)g(R') - g(R)f(R')$ to be useful.

Equation (3.32) expresses $\hat{F}_{\rm P}(R)$ in terms of the reference wave functions $f(R)$ and $g(R)$ and their radially dependent coefficients. This equation is exactly analogous to equation (3.5), which expresses $M(R)$ in terms of the reference wave functions $\hat{f}(R)$ and $\hat{g}(R)$ and their radially dependent coefficients. Hence, by following the same steps as in equations (3.5 - 3.11), we derive the following integral equation for $Z(R)$ in the region $R \geq R_{\rm e}$,

$$Z(R) = Z(R_{\rm e}) - \int_{R_{\rm e}}^{R} \left(f_{\rm P}(R') - Z(R')g_{\rm P}(R')\right) V'_{\rm PP}(R') \left(f_{\rm P}(R') - g_{\rm P}(R')Z(R')\right) {\rm d}R'. \tag{3.33}$$

Following a now familiar pattern, we perform a distorted wave approximation by simply replacing $Z(R)$ inside the integral on the right hand side of this equation by $Z(R_{\rm e})$,

$$Z(R) \approx Z(R_{\rm e}) - \int_{R_{\rm e}}^{R} \left(f_{\rm P}(R') - Z(R_{\rm e})g_{\rm P}(R')\right) V'_{\rm PP}(R') \left(f_{\rm P}(R') - g_{\rm P}(R')Z(R_{\rm e})\right) {\rm d}R'. \tag{3.34}$$

Note that, because the open-channel wave functions are oscillatory at long range, this integral converges as $R \to \infty$ for any potential that vanishes faster than $1/R$.

We determine the boundary conditions on $Z(R)$ at $R_{\rm e}$ by performing the transformation $F(R) = \hat{F}(R)\mathcal{N}'$ at $R_{\rm e}$. In order to solve for $Z(R_{\rm e})$, we use equation (3.32) to write the behavior of $\hat{F}_{\rm P}(R)$ at $R_{\rm e}$ in terms of $f(R)$ and $g(R)$,

$$\hat{F}_{\rm P}(R) = f_{\rm P}(R)\mathcal{A}^{-1/2}\left(\mathcal{I}+\mathcal{G}\tilde{K}'\right) - g_{\rm P}(R)\mathcal{A}^{1/2}\tilde{K}'. \tag{3.35}$$

Substituting this expression for $\hat{F}_{\rm P}(R)$ and the expression for $F_{\rm P}(R)$ in equation (3.30) into the open channels of the transformation $F(R) = \hat{F}(R)\mathcal{N}'$, we equate the coefficients in front of $f(R)$ and $g(R)$ on both sides of this equation and derive the following expressions for $\mathcal{N}'$ and $Z(R_{\rm e})$,

$$\mathcal{N}' \approx \left(\mathcal{I}+\mathcal{G}\tilde{K}'\right)^{-1}\mathcal{A}^{1/2} \tag{3.36a}$$

$$Z(R_{\rm e}) \approx \mathcal{A}^{1/2}\tilde{K}'\left(\mathcal{I}+\mathcal{G}\tilde{K}'\right)^{-1}\mathcal{A}^{1/2}. \tag{3.36b}$$

These constants have the same form as $\mathcal{N}$ and K in the set of equations (2.27), except that $\tilde{K}$ is replaced by $\tilde{K}'$.

Because $Z(R_\mathrm{e})$ depends on $\tilde{K}'$, which explicitly depends on the denominator $K^{\mathrm{sr}'}_{\mathrm{QQ}} + \cot\gamma$ in equation (3.25), $Z(R_\mathrm{e})$ has poles as a function of energy or field at the locations of scattering resonances. The change in $K^{\mathrm{sr}'}$ inside this denominator is responsible for shifting the position of resonances; therefore, $Z(R_\mathrm{e})$ depends strongly on $V'(R)$ in the region $R \leq R_\mathrm{e}$. These resonances are essential to produce accurate scattering observables, but there is one term in equation (3.34) that has two factors of $Z(R_\mathrm{e})$, leading to large and unphysical corrections to K' near resonances.

To eliminate the second order effects of $V'(R)$ in the region $R \leq R_\mathrm{e}$, we approximate the evolution of $Z(R)$ beyond R_e by simply neglecting the term in equation (3.34) that is second-order in $Z(R_\mathrm{e})$. Making this approximation, we propagate $Z(R)$ to the limit $R \to \infty$. The asymptotic limit of $Z(R)$ defines the perturbed energy-normalized K-matrix K',

$$\begin{aligned} K' \approx & Z(R_\mathrm{e}) - \int_{R_\mathrm{e}}^{\infty} f_\mathrm{P}(R') V'_{\mathrm{PP}}(R') f_\mathrm{P}(R') \mathrm{d}R' + \int_{R_\mathrm{e}}^{\infty} f_\mathrm{P}(R') V'_{\mathrm{PP}}(R') g_\mathrm{P}(R') \mathrm{d}R' Z(R_\mathrm{e}) \\ & + Z(R_\mathrm{e}) \int_{R_\mathrm{e}}^{\infty} g_\mathrm{P}(R') V'_{\mathrm{PP}}(R') f_\mathrm{P}(R') \mathrm{d}R', \end{aligned} \tag{3.37}$$

where we bring the constant $Z(R_\mathrm{e})$ outside of the integrals over R'. All of the integrals in equation (3.37) involve energy-normalized open-channel wave functions that smoothly vary with energy and applied fields.

Finally, we obtain the perturbed physical scattering matrix $S^{\mathrm{phys}'}$ by using the MQDT algebra of equation (2.29) with K replaced by K',

$$S^{\mathrm{phys}'} = e^{i\eta} \frac{\mathcal{I} + iK'}{\mathcal{I} - iK'} e^{i\eta}. \tag{3.38}$$

We have designed this equation to maximally incorporate the effect of the full potential $V'(R)$ beyond R_m within first-order perturbation theory. Simultaneously, we have expressed this equation in terms of quantities that weakly depend on energy and field. Equation (3.38) for S^{phys}, equation (3.37) for K', equation (3.36b) for $Z(R_\mathrm{e})$, and equation (3.25) for $\tilde{K}'$ show that $S^{\mathrm{phys}'}$ entirely depends on $K^{\mathrm{sr}'}$, the QDT parameters, and the integrals in equation (3.37).

In our implementation of this perturbation theory, we compute and interpolate $K^{\mathrm{sr}'}$ of equation (3.28). We do not interpolate K'. Rather, we interpolate the set of integrals in equation (3.37). For clarity, we rewrite the quantities that we interpolate below. Here, we rewrite equation (3.28),

$$K^{\mathrm{sr}'} = K^{\mathrm{sr}} - \int_{R_{\mathrm{m}}}^{R_{\mathrm{t}_1}} M^{(0)T}(R')V'(R')M^{(0)}(R')\mathrm{d}R' - \int_{R_{\mathrm{t}_1}}^{R_{\mathrm{e}}} \tilde{M}^{(0)T}(R')V'(R')\tilde{M}^{(0)}(R')\mathrm{d}R'. \quad (3.39)$$

In equation (3.37), the matrix $\int_{R_{\mathrm{m}}}^{\infty} g_{\mathrm{P}}(R')V'_{PP}(R')f_{\mathrm{P}}(R')\mathrm{d}R'$ is simply the transpose of the matrix $\int_{R_{\mathrm{m}}}^{\infty} f_{\mathrm{P}}(R')V'_{PP}(R')g_{\mathrm{P}}(R')\mathrm{d}R'$. Therefore, we only numerically integrate the small set of integrals $\int_{R_{\mathrm{m}}}^{\infty} f_i(R')V'_{ij}(R')f_j(R')\mathrm{d}R'$ and $\int_{R_{\mathrm{m}}}^{\infty} f_i(R')V'_{ij}(R')g_j(R')\mathrm{d}R'$, where i and j only run over the set of open channels. We compute and interpolate these integrals and $K^{\mathrm{sr}'}$ on a coarse grid in energy and field.

We then use the interpolated values of these open-channel integrals, $K^{\mathrm{sr}'}$, and the QDT parameters to compute $S^{\mathrm{phys}'}$ according to the set of equations (3.25), (3.36b), (3.37), and (3.38) by means of simple algebra. For clarity, we rewrite this set of equations below,

$$\tilde{K}' \approx K^{\mathrm{sr}'}_{\mathrm{PP}} - K^{\mathrm{sr}'}_{\mathrm{PQ}}(K^{\mathrm{sr}'}_{\mathrm{QQ}} + \cot\gamma)^{-1}K^{\mathrm{sr}'}_{\mathrm{QP}} \quad (3.40a)$$

$$Z(R_{\mathrm{e}}) \approx \mathcal{A}^{1/2}\tilde{K}'\left(\mathcal{I} + \mathcal{G}\tilde{K}'\right)^{-1}\mathcal{A}^{1/2} \quad (3.40b)$$

$$\begin{aligned} K' \approx & Z(R_{\mathrm{e}}) - \int_{R_{\mathrm{e}}}^{\infty} f_{\mathrm{P}}(R')V'_{\mathrm{PP}}(R')\Big(f_{\mathrm{P}}(R') - g_{\mathrm{P}}(R')Z(R_{\mathrm{e}})\Big)\mathrm{d}R' \\ & + Z(R_{\mathrm{e}})\int_{R_{\mathrm{e}}}^{\infty} g_{\mathrm{P}}(R')V'_{\mathrm{PP}}(R')f_{\mathrm{P}}(R')\mathrm{d}R' \end{aligned} \quad (3.40c)$$

$$S^{\mathrm{phys}'} = e^{i\eta}\frac{\mathcal{I} + iK'}{\mathcal{I} - iK'}e^{i\eta}. \quad (3.40d)$$

3.4 Summary

We have extended MQDT to perturbatively incorporate long-range anisotropic interactions. Using the Green's function method, we derived a differential equation for a radially dependent K-matrix, denoted $\mathcal{K}(R)$, that fully described the interchannel coupling over the entire range of R.

When the perturbation involved closed channels, we found that the solution to this differential equation exponentially diverged in the region $R_{t_1} \leq R \leq R_e$. Using the distorted wave approximation, we found an approximation for $\mathcal{K}(R)$ that asymptotically converged. We constructed this approximation in terms of quantities that were weakly dependent on energy and field, allowing for an efficient calculation of all scattering observables. In chapter 4, we demonstrate that this extension of MQDT is necessary to retain sub-G accuracy in the position of Fano-Feshbach resonances in the scattering of potassium atoms with artificially enhanced magnetic dipole moments.

Chapter 4

Atomic Scattering

This chapter contains material in references [54] and [72].

4.1 Introduction

Ultracold atomic scattering often depends on many partial waves, rapidly increasing the number of scattering channels ($N >> 1$) required to compute accurate scattering observables. In alkali atoms, strong anisotropic interactions at short range couple many different partial waves together, and high-partial-wave (high-L) resonances can greatly influence s-wave scattering. In strongly magnetic atoms, these anisotropic couplings persist to long range, and scattering observables strongly depend on many partial waves. The full close-coupling (FCC) method, described in chapter 2, produces numerically exact solutions to the coupled Schrödinger equations (2.2), but this method tends to be quite slow. For example, even the relatively simple scattering of K and Rb atoms, restricted to channels with $L = 0$ and $L = 2$, requires $N \approx 100$ coupled hyperfine channels. The computational time of the FCC method is proportional to N^3 [57], and using it to characterize resonant scattering observables requires long FCC calculations at every energy and field of interest. This method is especially slow at describing high-L Fano-Feshbach resonances (FRs) because their widths decrease quickly with increasing L.

In this chapter, we perform the challenging (yet numerically feasible) FCC calculations of scattering observables, allowing us to test our formulation of MQDT. This method propagates the log-derivative matrix $Y(R)$ to very long range, where it approaches a constant. After this propa-

gation, the asymptotic limit of $Y(R)$ determines all scattering observables. The FCC calculation is known to be quite accurate, and it is our standard with which to compare the accuracy of MQDT. We demonstrate that the zeroth-order MQDT calculation of chapter 2 accurately reproduces the FCC results for alkali-atom scattering, including high partial waves. We show that the elements of K^{sr} are weakly dependent on magnetic field, and we perform the MQDT calculation by interpolating K^{sr} on a coarse grid in magnetic field, greatly increasing the numerical efficiency of calculating FRs. Using this enhanced efficiency, we quickly predict and characterize many FRs in ultracold ^{40}K + ^{85}Rb and ^{133}Li + ^{6}Cs collisions.

We also use the perturbative MQDT calculation of chapter 3 to incorporate the effects of a long-range dipole-dipole interaction within MQDT. As an example, we use the ultracold scattering of ^{40}K with an artificially enhanced dipole-dipole interaction. We deliberately increase the magnitude of this interaction so that the zeroth-order MQDT calculation is no longer accurate. By comparing with the FCC calculation, we show that the perturbative MQDT calculation can adequately characterize the effects that the enhanced dipole-dipole interaction has on the position and shape of a particular FR. This calculation is performed by interpolating the field-smooth matrix $K^{\mathrm{sr}'}$ over a coarse grid in magnetic field, retaining the numerical efficiency of MQDT.

4.2 Alkali Atoms

The simplicity of alkali-atom scattering allows for the construction of accurate scattering models. Because each atom has a single valence electron, we describe the short-range interaction between these atoms in terms of singlet and triplet Born-Oppenheimer potentials. Additionally, the long-range potential between these atoms is approximately isotropic, and we can accurately describe this potential in terms of isotropic dispersion coefficients. However, the exact form of the short-range potentials is not precisely known a priori, and the positions of FRs are sensitive to the precise scattering lengths of these potentials. The extensive experimental evidence of resonant scattering features in these gases at ultracold temperatures helps to pin down the scattering lengths. Because of these measurements, we can fine-tune our scattering model to accurately describe scattering

between alkali atoms near threshold.

In this section, we consider the collision of ^{40}K + ^{87}Rb in the lowest hyperfine states of each atom $|f_{\rm K} = 9/2, m_{f_{\rm K}} = -9/2\rangle$ and $|f_{\rm Rb} = 1, m_{f_{\rm Rb}} = 1\rangle$, where a number of FRs have been observed [73, 74]. The quantum number f is the total electronic plus nuclear spin, and m_f is its projection onto the polarization axis of the magnetic field. Our scattering model adopts the accurate, short-range molecular potentials $X\ ^1\Sigma^+$ and $a\ ^3\Sigma^+$ of reference [59] that were constructed by performing a global fit to the position of several $L = 0$ FRs. For consistency, our model also adopts the interaction parameters of reference [59] that describe the long-range forces. We describe this long-range model below. The van der Waals parameters C_6, C_8, and C_{10} describe the long-range dispersion forces. The electron-exchange interaction is,

$$E_{\rm ex}(R) = A_{\rm ex} R^{\gamma_{\rm ex}} e^{-\beta_{\rm ex} R}, \tag{4.1}$$

which is added to the triplet molecular state and subtracted from the singlet molecular state. The magnetic dipole-dipole interaction is,

$$V_{\rm dd}(R) = -\frac{\alpha^2}{2}\left(3S_z^2 - S^2\right)\left(1/R^3 + a_{\rm SO} e^{-b_{\rm SO}(R-R_{\rm SO})}\right), \tag{4.2}$$

where α is the fine structure constant. Reference [59] reports the values of the long-range interaction parameters C_6, C_8, C_{10}, $A_{\rm ex}$, $\beta_{\rm ex}$, $\gamma_{\rm ex}$, $a_{\rm SO}$, $b_{\rm SO}$, and $R_{\rm SO}$.

This model allows us to calculate accurate scattering observables and predict unobserved scattering features. We use this same model potential for both the FCC calculation and the MQDT calculation, allowing us to directly compare the FCC and MQDT methods. The FCC calculation considers the full Hamiltonian into the asymptotic region. The MQDT method only uses this full Hamiltonian up to the matching radius $R_{\rm m}$. Beyond $R_{\rm m}$, the MQDT reference wave functions are single-channel solutions in $V^{\rm lr}(R)$. We make the following choice for $V^{\rm lr}(R)$,

$$V^{\rm lr}(R) = -C_6/R^6 - C_8/R^8 - C_{10}/R^{10}. \tag{4.3}$$

This choice neglects $E_{\rm ex}(R)$ and $V_{\rm dd}(R)$ beyond $R_{\rm m}$. As a consequence, each channel only differs by a constant energy set by its hyperfine quantum numbers and subsequent Zeeman shift.

Despite neglecting these long-range forces, MQDT remains accurate. The electron-exchange energy $E_{\mathrm{ex}}(R)$ is vanishingly small beyond $R \approx 30\ a_0$, and we can choose R_{m} beyond this location. The dipole-dipole interaction $V_{\mathrm{dd}}(R)$ is very long range and creates a coupling between channels, leading to a difference between the MQDT and FCC calculations. However, we find that R_{m} can be increased until $V_{\mathrm{dd}}(R)$ makes a negligible contribution to the elastic cross section. We choose $R_{\mathrm{m}} = 45\ a_0$. This allows for excellent agreement between the two calculations. In applications where weak longer-range couplings must be included, we can use the perturbative MQDT of chapter 3 to include them.

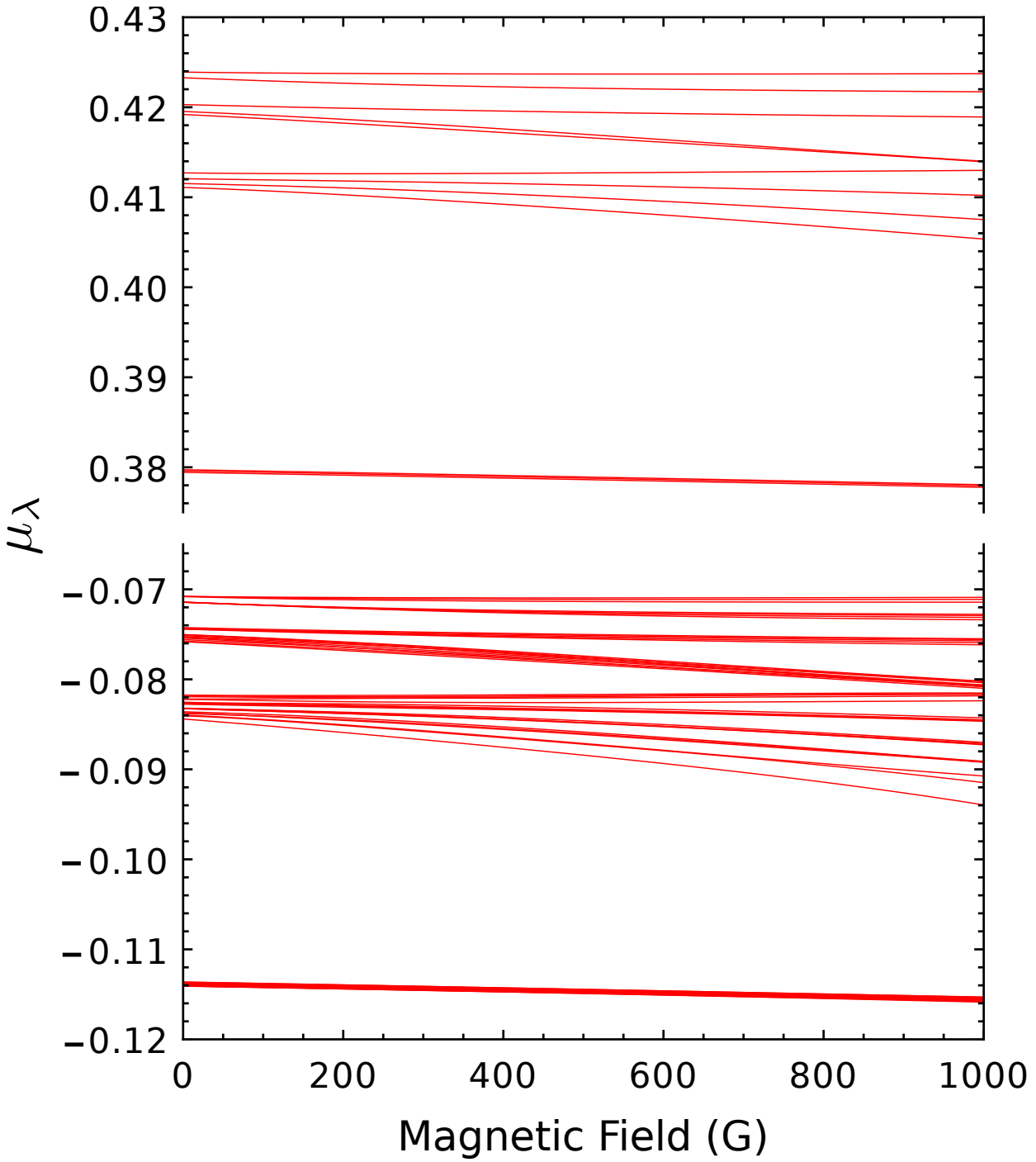

Figure 4.1: The quantum defects $\mu_\lambda = \tan\delta_\lambda/\pi$ are shown for the collision of ^{40}K + ^{87}Rb over the range $B = 0 - 1000$ G with a collision energy of 1 μK. For this calculation we match $Y(R)$ to solutions in the long-range potential $V^{\rm lr} = -C_6/R^6 - C_8/R^8 - C_{10}/R^{10}$ at $R_{\rm m} = 45\ a_0$, including channels with $L = 0$ and $L = 2$. The two graphs merely display two different ranges of μ over the same range of B.

If one chooses a matching radius R_{m} in the range $R_{\mathrm{m}} \approx 35 - 50\ a_0$ for alkali atoms, the QDT parameters approximately describe all physics beyond R_{m}. Simultaneously, all channels are locally open (or weakly closed) at R_{m}, and K^{sr} is typically a weak function of energy and field. Our choice of $R_{\mathrm{m}} = 45\ a_0$ leads to a smooth K^{sr} that is easy to interpolate over a large range of collision energy and magnetic field. The eigenvalues of K^{sr}, labeled by λ, have the functional form $\tan \delta_\lambda$, where δ_λ is the short-range eigenphase shift. We define the quantum defects to be $\mu_\lambda = \tan \delta_\lambda / \pi$. Figure 4.1 shows these quantum defects as a function of magnetic field over the range $B = 0 - 1000$ G.

With this same choice of $R_{\mathrm{m}} = 45\ a_0$, a coarse magnetic field grid of spacing 100 G allows for an accurate interpolation of K^{sr}, and MQDT accurately reproduces the six experimentally measured FRs in $L = 0 - 2$ states that were reported in reference [73]. Motivated by this accuracy and the excellent agreement with the FCC calculation, we use MQDT to quickly re-fit the singlet and triplet scattering lengths, producing our own accurate scattering model. Our fit includes the six experimentally measured resonance positions reported in reference [73] and the $L = 2$ resonance at 547.4(1) G, which was reported in reference [74] and recently confirmed by reference [75]. We list the measurements that we include in this fit and their uncertainties in table 4.1 of the next section. While retaining the value of $C_6 = 4.300 \times 10^3$ in atomic units, varying the scattering lengths leads to a minimum reduced chi-squared between the experimental resonance positions and the MQDT resonance positions. We vary these scattering lengths by slightly modifying the back wall of the singlet and triplet potentials. We find the optimal scattering lengths to be $a_{\mathrm{s}} = -110.8\ a_0$ and $a_{\mathrm{t}} = -214.5\ a_0$ with $\chi^2_{\mathrm{red}} = 0.83$.

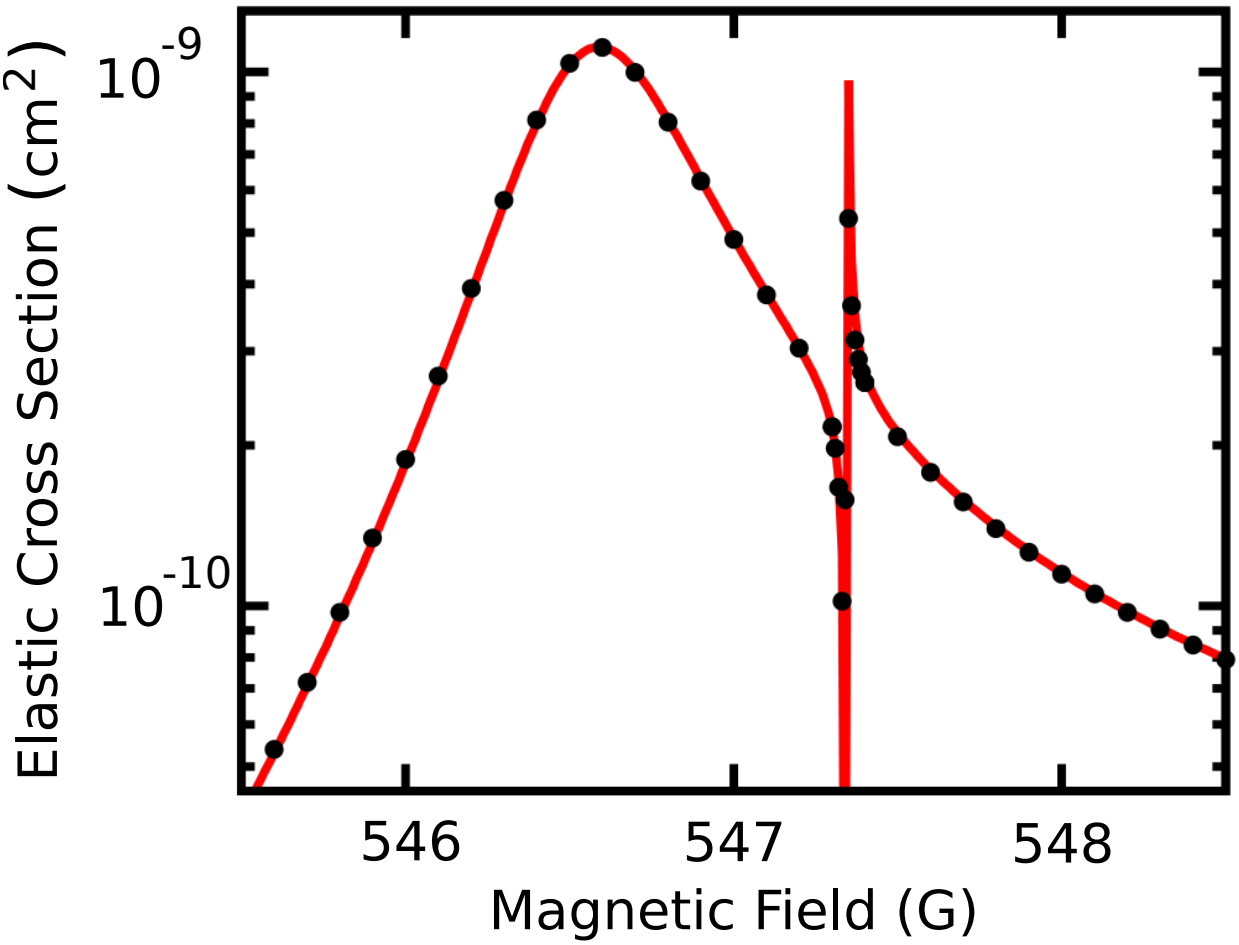

Figure 4.2: The elastic cross section for the collision of ^{40}K + ^{87}Rb with a collision energy of 1 μK is shown for the FCC calculation (black dots), including channels with $L = 0$ and $L = 2$. The FCC calculation is compared to the MQDT calculation (red curve) with $K^{\rm sr}$ interpolated over a range of 1000 G. This curve is unchanged if we use the analytic formulas (2.44) instead of the numerical values for A, η, and $\mathcal{G}$.

Using the re-tuned Hamiltonian, we perform the MQDT calculation of $L = 0 - 2$ FRs for ultracold $^{40}\mathrm{K} + {}^{87}\mathrm{Rb}$ collisions in their lowest hyperfine states. We demonstrate the accuracy of the MQDT calculation by comparing it to the FCC calculation. For example, figure 4.2 demonstrates the excellent agreement between the MQDT calculation and the FCC calculation of the elastic cross section near a pair of overlapping resonances. The wider resonance is of s-wave character, and the more narrow resonance is of d-wave character. By calculating K^{sr} on a magnetic field grid with a field spacing of 100 G and by interpolating the elements of K^{sr} over the range $B = 0 - 1000$ G, MQDT reproduces the FCC calculation with a small difference of $\lesssim 1$ mG in the resonance positions. The next section discusses the ability of MQDT to reproduce experimentally measured FR positions and predict unobserved FRs.

4.3 Fano-Feshbach Resonances

The accuracy and efficiency of MQDT allow for an extensive study of Fano-Feshbach resonances (FRs) in ultracold alkali-atom scattering. Because K^{sr} and the QDT parameters weakly depend on magnetic field, we can easily search for the location of FRs and characterize their shape. From equation (2.25b), we see that the roots of $\det\left(K^{\mathrm{sr}}_{\mathrm{QQ}} + \cot\gamma\right)$ determine quantitatively accurate resonance positions [34], where both K^{sr} and γ are interpolated with ease. After interpolating these quantities, the discovery of FRs only requires a magnetic field spacing that is finer than the distance between any two resonances [76]. This method allows enough numerical efficiency to ensure the discovery of *all* the FRs in a large range of magnetic field.

Table 4.1: This table describes all of the Fano-Feshbach resonances in the range $B = 0 - 1000$ G for the collision of ^{40}K + ^{87}Rb in the state $|f_{\mathrm{K}} = 9/2, m_{f_{\mathrm{K}}} = -9/2\rangle\,|f_{\mathrm{Rb}} = 1, m_{f_{\mathrm{Rb}}} = 1\rangle$ for a collision energy of 1 μK. This table lists the MQDT calculation of resonance positions B_0 and field widths Δ with their associated partial-wave quantum number L. All magnetic field values are in units of G. This table also lists the experimentally measured resonance positions B_{ex}.

B_{ex}	B_0	$-\Delta$	L	B_{ex}	B_0	$-\Delta$	L
-	96.06	1.5×10^{-16}	2	-	506.3	4.5×10^{-6}	2
-	108.7	2.3×10^{-13}	2	515.7(5)	515.1	0.50	1
-	124.3	3.1×10^{-9}	2	-	526.5	5.7×10^{-5}	1
-	143.9	2.6×10^{-8}	2	-	531.8	3.1×10^{-5}	1
-	155.9	1.9×10^{-12}	1	-	540.8	1.9×10^{-6}	1
-	168.1	2.7×10^{-7}	2	546.6(2)	546.6	3.1	0
-	171.9	1.1×10^{-11}	2	547.4(1)	547.3	6.3×10^{-3}	2
-	178.2	3.7×10^{-6}	1	-	558.5	9.6×10^{-8}	2
-	205.1	2.5×10^{-9}	1	-	568.9	4.0×10^{-6}	2
-	206.8	1.5×10^{-5}	0	-	590.1	1.9×10^{-6}	2
-	215.8	3.9×10^{-9}	2	-	592.9	3.1×10^{-7}	2
-	277.6	4.3×10^{-6}	2	-	621.8	0.13	1
-	320.3	5.3×10^{-10}	1	-	629.6	2.0×10^{-5}	1
-	356.8	9.5×10^{-5}	2	-	644.0	7.1×10^{-9}	1
-	393.3	5.1×10^{-5}	2	658.9(6)	658.9	0.80	0
-	403.2	1.2×10^{-8}	2	663.7(2)	663.8	5.5×10^{-3}	2
-	404.5	0.024	1	-	690.8	1.8×10^{-6}	2
-	412.2	2.2×10^{-4}	2	-	720.8	6.8×10^{-11}	2
-	421.9	3.6×10^{-12}	2	-	752.5	2.0×10^{-6}	1
-	429.4	2.4×10^{-8}	1	-	754.0	2.5×10^{-14}	2
-	444.0	1.8×10^{-9}	2	-	779.4	2.1×10^{-5}	1
-	455.8	3.9×10^{-5}	2	-	809.7	4.6×10^{-12}	1
456.1(2)	456.3	5.6×10^{-3}	1	-	823.2	1.9×10^{-4}	0
-	462.0	0.062	0	-	892.8	6.3×10^{-10}	2
-	466.3	2.5×10^{-5}	2	-	934.3	6.6×10^{-9}	2
-	473.1	6.7×10^{-9}	1	-	979.9	4.9×10^{-11}	2
-	479.9	2.3×10^{-5}	2				
-	483.5	3.9×10^{-8}	2				
495.6(5)	495.3	0.15	0				

4.3.1 K + Rb

In section 4.2, we described the scattering between ^{40}K + ^{87}Rb in their lowest hyperfine states $|f_{\rm K} = 9/2, m_{f_{\rm K}} = -9/2\rangle$ and $|f_{\rm Rb} = 1, m_{f_{\rm Rb}} = 1\rangle$, and we re-tuned the scattering model to achieve an optimum accuracy. Here, even though some resonances can be extremely narrow, we use MQDT to predict and describe *all* of the FRs between these states in the range $0 - 1000$ G. Table 4.1 lists these resonance positions and field widths.

As our model calculates all experimentally measured resonances close to their positions $B_{\rm ex}$, the unmeasured resonance positions of table 4.1 are predictive with uncertainties on the order of current experimental uncertainties ($\lesssim 1$ G). Once our theory predicts a resonance at the position B_0, we determine the width of an $L = 0$ or $L = 2$ resonance by fitting the divergence of the scattering length $a(B)$ near the resonance to the following form [73],

$$a(B) = a_{\rm bg}\left(1 - \frac{\Delta}{B - B_0}\right), \tag{4.4}$$

where $a_{\rm bg}$ is the constant local background scattering length and Δ is the field width. To describe resonances of $L = 1$ character, we fit the divergence of the scattering volume $a_1^3(B)$ near the resonance to the following form,

$$a_1^3(B) = a_{1,\rm bg}^3\left(1 - \frac{\Delta}{B - B_0}\right), \tag{4.5}$$

where $a_{1,\rm bg}^3$ is the constant local background scattering volume.

For high-L resonances beyond $L = 2$, the resonance widths in K + Rb collisions become orders of magnitude more narrow. For example, MQDT predicts the widest of the $L = 4$ resonances to have a field width $\lesssim 1$ μG. The time required to perform a FCC calculation of resonances this narrow makes the comparison between the MQDT calculation and the FCC calculation challenging. However, predicting the position and width of high-L resonances remains simple within MQDT. Despite only performing a detailed, fully-coupled calculation on a magnetic field grid of spacing 100 G, our method has found and characterized features 18 orders of magnitude smaller than this.

Table 4.2: This table reports the MQDT calculation of FRs in ^{6}Li + ^{133}Cs. For each resonance, this table lists the incident spin state $|f_{\mathrm{Li}}, m_{f_{\mathrm{Li}}}, f_{\mathrm{Cs}}, m_{f_{\mathrm{Cs}}}\rangle$; the resonant state quantum numbers $M_F = m_{f_{\mathrm{Li}}} + m_{f_{\mathrm{Cs}}}$, L, and M_L; the resonance location B_0; the field width Δ; the local background scattering length or scattering volume $a_{L,\mathrm{bg}}^{2L+1}(B_0)$ (in atomic units); and the inelastic field width Γ. The collision energy is 1 μK in each case. All magnetic field values are in units of G. This table also reports the experimentally measured resonance positions B_{ex}, reported in reference [77].

Incident state	M_F	L	M_L	B_{ex}	B_0	Δ	$a_{L,\mathrm{bg}}^{2L+1}(B_0)$	Γ
$\|1/2, 1/2, 3, 3\rangle$	5/2	1	1		634.2	-1.39×10^{-4}	-6.89×10^{4}	–
	7/2	1	0	662.79(1)	662.9	-9.55×10^{0}	-1.02×10^{5}	–
	7/2	1	1	663.04(1)	663.0	-9.56×10^{0}	-1.02×10^{5}	–
	5/2	1	1		682.3	-3.98×10^{-6}	-1.52×10^{5}	–
	9/2	1	-1		690.6	-2.50×10^{-5}	-1.36×10^{5}	–
	7/2	1	0	713.63(2)	713.7	-5.92×10^{-1}	-1.23×10^{5}	–
	7/2	1	1	714.07(1)	714.0	-5.90×10^{-1}	-1.23×10^{5}	–
	5/2	1	1		737.6	-2.04×10^{-9}	-1.20×10^{5}	–
	7/2	0	0	843.5(4)	843.1	-6.56×10^{1}	-2.64×10^{1}	–
	7/2	0	0	892.87(7)	892.9	-2.07×10^{0}	-6.40×10^{1}	–
$\|1/2, -1/2, 3, 3\rangle$	3/2	1	1		632.5	-2.01×10^{-6}	-9.01×10^{4}	–
	5/2	1	0	658.21(5)	658.2	-1.67×10^{-1}	-8.42×10^{4}	–
	3/2	1	1		676.0	-9.57×10^{-5}	-7.46×10^{4}	–
	7/2	1	-1		687.4	–	–	–
	5/2	1	0	708.63(1)	708.7	-9.32×10^{0}	-1.03×10^{5}	–
	5/2	1	1	708.88(1)	708.9	-9.33×10^{0}	-1.03×10^{5}	–
	3/2	1	1		728.8	-3.21×10^{-6}	-1.50×10^{5}	–
	7/2	1	-1		740.9	-1.54×10^{-5}	-1.31×10^{5}	4.40×10^{-1}
	5/2	1	0	764.23(1)	764.3	-5.69×10^{-1}	-1.21×10^{5}	–
	5/2	1	1	764.67(1)	764.6	-5.68×10^{-1}	-1.21×10^{5}	–
	5/2	0	0	816.24(2)	816.5	-2.37×10^{0}	-4.30×10^{0}	–
	5/2	0	0	889.2(2)	888.9	-6.37×10^{1}	-2.70×10^{1}	–
	5/2	0	0	943.26(3)	943.3	-2.03×10^{0}	-6.10×10^{1}	–
$\|1/2, 1/2, 3, 2\rangle$	5/2	1	1	704.49(3)	704.5	-1.79×10^{1}	-9.94×10^{4}	1.70×10^{-1}
	7/2	1	0		734.6	–	–	–
	5/2	1	1		760.4	-6.03×10^{-1}	-1.33×10^{5}	1.20×10^{1}
	9/2	1	-1		773.1	-1.65×10^{-6}	-1.32×10^{5}	–
	7/2	1	0		798.3	-1.89×10^{-6}	-1.22×10^{5}	8.67×10^{-1}
	5/2	1	1		824.7	-1.39×10^{-3}	-1.17×10^{5}	7.87×10^{-1}
	5/2	0	0	896.6(7)	896.2	-1.39×10^{2}	-2.07×10^{1}	7.23×10^{-1}
	5/2	0	0		939.6	-2.00×10^{0}	-9.08×10^{1}	2.10×10^{1}
	5/2	0	0		1019.1	-1.30×10^{-3}	-5.03×10^{1}	7.55×10^{-1}
$\|1/2, -1/2, 3, 2\rangle$	3/2	1	1		694.8	-3.90×10^{-1}	-6.86×10^{4}	–
	5/2	1	0		728.5	–	–	–
	3/2	1	1	750.06(6)	750.1	-1.75×10^{1}	-1.00×10^{5}	1.48×10^{-1}
	7/2	1	-1		761.5	–	–	–
	5/2	1	0		784.8	–	–	–
	3/2	1	1		811.2	-5.68×10^{-1}	-1.30×10^{5}	1.28×10^{1}
	7/2	1	-1		828.0	-2.27×10^{-6}	-1.28×10^{5}	8.42×10^{-1}
	5/2	1	0	853.85(1)	853.8	-1.33×10^{-6}	-1.20×10^{5}	8.37×10^{-1}
	3/2	0	0		854.3	1.43×10^{0}	9.74×10^{0}	–
	3/2	0	0	943.5(1.1)	941.6	-1.33×10^{2}	-2.17×10^{1}	6.01×10^{-1}
	3/2	0	0		989.9	-1.89×10^{0}	-8.42×10^{1}	2.12×10^{1}

4.3.2 Li + Cs

In this section, we further demonstrate the accuracy of MQDT and its predictive power by characterizing a large set of s-wave FRs and p-wave FRs for a few different incident states of ultracold ^{6}Li + ^{133}Cs scattering. We choose the set of incident states listed in table 4.2. For the MQDT calculation, we choose $R_{\rm m} = 40\ a_0$. This choice produces a $K^{\rm sr}$ that is smooth in energy and field. The smoothness of $K^{\rm sr}$ is similar to the case of K + Rb, for which the eigenvalues of $K^{\rm sr}$ were shown in figure 4.1.

We construct a scattering model using the long-range interactions described in section 4.2. Here, we use the long-range interaction parameters of reference [78]. We also use the accurate, short-range molecular potentials $X\ ^1\Sigma^+$ and $a\ ^3\Sigma^+$ of reference [78]. Similar to our treatment of ^{40}K + ^{87}Rb, we slightly modify the back wall of these singlet and triplet molecular potentials to optimally produce 19 of the experimentally measured FR positions reported in reference [77]. Table 4.2 reports these measured FR positions, along with the optimal MQDT prediction of these resonance positions and their corresponding quantum numbers.

Reference [72] reports a detailed comparison between the MQDT method and the FCC method, demonstrating their equivalent ability to describe these 19 experimentally measured FR positions. MQDT obtains the root-mean-square deviation of $\delta B^{\rm rms} = 0.040$ G between the measured FR positions and those positions calculated by theory. The FCC calculation obtains $\delta B^{\rm rms} = 0.039$ G. Reference [72] also fully develops and applies three other methods of determining these FR positions, obtaining $\delta B^{\rm rms} = 0.048$ G for the MQDT frame transformation method, $\delta B^{\rm rms} = 0.263$ G for the dressed asymptotic bound state method, and $\delta B^{\rm rms} = 0.965$ G for the bare asymptotic bound state method. Besides the FCC calculation, all of these calculations have a similar computational expense, and MQDT performs the best.

Utilizing the efficiency and accuracy of MQDT, we search for all FRs in the range of magnetic field $0 - 1500$ G for this same set of incident states. For brevity, we only describe p-wave FRs for a single value of incident M_L for each incident spin state, except when this doublet was experimentally

resolved. We also describe how the theory extracts resonance widths. Within MQDT, finding and identifying FRs is straightforward. Approximate FR locations are quickly determined by searching for roots of $\det(K^{\rm sr}_{QQ} + \cot\gamma)$, and the eigenstate of $K^{\rm sr}_{QQ} + \cot\gamma$ whose eigenvalue crosses zero near an FR identifies the quantum numbers of the resonant state. Table 4.2 reports FRs in the range of magnetic field $B = 0{-}1500$ G, labeled by their incident spin state $|f_{\rm Li}, m_{f_{\rm Li}}, f_{\rm Cs}, m_{f_{\rm Cs}}\rangle$ and resonant-state quantum numbers $M_F = m_{f_{\rm Li}} + m_{f_{\rm Cs}}$, L, and M_L. The quantum number M_L of each incident channel is easily inferred from table 4.2 by conservation of total angular momentum $M_F^{\rm inc} + M_L^{\rm inc} = M_F^{\rm res} + M_L^{\rm res}$.

To characterize each FR in terms of a resonance position B_0 and a field width Δ, we calculate one of two quantities: the real part of the scattering length a_0^1 or the real part of the scattering volume a_1^3. We refer to these two quantities simultaneously as a_L^{2L+1}. The quantities a_L^{2L+1} are approximately independent of energy at ultralow energy,

$$a_L^{2L+1} \xrightarrow{k\to 0} -\tan\delta_L / k^{2L+1}, \tag{4.6}$$

where the phase shift δ_L obeys the Wigner threshold laws $\delta_L \xrightarrow{k\to 0} \propto k^{2L+1}$. We numerically determine that the simple threshold behavior of δ_L leads to an energy-independent field width Δ for $L = 0$ and $L = 1$ resonances. We use MQDT to quickly generate a_L^{2L+1} on a fine grid in magnetic field at an incident collision energy of 1 μK, and we fit $a_L^{2L+1}(B)$ to one of three different functional forms described below.

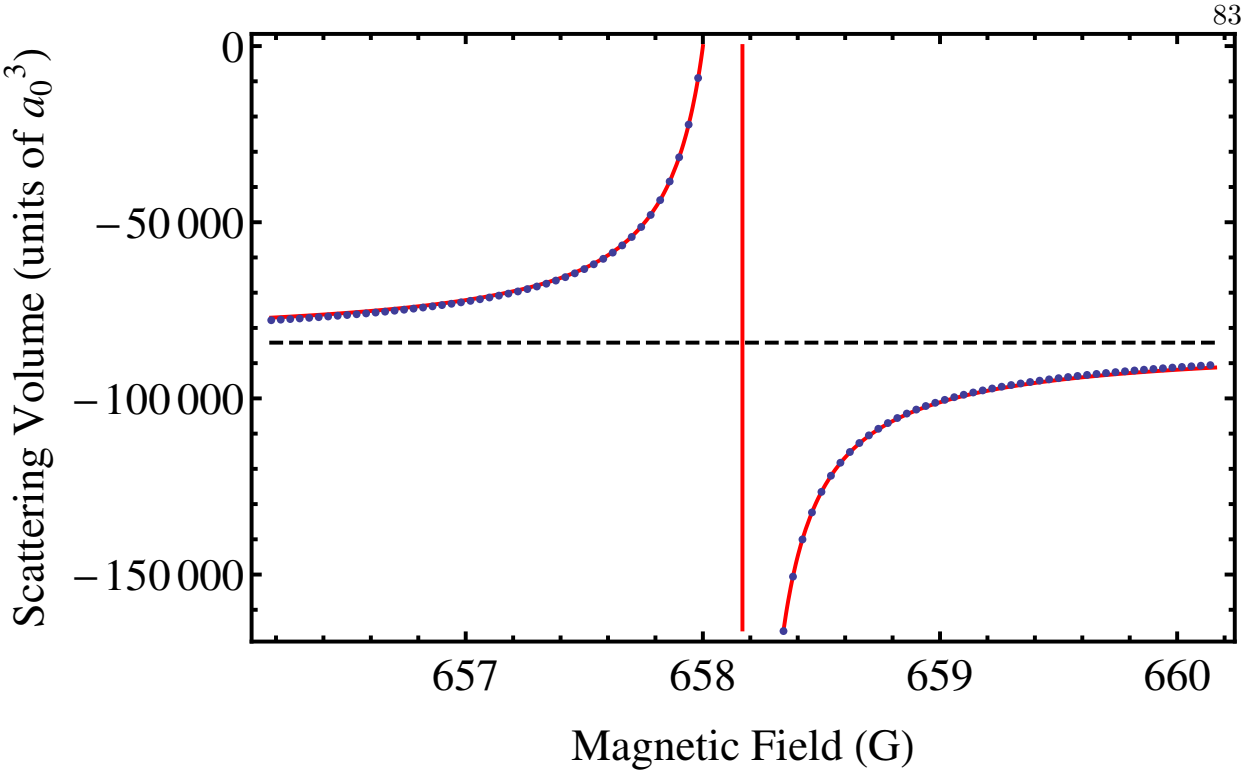

(a) $\Delta \approx -0.167$ G, and $a^3_{1,\mathrm{bg}}(B)$ is constant.

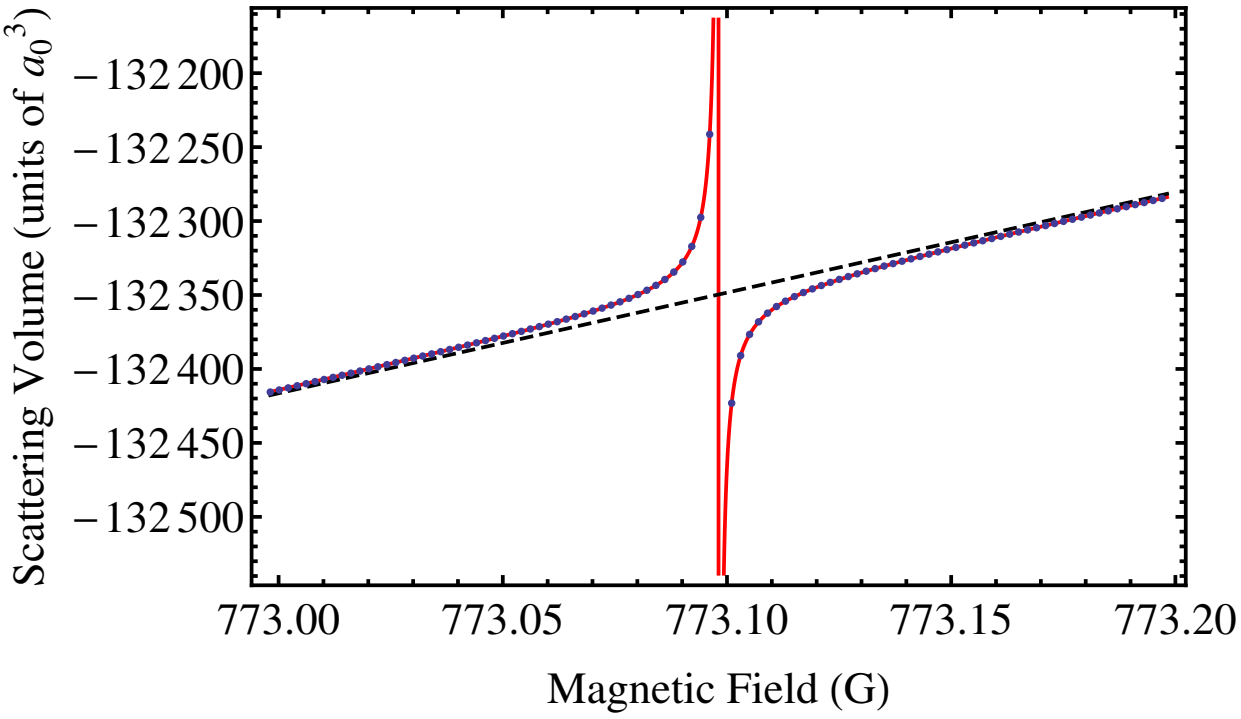

(b) $\Delta \approx -1.65$ μG, and $a^3_{1,\mathrm{bg}}(B)$ is linear.

Figure 4.3: These graphs show the $L = 1$ resonances near (a) 658.2 G and (b) 773.1 G. In each graph, the red curve is the best-fit form of equation (4.7); the blue dots represent the MQDT calculation of $a_1^3(B)$; and the black dashed line is the function $a^3_{1,\mathrm{bg}}(B)$.

Unlike the previous section, the incident states we explore in this section can lead to inelastic scattering. For the majority of FRs in table 4.2, the resonant state is much more strongly coupled to the incident scattering channel than to any inelastic (exoergic) channel, and a clear pole emerges in $a_L^{2L+1}(B)$. In this case, $a_L^{2L+1}(B)$ takes the conventional form,

$$a_L^{2L+1}(B) = a_{L,\mathrm{bg}}^{2L+1}(B)\left(1 - \frac{\Delta}{B - B_0}\right), \tag{4.7}$$

where Δ and B_0 are constants. The quantity Δ is the field width, and B_0 is the resonance location. When $|\Delta|$ is relatively large ($|\Delta| > 0.1$ G), we let $a_{L,\mathrm{bg}}^{2L+1}(B)$ be constant in B. This allows for an excellent fit of $a_L^{2L+1}(B)$. When $|\Delta|$ is relatively small ($|\Delta| < 0.1$ G), we let $a_{L,\mathrm{bg}}^{2L+1}(B)$ be linear in B to achieve an equivalent fit. Figures 4.3(a) and 4.3(b) demonstrate fits of resonances described by equation (4.7) when $|\Delta| > 0.1$ G and $|\Delta| < 0.1$ G, respectively.

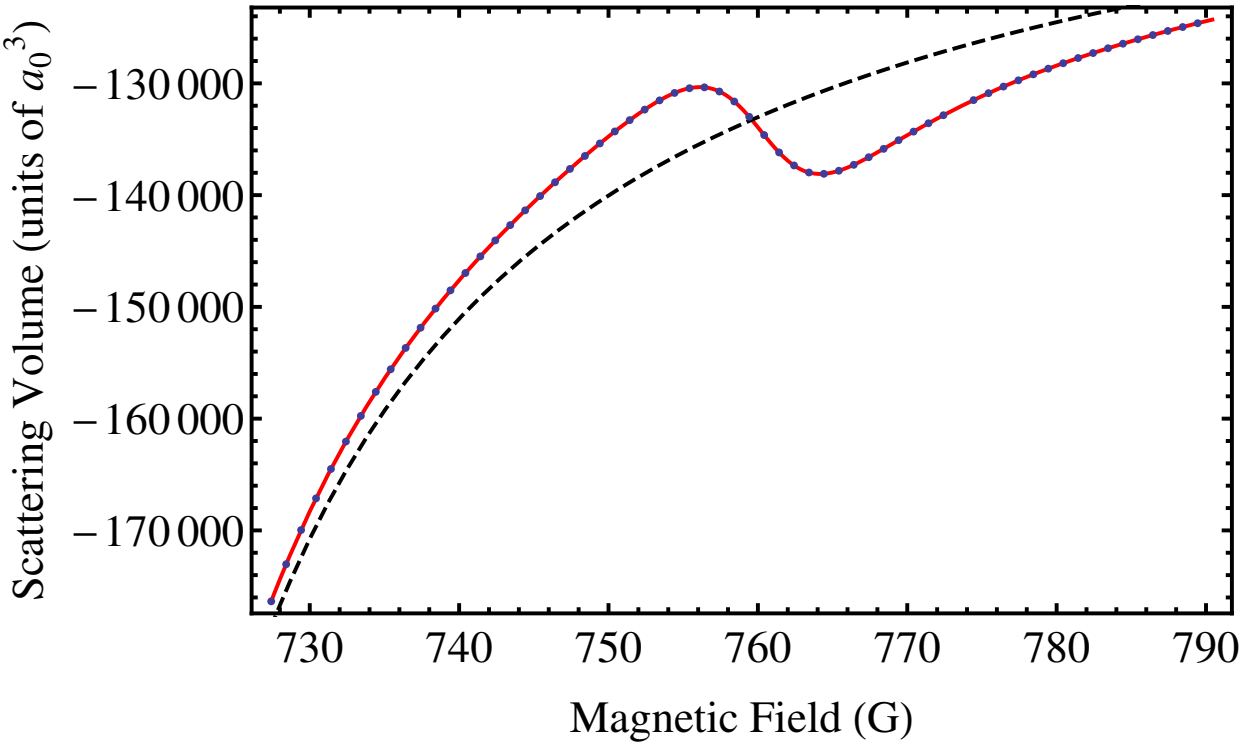

Figure 4.4: This graph shows the $L = 1$ resonance near 760.4 G. The red curve is the best-fit form of equation (4.8); the blue dots represent the MQDT calculation of $a_1^3(B)$; and the black dashed line is the high order polynomial $a_{1,\mathrm{bg}}^3(B)$. This fit excludes data around the narrow resonance near 773.1 G.

For several FRs in table 4.2, the resonant state is comparably coupled to both the incident channel and an inelastic channel, and the variation of $a_L^{2L+1}(B)$ becomes less drastic than for pure elastic scattering. In this case we fit $a_L^{2L+1}(B)$ to the following form [79],

$$a_L^{2L+1}(B) = a_{L,\mathrm{bg}}^{2L+1}(B) + \frac{\alpha\big(2(B-B_0)/\Gamma\big)+\beta}{\big(2(B-B_0)/\Gamma\big)^2+1}, \tag{4.8}$$

where α, β, Γ, and B_0 are constants. The quantity Γ is the inelastic field width. Since the variation in $a_L^{2L+1}(B)$ near these FRs can be small, we fit these FRs by letting $a_{L,\mathrm{bg}}^{2L+1}(B)$ be a high order (order=9) polynomial in B. This high-order fit is appropriate as the coefficients decrease by orders of magnitude with successive powers of B, and the best-fit $a_{L,\mathrm{bg}}^{2L+1}(B)$ is not oscillatory in the vicinity of B_0. For example, figure 4.4 shows the best-fit scattering volume $a_1^3(B)$ near the resonance at 760.4 G.

Table 4.2 summarizes the behavior of each FR in terms of the small set of parameters B_0, Δ, $a_{L,\mathrm{bg}}^{2L+1}(B_0)$, and Γ. We use the parameter Δ in order to directly compare all FRs, regardless of their character. As fitting the FRs to the form of equation (4.8) does not determine Δ, we suggest an approximate relation between Δ and Γ. By comparing equations (4.8) and (4.7) in the limit $(B-B_0)/\Gamma >> 1$, we obtain the following approximate relation,

$$\Delta \approx -\frac{\alpha\Gamma/2}{a_{L,\mathrm{bg}}^{2L+1}(B_0)}. \tag{4.9}$$

Listing a value for Γ in table 4.2 indicates that this approximation has been used to determine Δ.

Five of the resonances whose locations are identified by MQDT do not exhibit an appreciable variation in a_L^{2L+1} with B. For these FRs, table 4.2 gives the predicted resonance location from the root of $\det(K_{QQ}^{\mathrm{sr}} + \cot\gamma)$ but does not report a value of Δ. Our method has found FRs with a value of Δ as small as 10^{-9} G. Therefore, either the uncharacterized resonances are heavily suppressed by inelastic scattering, or they are extremely narrow.

4.4 Magnetic Atoms

For the study of alkali-atom scattering in section 4.2, it is in fact a good assumption to neglect the magnetic dipole-dipole interaction at long range. This holds because of the comparatively small

magnetic dipole moment ($\mu = 1\ \mu_{\mathrm{B}}$) of these atoms. In alternative cases, such as erbium ($\mu = 7\ \mu_{\mathrm{B}}$) or dysprosium ($\mu = 10\ \mu_{\mathrm{B}}$) this may no longer be the case, and the long-range dipolar interaction may significantly impact the scattering, particularly near a Fano-Feshbach resonance (FR). Additionally, dipolar molecules have strong anisotropic couplings at long range that are not negligible. To account for these effects, we use the perturbative MQDT method of chapter 3. In this section, we illustrate the efficiency and accuracy of the perturbative MQDT method by applying this method to the ultracold scattering of potassium atoms with an artificially enhanced magnetic dipole-dipole interaction.

To this end, we construct a simple model that accurately describes the ultracold scattering of potassium atoms, and we artificially increase the magnitude of the dipole-dipole interaction $V_{\mathrm{dd}}(R)$. For simplicity, we also neglect the second-order spin-orbit interaction in our model of potassium. In this case, equation (4.10) takes the following form,

$$V_{\mathrm{dd}}(R) = -\frac{\xi^2\alpha^2}{2}\left(3S_z^2 - S^2\right)/R^3, \tag{4.10}$$

where we include the artificial enhancement factor ξ^2. Note that this enhancement only changes the strength of $V_{\mathrm{dd}}(R)$ and does not affect the threshold energies. By increasing the value of ξ, we generate a magnetic dipole-dipole interaction with an artificially large strength. This strength is comparable to the strength of the magnetic dipole-dipole interaction between two atoms with the same magnetic dipole moment $\mu = \xi\ \mu_{\mathrm{B}}$. For realistic alkali-atom collisions, we simply set ξ equal to exactly one. We increase the value of ξ to simulate atomic scattering with dipole moments μ as large as $\mu = 10\ \mu_{\mathrm{B}}$ and beyond. The physical significance of ξ is most closely related to half of the electronic gyromagnetic ratio g_s in only this single term of the potential $V(R)$. Below, we demonstrate that the long-range dipole-dipole interaction can significantly shift FRs and that our MQDT perturbation theory does an adequate job of tracking this shift on resonance.

Our model of potassium uses the molecular potential $X\ ^1\Sigma^+$ g of reference [80] and the molecular potential $a\ ^3\Sigma^+$ u of reference [81] with corrections from references [82] and [83]. We use the long-range dispersion coefficient C_6 of reference [84] and the coefficients C_8 and C_{10} of

reference [85]. We include the partial waves $L = 0$ and $L = 2$. We adjust the singlet and triplet scattering lengths to fit the measurement of binding energy vs. magnetic field near the s-wave FR between the states $|f = 9/2, m_f = -7/2\rangle$ and $|f = 9/2, m_f = -9/2\rangle$, reported in reference [86]. The quantum number f is the total electronic plus nuclear spin, and m_f is its projection onto the polarization axis of magnetic field.

We find that increasing the magnitude of the dipole-dipole interaction significantly shifts the position of the s-wave FR between the states $|f = 9/2, m_f = -7/2\rangle$ and $|f = 9/2, m_f = -9/2\rangle$. We artificially increase $V_{\mathrm{dd}}(R)$ by letting $\xi = 10$, which corresponds to a magnetic dipole moment of dysprosium ($\mu = 10\ \mu_{\mathrm{B}}$), and we use the character of this resonance at 1 μK to compare three different computational methods: the full close-coupling (FCC) calculation, the zeroth-order MQDT calculation of chapter 2, and the perturbative MQDT calculation of chapter 3. These three calculations all use the same log-derivative propagation method in the region $R \leq R_{\mathrm{m}}$, producing the same value for K^{sr} in both the zeroth-order MQDT calculation and the perturbative MQDT calculation. Therefore, any difference between the results of these three methods is solely due to their ability to accurately account for the influence of the potential $V(R)$ beyond R_{m}.

4.4.1 Accuracy in the Near Zone

In the region $R_{\mathrm{m}} \leq R \leq R_{\mathrm{t}_1}$, all channels are locally open, and the perturbative MQDT calculation uses equation (3.13) to propagate $\mathcal{K}(R)$ beyond its boundary condition at R_{m},

$$\mathcal{K}(R) \approx K^{\mathrm{sr}} - \int_{R_{\mathrm{m}}}^{R} M^{(0)T}(R')V'(R')M^{(0)}(R')\mathrm{d}R', \tag{4.11}$$

where we determine K^{sr} by numerically propagating the log-derivative matrix $Y(R)$ from $R \approx 0$ to R_{m} and evaluating equation (2.12). Alternatively, since all channels are locally open in this region, we can instead simply continue to propagate the log-derivative matrix to a location R beyond R_{m} and determine a numerically exact version of $\mathcal{K}(R)$. We use the following equation to determine this numerically exact value of $\mathcal{K}(R)$,

$$\mathcal{K}(R) = \left(Y(R)\hat{g}(R) - \frac{\mathrm{d}\hat{g}(R)}{\mathrm{d}R}\right)^{-1}\left(Y(R)\hat{f}(R) - \frac{\mathrm{d}\hat{f}(R)}{\mathrm{d}R}\right). \tag{4.12}$$

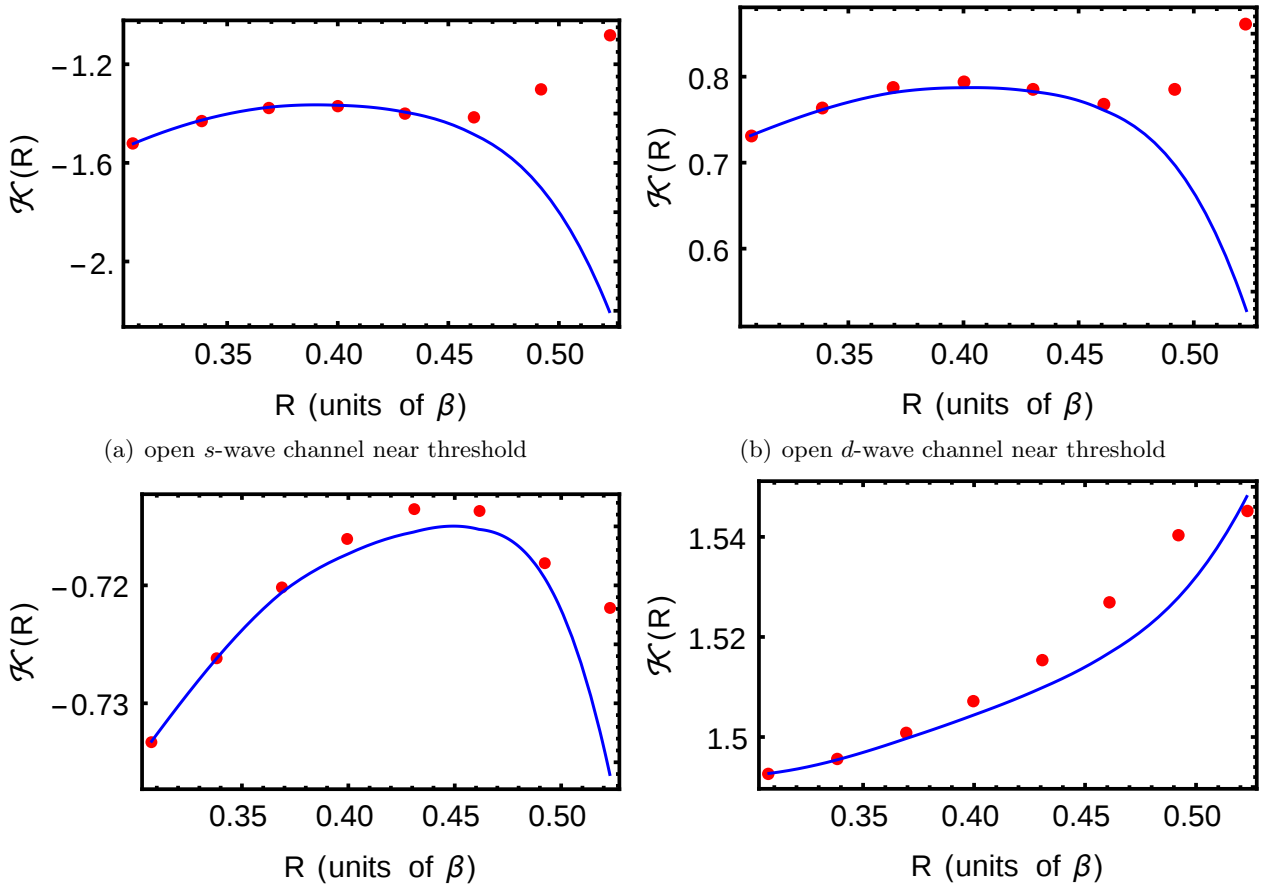

(a) open s-wave channel near threshold

(b) open d-wave channel near threshold

(c) closed s-wave channel

(d) closed d-wave channel

Figure 4.5: These graphs represent the calculation of $\mathcal{K}(R)$ with $\xi = 10$ using the exact log-derivative propagation (red dots) and the perturbative expression in equation (4.11) (blue line). These graphs show four representative diagonal elements of $\mathcal{K}(R)$ that correspond to (a) an open s-wave channel near threshold, (b) an open d-wave channel near threshold, (c) a closed s-wave channel, and (d) a closed d-wave channel. The other elements of $\mathcal{K}(R)$ all have a similar radial dependence that is not shown.

Figure 4.5 compares the perturbative calculation to the numerically exact calculation of $\mathcal{K}(R)$, where $R_{\mathrm{m}} = 30\ a_0$. This value corresponds to $R_{\mathrm{m}} \approx 0.31$ in units of the natural van der Waals length β. The agreement is excellent when $R \leq R_{\mathrm{t}_1} \approx 0.33$. Extending both of these methods beyond R_{t_1} demonstrates the numerical divergence of $\mathcal{K}(R)$. Not only do both of these methods show a divergence of $\mathcal{K}(R)$ beyond R_{t_1}, but also the two calculations quickly diverge from each other. We numerically determine that neither calculation of $\mathcal{K}(R)$ beyond R_{t_1} leads to accurate scattering observables. Although we choose $R_{\mathrm{m}} \approx R_{\mathrm{t}_1}$ in this example, we note that the accuracy of equation (4.11) in the region of locally open channels indicates that the alternative approximation to $K^{\mathrm{sr}'}$ in equation (3.29) may be useful when some closed channels are locally open well beyond R_{t_1}, which is not the case in this example problem.

4.4.2 Choosing the Elimination Radius

Beyond R_{t_1}, the issue of numerical convergence is simple for the FCC calculation and for the zeroth-order MQDT calculation. Beyond R_{m}, we entirely formulate these calculations in terms of quantities that we determine asymptotically. The FCC calculation simply continues to propagate the log-derivative matrix $Y(R)$ to the limit $R \to \infty$. In this limit, the $N_{\mathrm{o}} \times N_{\mathrm{o}}$ block of $Y(R)$ shows a clear convergence, and we use it to compute scattering observables. Likewise, the zeroth-order MQDT calculation only requires K^{sr} and the QDT parameters, which we also compute in the asymptotic limit, using the set of equations (2.17).

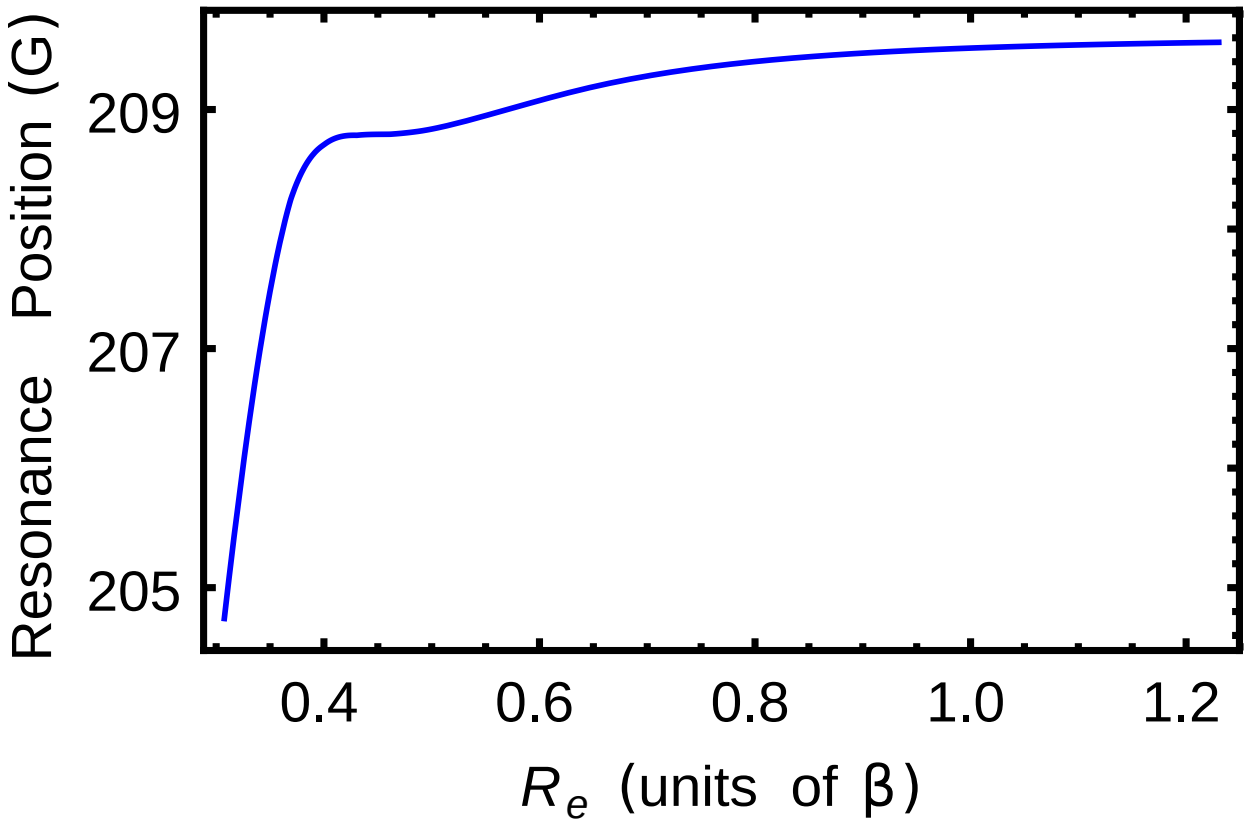

Figure 4.6: This figure shows the position B_0 of the s-wave FR between the states $|f = 9/2, m_f = -7/2\rangle$ and $|f = 9/2, m_f = -9/2\rangle$ of ^{40}K, as calculated by the perturbative MQDT method. This figure shows how the resonance position depends on the location $R_{\rm e}$ at which we eliminate the closed channels from the scattering problem. The graph covers the region $R_{\rm e} \geq R_{\rm t_1}$, where $R_{\rm t_1} \approx 0.33$ is the smallest outer classical turning point of any asymptotically closed channel. We choose $R_{\rm m} \approx 0.31$, and we artificially increase the dipole-dipole interaction to 100 times its magnitude ($\xi = 10$).

In addition to quantities that we determine asymptotically, the perturbative MQDT calculation also depends on the value of the elimination radius R_{e} since we do not take the limit $R_{\mathrm{e}} \to \infty$. In order to determine the proper value of R_{e}, we need to determine the location beyond which the closed channels have a negligible effect on scattering observables. For example, figure 4.6 shows the position B_0 of the FR between the states $|f = 9/2, m_f = -7/2\rangle$ and $|f = 9/2, m_f = -9/2\rangle$ of potassium as a function of R_{e} with $\xi = 10$. In the region $R_{\mathrm{e}} \lesssim 0.4$, the resonance position shows a rapid dependence on R_{e}. Past this region, the resonance position shows a clear convergence with increasing R_{e}, and we choose $R_{\mathrm{e}} = 1$ for this example problem.

The only open channel with a non-zero partial wave has a classical turning point on the inner side of its d-wave centrifugal barrier at $R_{\mathrm{t}} \approx 0.64$. We choose $R_{\mathrm{e}} = 1$ because this choice achieves a better accuracy than the choice of $R_{\mathrm{e}} = 0.64$. However, because the power-law growth of an open-channel wave function under a centrifugal barrier may lead to numerical instabilities in other problems, we could instead safely choose R_{e} at this turning point, sacrificing approximately 0.5 G of accuracy in the position of this resonance. Although we achieve accurate results with this method, determining a more robust method of treating this type of channel is a possible direction of future research.

4.4.3 Efficiency

One of the main advantages of MQDT is that K^{sr} and the QDT parameters are smooth functions of energy and magnetic or electric field. As previously demonstrated in chapter 2, the zeroth-order MQDT calculation efficiently and accurately determines scattering observables (when $V'(R)$ is negligible beyond R_{m}) by interpolating K^{sr} and the QDT parameters over a wide range of energy and field. This interpolation provides significant computational savings over the FCC calculation, which requires a time-consuming numerical calculation at every energy and magnetic field of interest. The efficiency of MQDT is particularly useful when describing FRs because they tend to be narrow features in energy or field.

In this section, we show that the perturbed scattering observables also depend on quantities

that are smooth in energy and field. We show that the quantity $K^{\mathrm{sr}'}$ exhibits an equally smooth dependence on energy and field as the unperturbed version K^{sr}, and we show that the perturbation integrals in equation (3.37) are nearly constant functions of magnetic field. Interpolating these quantities over a wide range of energy and magnetic field, we show a significant improvement in accuracy over the zeroth-order MQDT calculation, while retaining all of its numerical efficiency.

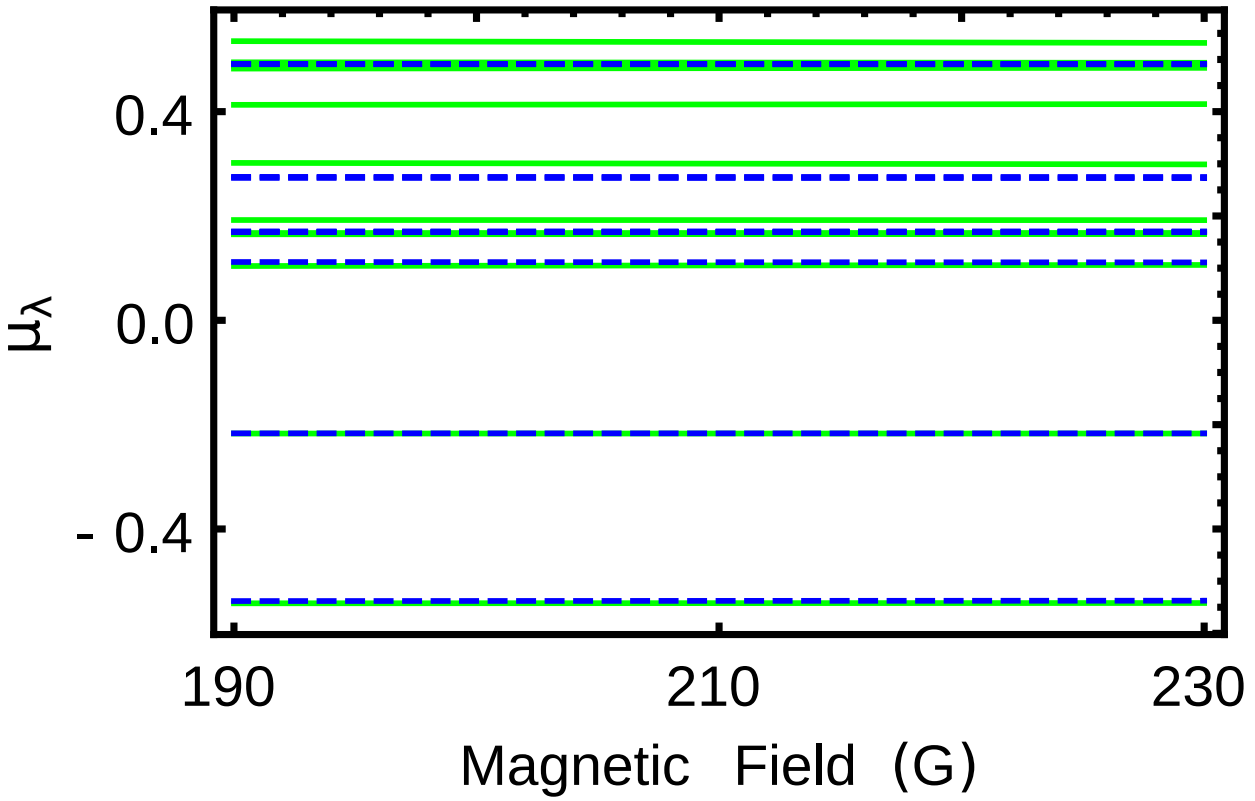

Figure 4.7: These graphs show the quantum defects $\mu_\lambda = \tan\delta_\lambda/\pi$, where the quantities $\tan\delta_\lambda$ are either the eigenvalues of $K^{\rm sr}$ (blue dashed lines) or the eigenvalues of $K^{\rm sr'}$ (green solid lines) as functions of magnetic field in the range $190 - 230$ G. These calculations use $R_{\rm m} \approx 0.31$ and $\xi = 10$. The quantum defects are slightly different in each case, and they are equivalently weak functions of magnetic field. Although this graph contains all thirteen quantum defects for both the perturbative calculation and the non-perturbative calculation, many of the quantum defects overlap on this scale.

Figure 4.7 shows the quantum defects $\mu_\lambda = \tan\delta_\lambda/\pi$, where the quantities $\tan\delta_\lambda$ are either the eigenvalues of $K^{\rm sr}$ (blue dashed lines) or the eigenvalues of $K^{\rm sr'}$ (green solid lines) as functions of magnetic field in the range $190-230$ G. We compute $K^{\rm sr}$ using equation (2.12), and we compute $K^{\rm sr'}$ using equation (3.28). The numerical integration of the one-dimensional integrals in this equation is extremely rapid, owing to the first-order nature of the perturbation theory. We find that the eigenvalues have been only slightly shifted from their unperturbed values, and they remain equally smooth functions in this range of magnetic field. The elements of $K^{\rm sr'}$ are equally smooth quantities, and we therefore achieve a numerically accurate interpolation of these elements by using a coarse field spacing of 10 G, noting that this range and field spacing could be much larger. We then quickly generate $\tilde{K}'$ of equation (3.15) with an arbitrarily fine resolution in field using the interpolated values of $K^{\rm sr'}$ and the QDT parameters.

In order to determine K' of equation (3.37), we only require the small set of one-dimensional perturbation integrals $\int_{R_{\rm m}}^{\infty} f_i(R')V'_{ij}(R')f_j(R'){\rm d}R'$ and $\int_{R_{\rm m}}^{\infty} f_i(R')V'_{ij}(R')g_j(R'){\rm d}R'$, where i and j run over the set of open channels. In this example problem, there are two open channels: the incident s-wave channel, which has a channel collision energy of 1 μK, and an open d-wave channel that has a threshold degenerate with the incident channel. Because these two channels have the same threshold energy at every magnetic field, all of these perturbation integrals are nearly constant functions of magnetic field. We numerically calculate and interpolate these integrals on the same coarse grid as the computation of $K^{\rm sr'}$: from $190-230$ G with a field spacing of 10 G. With K' in hand, we compute $S^{\rm phys'}$ and, therefore, all scattering observables using equation (3.38). Note that we can also use the quantity $K^{\rm sr'}_{\rm QQ} + \cot\gamma$ to efficiently search for FRs.

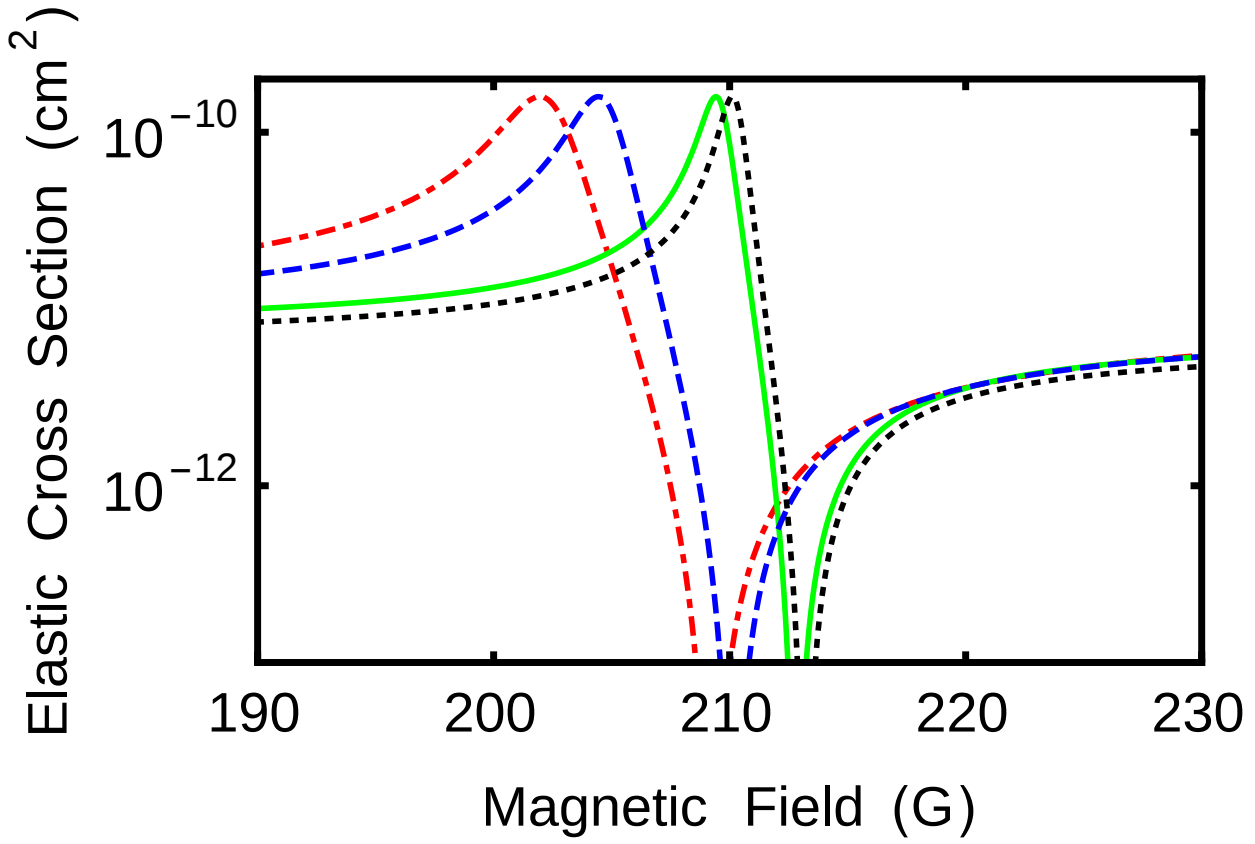

Figure 4.8: This figure shows the s-wave elastic cross section near the FR between the states $|f = 9/2, m_f = -7/2\rangle$ and $|f = 9/2, m_f = -9/2\rangle$ of ^{40}K at a collision energy of 1 μK with an artificially enhanced dipole-dipole interaction. This figure shows three different calculations of the elastic cross section with $\xi = 10$: the zeroth-order MQDT calculation (blue dashed line), the perturbative MQDT calculation (green solid line), and the FCC calculation (black dotted line). As a point of reference, this figure also shows the zeroth-order MQDT calculation of the elastic cross section with $\xi = 1$ (red dot-dashed line). For these calculations, $R_{\rm m} = 40\ a_0$, and $R_{\rm e} = 1\ \beta$, where β is the van der Waals length.

4.4.4 Accuracy

In this section, we demonstrate the accuracy of the perturbative MQDT method by comparing its results to the zeroth-order MQDT calculation and to the FCC calculation. For these calculations, we choose $R_{\mathrm{m}} = 40\ a_0$ and $R_{\mathrm{e}} = 1\ \beta$, where β is the van der Waals length. Figure 4.8 shows the s-wave elastic cross section near the FR between the states $|f = 9/2, m_f = -7/2\rangle$ and $|f = 9/2, m_f = -9/2\rangle$ of ^{40}K at a collision energy of 1 μK. The red dot-dashed line is the result of the zeroth-order MQDT calculation for natural potassium, corresponding to a dipole-dipole interaction with $\xi = 1$. This calculation agrees well with the FCC calculation at the same interaction strength. The other three lines on this graph represent calculations in which the dipole-dipole interaction has been artificially increased to 100 times the strength of natural potassium ($\xi = 10$). The choice of $\xi = 10$ corresponds to the most magnetic atom, dysprosium ($\mu = 10\ \mu_{\mathrm{B}}$). The blue dashed line represents the zeroth-order MQDT calculation. We see a significant change in the resonance position and width, even though this calculation only includes the enhanced dipolar interaction at distances less than R_{m}. We compute the solid green line using the perturbation theory of chapter 3, and the FCC calculation produces the black dotted line. Figure 4.8 shows that the influence of the dipole-dipole interaction with $\xi = 10$ is significant beyond R_{m}, shifting this particular resonance by roughly 5 G. The perturbative MQDT calculation approximately tracks this shift.

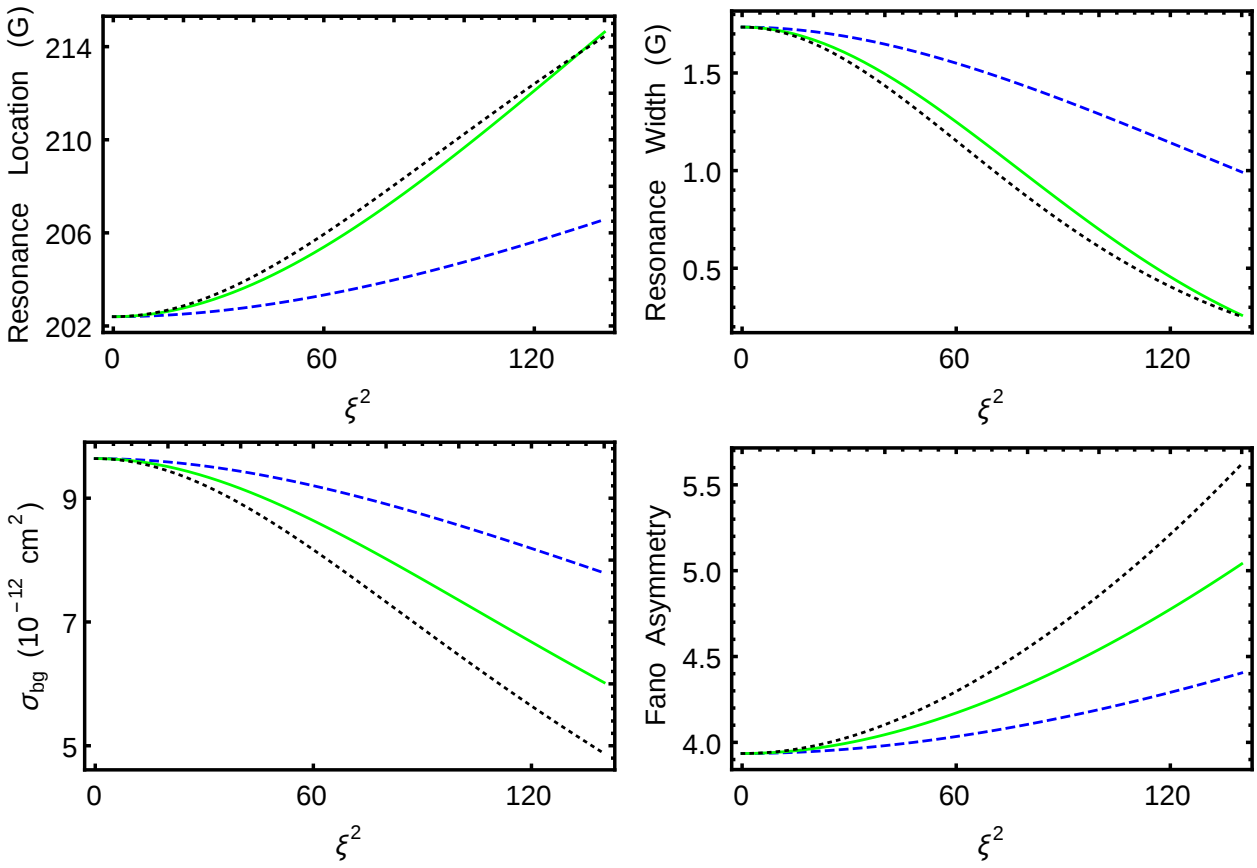

Figure 4.9: This figure shows the resonance field location B_0 (top left panel), the resonance field width Δ (top right panel), the background elastic cross section $\sigma_{\rm bg}$ (bottom left panel), and the Fano asymmetry parameter q (bottom right panel). Each panel shows three different calculations: the zeroth-order MQDT calculation (blue dashed line), the perturbative MQDT calculation (green solid line), and the FCC calculation (black dotted line). For these calculations, $R_{\rm m} = 40\ a_0$, and $R_{\rm e} = 1\ \beta$, where β is the van der Waals length.

We further investigate the accuracy of the perturbative MQDT method by using it to calculate the shape of this same FR as a function of magnetic field for different values of ξ. We again compare this calculation to both the zeroth-order MQDT calculation and the FCC calculation. We describe a resonance by computing the elastic cross section $\sigma(B)$ near the resonance and fitting it to the following form,

$$\sigma(B) = \sigma_{\rm bg} \frac{\big((B - B_0)/\Delta - q\big)^2}{1 + \big((B - B_0)/\Delta\big)^2}, \tag{4.13}$$

where B_0 is the resonance field position, Δ is the resonance field width, $\sigma_{\rm bg}$ is the background elastic scattering cross section, and q is the Fano asymmetry parameter [19]. Figure 4.9 compares three different methods of calculating these resonance properties, plotted as a function of ξ^2. Figure 4.9(a) shows B_0; figure 4.9(b) shows Δ; figure 4.9(c) shows $a_{\rm bg}$; and 4.9(d) shows q. Each figure shows a blue dashed line for the zeroth-order MQDT calculation, a green solid line for the perturbative MQDT calculation, and a black dotted line for the FCC calculation.

The dipolar coupling between channels gives the resonance properties B_0, Δ, $\sigma_{\rm bg}$, and q a quadratic dependence on ξ^2 at small ξ. Even though the perturbative MQDT calculation uses only a first-order distorted wave approximation, the perturbation theory tracks this quadratic behavior and significantly improves the zeroth-order MQDT result for each quantity and at all interaction strengths. The perturbation theory appears to more accurately account for the shift in the resonance location and width than for the shift in the background elastic cross section and the Fano asymmetry parameter. The absolute error in this particular resonance location for this artificial model is 0.41 G for a dipole strength of erbium ($\xi = 7$) and 0.59 G for a dipole strength of dysprosium ($\xi = 10$).

4.5 Summary

We successfully applied MQDT to collisions between alkali atoms, including high partial waves. We used the efficiency of MQDT to locate and characterize many Fano-Feshbach resonances in the collisions ^{40}K + ^{85}Rb and ^{133}Li + ^{6}Cs. We also developed a method to pertur-

batively incorporate long-range anisotropic interactions within MQDT. In the presence of strong dipolar coupling, this method allowed for an enhanced accuracy in the calculation of scattering observables in terms of quantities that weakly depend on energy and field. We demonstrated that the perturbative MQDT method is capable of retaining sub-G accuracy in the calculation of a particular Fano-Feshbach resonance position in ultracold scattering of potassium atoms with an artificially enhanced dipole-dipole interaction. This study included the entire range of atomic dipole strengths and beyond.

Chapter 5

Molecular Scattering

This chapter contains material in references [87] and [88].

5.1 Introduction

The ultracold scattering of molecules may provide a sensitive probe of chemical reaction dynamics. Cooling molecules to ultracold temperatures allows one to prepare the reactant molecules in a single quantum state with very small transnational kinetic energy at large separations. Modest external magnetic and electric fields greatly influence the character of this state and, therefore, may have a profound effect on chemical reactions [89–93]. Studying the products of the reaction and their dependence on external fields may lead to a more detailed understanding of the reaction complex. At the same time, the sensitive dependence on field allows for the control of chemical reactions. This kind of control has been demonstrated in a prototype experiment involving KRb molecules [94, 95].

In typical ultracold chemical reactions, the kinetic energy at short-range, where the reaction dynamics take place, is on the order of $10 - 1000$ K, and the asymptotic translational energy in the reactant channels is on the ultra-low energy scale near 1 μK. While the FCC calculation can handle this disparity in energy scales, the computations become impractically large when one includes all of the relevant quantum states and external field effects. As a result, the vast majority of FCC calculations of ultracold reactions only consider field-free cases without the inclusion of spin and hyperfine splitting [89–93, 96–101]. Although Tscherbul and Krems [102] have formulated

the theory of chemical reactions for an atom-diatom system in external fields and have applied the theory to the Li + HF reaction, the computations remain demanding.

MQDT makes use of this disparity in energy scales to greatly simplify these types of calculations, as it did for the atomic case in chapter 4. Previous extensions of MQDT describe atom-molecule systems [39,103] and molecule-molecule reactive scattering [47,49,104,105]. These MQDT methods estimate the overall reaction rate coefficients of several barrierless reactions [47,104] at far less computational expense than the FCC calculations. However, these implementations of MQDT only estimate the total reaction rate coefficient. They do not include the rotational and vibrational degrees of freedom and, therefore, cannot calculate the ro-vibrational populations of the reaction products.

In this chapter, we develop an MQDT treatment of non-reactive and reactive molecular scattering that is fully capable of including external-field effects and also includes ro-vibrational degrees of freedom. To accomplish this, we take advantage of two different coordinate systems. One of these coordinate systems best describes the short-range region, and the other one best describes the long-range region. This chapter explains the key features in this extension of MQDT, and it closely follows references [87] and [88]. For non-reactive molecular collisions, reference [87] straightforwardly applies the MQDT formalism of chapter 2 beyond the matching radius R_{m} in terms of a single long-range coordinate system. For reactive molecular collisions, reference [88] transforms the log-derivative matrix between the two different coordinate systems that best describe each region.

The construction of short-range potentials and the solution of the coupled-channel Schrödinger equation at short-range involve many complications that are explained in references [87] and [88]. We use the results of the FCC calculations to compare the accuracy of our extensions of MQDT. As an example, we apply this theory to the non-reactive scattering of H_2 + H_2 molecules and the reactive scattering of D + H_2 molecules. The molecular MQDT results show excellent agreement with the FCC calculations, and K^{sr} remains smooth and weakly energy dependent for these cases.

5.2 $\mathbf{H}_2(v_1, j_1) + \mathbf{H}_2(v_2, j_2)$

The MQDT formalism of chapter 2 is directly applicable to molecular collisions that involve ro-vibrational degrees of freedom. As an example, we demonstrate the ability of MQDT to accurately describe a particular scattering process of the collision H_2 + H_2. We focus on the quasi-resonant energy transfer in para-para H_2 scattering, which involves a non-trivial exchange of energy at short-range. The vibrational quantum number v and the rotational quantum number j describe the state of each $H_2(v, j)$ molecule. We choose to describe the particular scattering process $(v_1, j_1, v_2, j_2) = (1, 0, 0, 2) \rightarrow (1, 2, 0, 0)$. In this process, a vibrating rotationless molecule in the state $(v = 1, j = 0)$ collides with a rotating vibrationless molecule in the state $(v = 0, j = 2)$. The collision transfers the rotational energy between the two molecules, releasing a kinetic energy of approximately 25 K.

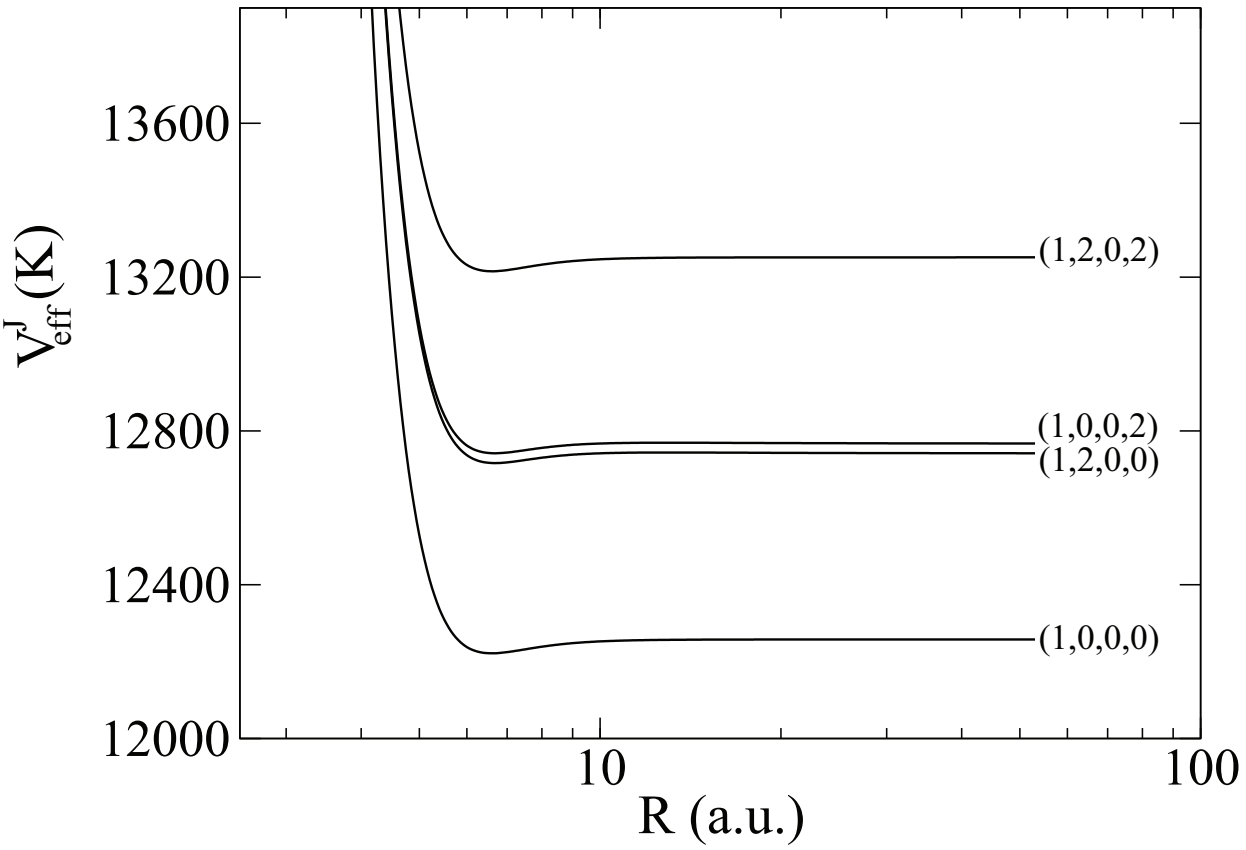

Figure 5.1: This figure shows the effective diabatic potential energies that are relevant in the quasi-resonant scattering process $(v_1, j_1, v_2, j_2) = (1, 0, 0, 2) \rightarrow (1, 2, 0, 0)$ of two H_2 molecules. The process is quasi-resonant because the molecular states are nearly degenerate, being asymptotically separated by approximately 25 K. An asymptotic energy spacing of approximately 400 K separates the other relevant channels from the incident channel $(1, 0, 0, 2)$.

The collision process $(v_1, j_1, v_2, j_2) = (1, 0, 0, 2) \rightarrow (1, 2, 0, 0)$ conserves the total rotational angular momentum. This type of process is known to be highly state-selective [106], and one only needs to include the channels $(1, 0, 0, 2)$ and $(1, 2, 0, 0)$ in order to accurately describe this process [87]. Hence, we construct a greatly simplified scattering model that accurately describes this process by only including the four channels $(1, 0, 0, 0)$, $(1, 0, 0, 2)$, $(1, 2, 0, 0)$ and $(1, 2, 0, 2)$. Figure 5.1 shows the effective diabatic potential energies $V^J_{\rm eff}(R)$ that asymptotically correspond to these states, where R is the separation between the H_2 molecules. Reference [87] details the construction of $V^J_{\rm eff}(R)$. This model is accurate, in part, because the process $(1, 0, 0, 2) \rightarrow (1, 2, 0, 0)$ is quasi-resonant, meaning that the molecular states $(1, 0, 0, 2)$ and $(1, 2, 0, 0)$ are nearly degenerate. Their energies differ by approximately 25 K, and approximately 400 K separates the other molecular states. The FCC calculation and the MQDT calculation both use this reduced set of channels.

Similar to the applications of MQDT to alkali atom scattering in chapter 4, we find that the isotropic potential $V^{\rm lr}(R)$ is a good approximation to $V^J_{\rm eff}(R)$ at large R when $V^{\rm lr}(R)$ has the following form,

$$V^{\rm lr}(R) = -C_6/R^6 - C_8/R^8 - C_{10}/R^{10}. \tag{5.1}$$

This potential has the same form as in equation (2.8). To determine the dispersion coefficients C_6, C_8, and C_{10}, we fit the asymptotic expansion of $V^J_{\rm eff}(R)$ for each channel to the form of $V^{\rm lr}(R)$ in equation (5.1).

The potential energy curves in figure 5.1 have a qualitatively different character than in the alkali-atom case. The weakly polarizable H_2 molecules have a small C_6, producing a potential depth that is small compared to the rotational splitting. At at collision energy 1 μK above the incident channel $(1, 0, 0, 2)$, the channel $(1, 2, 0, 2)$ remains classically forbidden over the entire range of R. This means that one cannot choose the matching radius $R_{\rm m}$ in a region where all channels are locally open. However, the well depth of channel $(1, 2, 0, 2)$ is so small that it remains well separated in energy from the other channels at short range. We find that the MQDT formalism of chapter 2 produces a $K^{\rm sr}$ that is nearly constant in energy, and we simply use its value at zero

energy for the MQDT calculation.

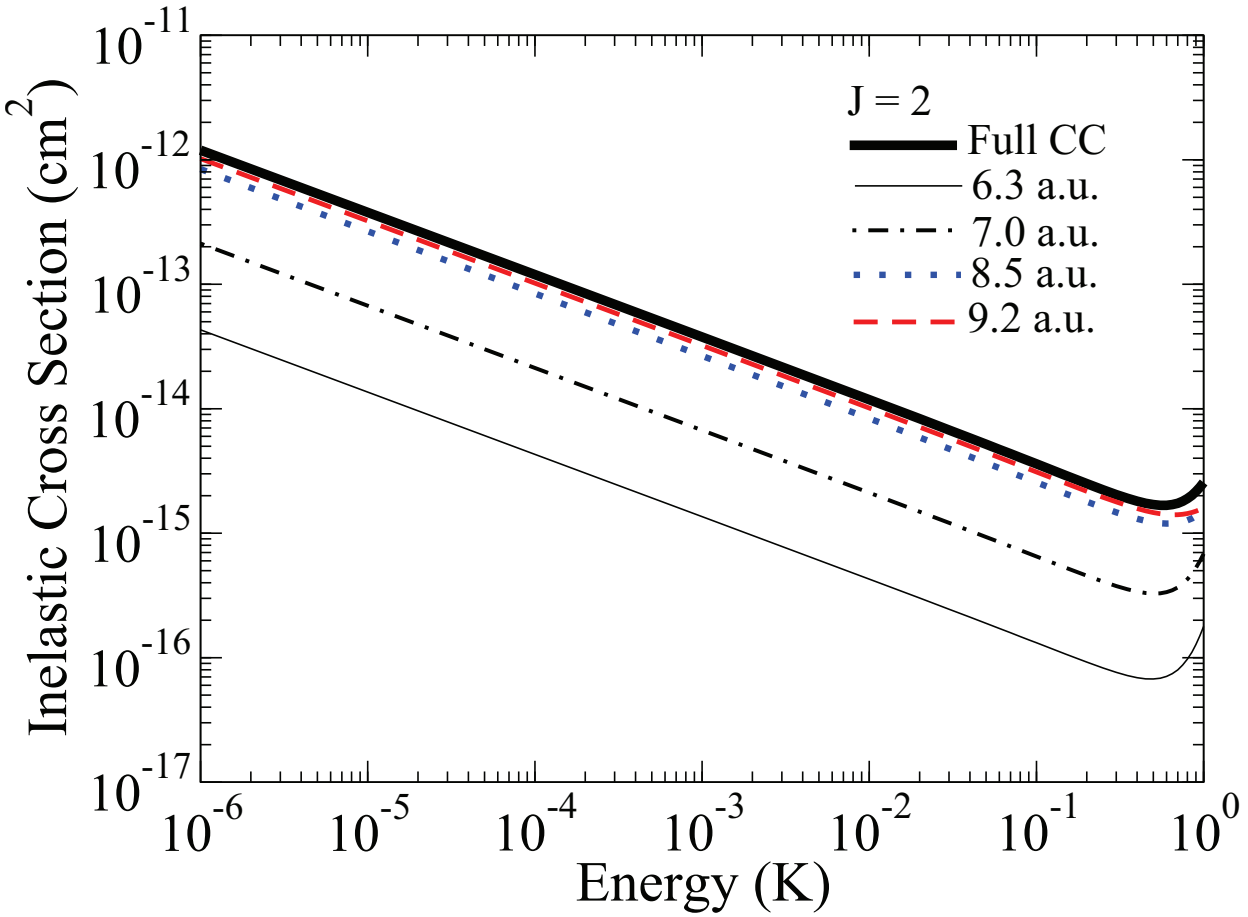

Figure 5.2: This figure shows the inelastic cross section for the quasi-resonant scattering process $(v_1, j_1, v_2, j_2) = (1, 0, 0, 2) \rightarrow (1, 2, 0, 0)$ of two H_2 molecules. This figure compares the FCC calculation (thick black line) to the MQDT calculation with a matching radius of $R_m = 6.3\ a_0$ (thin black line), 7.0 a_0 (black dot-dashed line), 8.5 a_0 (blue dotted line), and 9.2 a_0 (red dashed line). The MQDT calculation uses the single value of K^{sr} computed at zero energy. This calculation converges to the FCC calculation as we increase R_m.

Figure 5.2 shows that MQDT is able to accurately describe the quasi-resonant scattering process $(v_1, j_1, v_2, j_2) = (1, 0, 0, 2) \rightarrow (1, 2, 0, 0)$ of two H_2 molecules over an energy range that spans six orders of magnitude, even though MQDT only uses the value of K^{sr} at zero energy. This figure shows the inelastic cross section for this process, as computed by the FCC calculation (thick black line) and by the MQDT calculation with a matching radius of $R_{\mathrm{m}} = 6.3\ a_0$ (thin black line), 7.0 a_0 (black dot-dashed line), 8.5 a_0 (blue dotted line), and 9.2 a_0 (red dashed line). The MQDT calculation converges to the FCC calculation as we increase R_{m}. The MQDT calculation is nearly converged at $R_{\mathrm{m}} = 9.2\ a_0$, which is on the order of the van der Waals length for this system $R_{\mathrm{vdW}} = 14.5\ a_0$.

5.3 MQDT for Chemical Reactions

Chemical reactions add additional complexity to scattering calculations, and MQDT can greatly simplify these calculations. In order to use MQDT to describe cold chemistry, one needs to slightly modify the matching procedure at R_{m} to incorporate a transformation between different coordinate systems. One best describes the short-range interactions that influence chemical reactions in hyperspherical coordinates [107], and one best describes the long-range interactions between the reactants or products in Jacobi coordinates. Both of these coordinate systems use the Euler angles as external coordinates; however, the internal coordinates are different. For atom-diatom collisions, there are three possible arrangements of the three atoms. We label the possible arrangements by τ. Jacobi coordinates describe these arrangements in terms of s_τ and S_τ. The separation s_τ is the internuclear distance between the constituents of the diatom. The separation S_τ is the distance between the diatom center of mass and the remaining atom. The following transformation defines the Delves hyperspherical coordinates in terms of s_τ and S_τ,

$$\rho = \left(s_\tau^2 + S_\tau^2\right)^{1/2} \tag{5.2a}$$

$$\theta_\tau = \tan^{-1}\left(s_\tau / S_\tau\right), \tag{5.2b}$$

where ρ is the hyperradius and θ_τ is one hyperangle. The other hyperangle γ_τ is the angle between the vectors $\vec{s}_\tau$ and $\vec{S}_\tau$.

Reference [88] supplies the detailed construction of the log-derivative matrix $Y(\rho)$, following a standard procedure developed in references [108] and [102]. After constructing $Y(\rho)$ at short range, we use $Y(\rho)$ as a boundary condition on the log-derivative of $M(S_\tau)$ at the matching separation S_m, which is independent of τ. Analogous to chapter 2, we define $M(S_\tau)$ as a the following linear combination of the reference wave functions $\hat{f}(S_\tau)$ and $\hat{g}(S_\tau)$ at $S_\tau \geq S_\mathrm{m}$,

$$M_{ij}(S_\tau) = \hat{f}_i(S_\tau)\delta_{ij} - \hat{g}_i(S_\tau)K^{\mathrm{sr}}_{ij}. \tag{5.3}$$

This equation defines K^{sr}. Reference [88] details the exact matching procedure we use to determine K^{sr} from $Y(\rho)$.

The reference wave functions $\hat{f}(S_\tau)$ and $\hat{g}(S_\tau)$ represent a pair of linearly independent reference functions in each channel, satisfying the following radial Schrödinger equation,

$$\left(-\frac{\mathrm{d}^2}{\mathrm{d}S_\tau^2} + \frac{L_i(L_i+1)}{S_\tau^2} + V^{\mathrm{lr}}(S_\tau)\right)\begin{Bmatrix} \hat{f}_i \\ \\ \hat{g}_i \end{Bmatrix} = E_i \begin{Bmatrix} \hat{f}_i \\ \\ \hat{g}_i \end{Bmatrix}. \tag{5.4}$$

The quantum number L_i specifies the partial wave, and E_i is the kinetic energy in channel i. Similar to the previous chapters, S is in units of the natural length scale $\beta = (2\mu C_6/\hbar^2)^{1/4}$ of the potential $-C_6/R^6$, and E_i is in units of the natural energy scale $E_\beta = \hbar^2/2\mu\beta^2$. However, in this chapter, we use the reduced mass of the three-body system $\mu = \sqrt{m_1 m_2 m_3/(m_1+m_2+m_3)}$. The channel index i asymptotically correlates with the separated molecule quantum numbers $\{v, j, L\}$ and with the arrangement τ. The long-range reference potential $V^{\mathrm{lr}}(S_\tau)$ takes the following form,

$$V^{\mathrm{lr}}(S_\tau) = -C_6/S_\tau^6 - C_8/S_\tau^8 - C_{10}/S_\tau^{10}. \tag{5.5}$$

The definition of K^{sr} in equation (5.3) is naturally tied to the definition of the reference functions $\hat{f}(R)$ and $\hat{g}(R)$. For typical atom-diatom collisions, we can make a simplifying approximation in the product channels. The kinetic energy is often sufficiently large in the product channels that the reference potential $V^{\mathrm{lr}}(S_\tau)$ is negligible beyond S_m. In this case, we do not use the same

definition of the reference wave functions $\hat{f}(S_\tau)$ and $\hat{g}(S_\tau)$ as in the rest of this thesis. We simply choose the reference wave functions $\hat{f}(S_\tau)$ and $\hat{g}(S_\tau)$ to be the energy-normalized free-particle solutions $f(S_\tau)$ and $g(S_\tau)$ in the product channels,

$$\hat{f}_i(S_\tau) = f_i(S_\tau) = k_i^{1/2} S_\tau j_{L_i}(k_i S_\tau) \tag{5.6a}$$

$$\hat{g}_i(S_\tau) = g_i(S_\tau) = k_i^{1/2} S_\tau n_{L_i}(k_i S_\tau). \tag{5.6b}$$

where $k_i = \sqrt{E_i}$. The functions $j_{L_i}(k_i S_\tau)$ and $n_{L_i}(k_i S_\tau)$ are the spherical Bessel functions of the first and second kind, respectively. The set of equations (5.6) does not merely specify boundary conditions on the reference wave functions; we let $\hat{f}(S_\tau)$ and $\hat{g}(S_\tau)$ have this functional form at all $S_\tau \geq S_\mathrm{m}$ in the product channels. Indeed, using this set of reference wave functions is a suitable choice in any channel that has very high kinetic energy, whether or not that channel is a product or reactant channel.

In cold atom-diatom collisions, the kinetic energy in the reactant channels is typically in the mK–μK range, and the long-range reference potential is *not* negligible. As the solutions $f(S_\tau)$ and $g(S_\tau)$ in equation (5.6) strongly depend on energy in the threshold regime, we make a different choice for $\hat{f}(S_\tau)$ and $\hat{g}(S_\tau)$ in the reactant channels. We choose to give these reference wave functions WKB-like boundary conditions at short range. Using this kind of reference wave function is not typical in quantum chemistry. These functions are not energy-normalized, and they weakly depend on energy in the threshold regime.

Specifically, we define $\hat{f}(S_\tau)$ and $\hat{g}(S_\tau)$ by the following WKB-like boundary conditions at S_x in the reactant channels,

$$\hat{f}_i(S_\tau) = \frac{1}{\sqrt{k_i(S_\tau)}} \sin\left(\int_{S_x}^{S_\tau} k_i(S'_\tau) dS'_\tau + \phi_i\right) \quad \text{at} \quad S_\tau = S_\mathrm{x} \tag{5.7a}$$

$$\hat{g}_i(S_\tau) = -\frac{1}{\sqrt{k_i(S_\tau)}} \cos\left(\int_{S_x}^{S_\tau} k_i(S'_\tau) dS'_\tau + \phi_i\right) \quad \text{at} \quad S_\tau = S_\mathrm{x}, \tag{5.7b}$$

where $k_i(S_\tau) = \sqrt{E_i - V^\mathrm{lr}(S_\tau)}$. These are the same reference wave functions that we use in the rest of this thesis. We choose a small enough S_x that the kinetic energy in the reference potential at S_x is positive in every channel. The phase ϕ_i is chosen in the same manner as in chapter 2

in order to preserve the numerical linear independence of these functions in the asymptotic limit, even in the threshold regime when the partial wave is nonzero. The standard MQDT transformations of chapter 2 relate these solutions to the energy-normalized solutions $f(S_\tau)$ and $g(S_\tau)$ in the asymptotic limit. In the reactant channels,

$$\hat{f}_i(S_\tau)\mathcal{A}_i^{1/2} \xrightarrow{S_\tau\to\infty} \quad f_i(S_\tau) \tag{5.8a}$$

$$\hat{f}_i(S_\tau)\mathcal{A}_i^{-1/2}\mathcal{G}_i + \hat{g}_i(S_\tau)\mathcal{A}_i^{-1/2} \xrightarrow{S_\tau\to\infty} \quad g_i(S_\tau). \tag{5.8b}$$

The main feature of K^{sr} in the theory is that it is generally only weakly dependent on energy in the ultracold regime near the threshold of the reactants. We demonstrate that K^{sr} is weakly dependent on energy for a specific example in the next section. When K^{sr} is a smooth function of energy, we can interpolate K^{sr} over a wide range of collision energies, reducing the number of energies at which we must perform the full hyperspherical calculation.

After interpolating K^{sr}, we perform the MQDT procedure that produces the physical scattering matrix S^{phys} from K^{sr}. We eliminate the closed channels in the typical MQDT fashion, yielding the reduced K-matrix $\tilde{K}$,

$$\tilde{K} = K^{\mathrm{sr}}_{\mathrm{PP}} - K^{\mathrm{sr}}_{\mathrm{PQ}}\left(\cot\gamma + K^{\mathrm{sr}}_{\mathrm{QQ}}\right)^{-1} K^{\mathrm{sr}}_{\mathrm{QP}}. \tag{5.9}$$

We now adapt the MQDT transformation to account for the simple choice of reference wave functions in the product channels, given by equation (5.6). To perform this transformation, we conveniently repartition $\tilde{K}$ into reactant (R) channels and product (P) channels,

$$\tilde{K} = \begin{pmatrix} \tilde{K}_{\mathrm{RR}} & \tilde{K}_{\mathrm{RP}} \\ \tilde{K}_{\mathrm{PR}} & \tilde{K}_{\mathrm{PP}} \end{pmatrix},$$

not to be confused with P and Q. There remains only the matter of translating the reference functions $\hat{f}(S_\tau)$ and $\hat{g}(S_\tau)$ into the energy-normalized versions $f(S_\tau)$ and $g(S_\tau)$. In the product channels, no transformation is necessary because we use the relations in equation (5.6). In the reactant channels, we use the relations in equation (5.8).

In block notation, the final expression for K becomes,

$$K_{\mathrm{RR}} = \mathcal{A}^{1/2}(I_{\mathrm{R}} + \tilde{K}_{\mathrm{RR}}\mathcal{G})^{-1}\tilde{K}_{\mathrm{RR}}\mathcal{A}^{1/2} \tag{5.10}$$

$$K_{\mathrm{PR}} = \tilde{K}_{\mathrm{PR}}\left(I_{\mathrm{R}} - \mathcal{G}(I_{\mathrm{R}} + \tilde{K}_{\mathrm{RR}}\mathcal{G})^{-1}\tilde{K}_{\mathrm{RR}}\right)\mathcal{A}^{1/2} \tag{5.11}$$

$$K_{\mathrm{RP}} = \mathcal{A}^{1/2}(I_{\mathrm{R}} + \tilde{K}_{\mathrm{RR}}\mathcal{G})^{-1}\tilde{K}_{\mathrm{RP}} \tag{5.12}$$

$$K_{\mathrm{PP}} = \tilde{K}_{\mathrm{PP}} - \tilde{K}_{\mathrm{PR}}\mathcal{G}(I_{\mathrm{R}} + \tilde{K}_{\mathrm{RR}}\mathcal{G})^{-1}\tilde{K}_{\mathrm{RP}}, \tag{5.13}$$

where I_{R} is the $N_{\mathrm{r}} \times N_{\mathrm{r}}$ identity matrix and N_{r} is the number of reactant channels. We illustrate the symmetry of K by the following transformation,

$$K_{\mathrm{RP}}^{T} = \tilde{K}_{\mathrm{PR}}(I_{\mathrm{R}} + \mathcal{G}\tilde{K}_{\mathrm{RR}})^{-1}\mathcal{A}^{1/2} \tag{5.14}$$

$$= \tilde{K}_{\mathrm{PR}}\left(I_{\mathrm{R}} - (\tilde{K}_{\mathrm{RR}}^{-1}\mathcal{G}^{-1} + I_{\mathrm{R}})^{-1}\right)\mathcal{A}^{1/2} \tag{5.15}$$

$$= \tilde{K}_{\mathrm{PR}}\left(I_{\mathrm{R}} - \mathcal{G}(I_{\mathrm{R}} + \tilde{K}_{\mathrm{RR}}\mathcal{G})^{-1}\tilde{K}_{\mathrm{RR}}\right)\mathcal{A}^{1/2} \tag{5.16}$$

$$= K_{\mathrm{PR}}. \tag{5.17}$$

We use Woodbury's matrix identity [109] to arrive at equation (5.15). We must also incorporate the additional phase shift η that the reactant-channel reference wave functions experience during their propagation in the long-range potential $V^{\mathrm{lr}}(S_\tau)$. This leads to the physical scattering matrix,

$$S^{\mathrm{phys}} = \begin{pmatrix} e^{i\eta} & 0 \\ 0 & I_{\mathrm{P}} \end{pmatrix}(\mathcal{I} + iK)(\mathcal{I} - iK)^{-1}\begin{pmatrix} e^{i\eta} & 0 \\ 0 & I_{\mathrm{P}} \end{pmatrix}.$$

The matrix $\mathcal{I}$ is the $N_{\mathrm{o}} \times N_{\mathrm{o}}$ identity matrix, where N_{o} is the number of open channels.

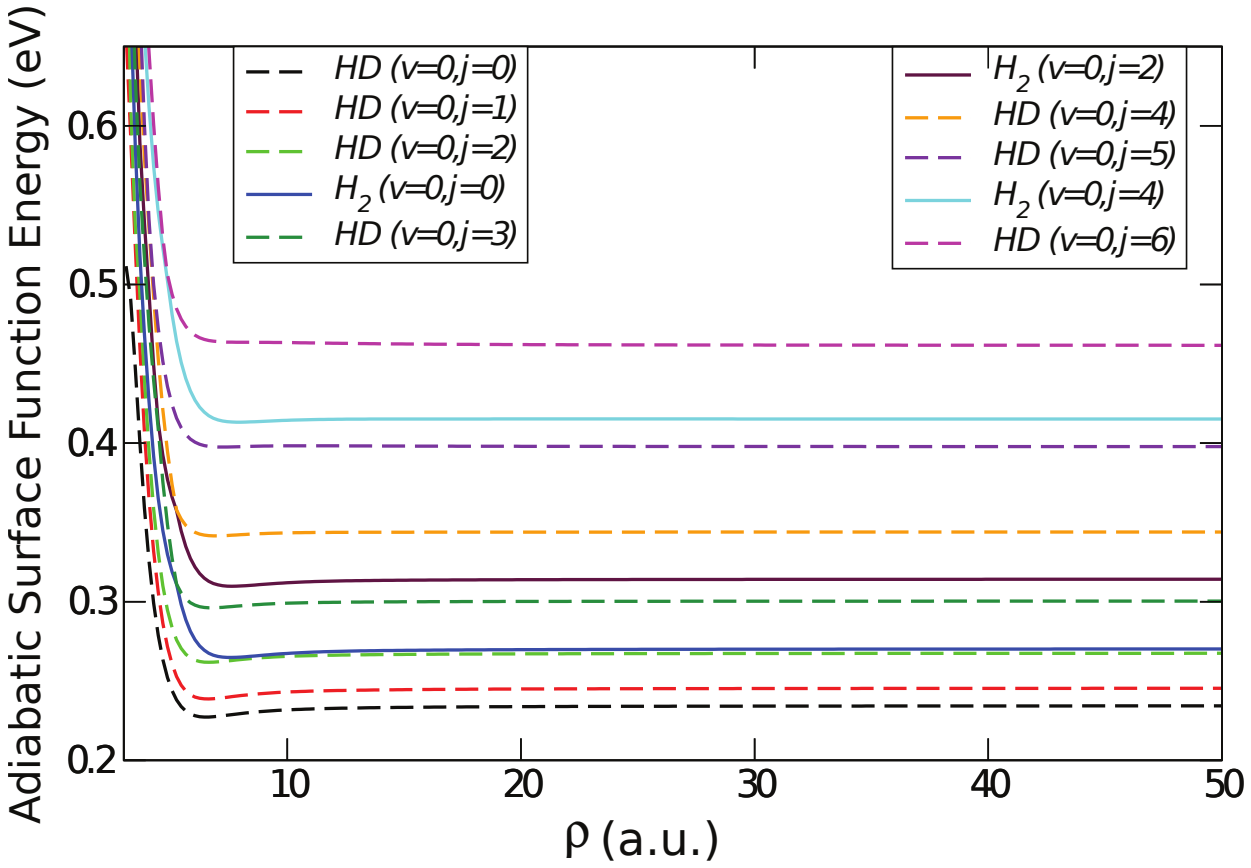

Figure 5.3: This graph shows the ten lowest adiabatic surface function energies $\epsilon_n(\rho)$ (defined in reference [88]) as a function of the hyperradius ρ for the D + $H_2(v = 0, j = 0)$ system with $J = 0$. Each adiabatic curve asymptotically correlates with a unique ro-vibrational level of either the H_2 molecule or the DH molecule, as indicated in the figure.

5.4 $\mathbf{D + H_2}(v, j) \rightarrow \mathbf{HD}(v', j') + \mathbf{H}$

As an illustrative example, we apply the above approach for reactive scattering to the reaction D + $H_2(v, j) \rightarrow HD(v', j')$ + H. This approach requires an accurate description of the long-range potential in the reactant channels, where we use the MQDT reference wave functions. Since most of the available potential energy surfaces for elementary chemical reactions do not provide an accurate treatment of the long-range interaction, a reliable description of reactive scattering in ultracold collisions continues to be a challenge. The availability of an accurate potential energy surface for D + H_2 motivates the choice of using this collision as an example. We use the potential energy surface of Mielke et al. [110] that includes the long-range forces for the diatomic species. Reference [88] details the construction of the diabatic potential matrix $V_\tau(S_\tau)$ and the adiabatic surface function energies $\epsilon_n(\rho)$. Figure 5.3 shows the ten lowest values of $\epsilon_n(\rho)$ for the D + H_2 system with $J = 0$. Each adiabatic curves asymptotically correlates with a unique ro-vibrational level of either the H_2 molecule or the HD molecule. We also calculate similar energies for the higher ro-vibrational levels of these molecules.

We numerically compute the MQDT reference functions and parameters by solving the one-dimensional Schrödinger equation (5.4). We use the form of $V^{\mathrm{lr}}(S_\tau)$ in equation (5.1). Constructing this potential requires the dispersion coefficients C_6, C_8, and C_{10} for the D + H_2 atom-diatom interactions. We numerically extract effective values of the dispersion coefficients by fitting the long-range part of the lowest diagonal element of $V_\tau(S_\tau)$ to the form of $V^{\mathrm{lr}}(S_\tau)$. The effective dispersion coefficients are slightly sensitive to the initial vibrational level of H_2, but we use the same $v = 0$ coefficients for all vibrational levels.

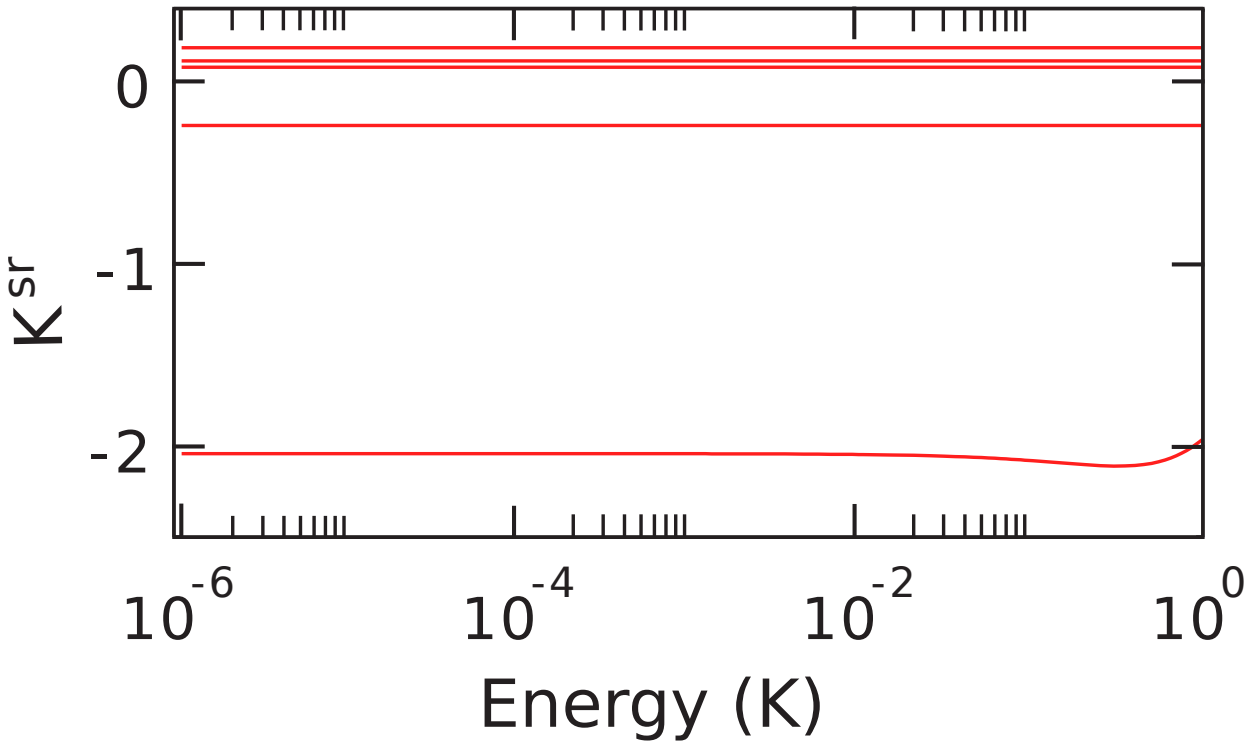

Figure 5.4: This figure shows the diagonal elements of K^{sr} in the reactant channels as a function of collision energy for $R_{\mathrm{m}} = 20\ a_0$.

Figure 5.4 shows the diagonal elements of $K^{\rm sr}$ in the reactant channels as a function of collision energy. We choose the state $(v, j) = (0, 0)$ of the H_2 molecule as the incident channel. The matching radius is 20 a_0. Figure 5.4 clearly demonstrates that $K^{\rm sr}$ is weakly dependent on energy in the ultracold regime, and it maintains this behavior up to 100 mK. Beyond this range, $K^{\rm sr}$ becomes a smooth function of energy. Hence, we divide the interpolation of $K^{\rm sr}$ into two different ranges of collision energy: the ultra-low energy range $E = 1$ μK – 1 mK, and the energy range $E = 100$ mK – 1 K. In the ultra-low regime, we use a linear fit to the value of $K^{\rm sr}$ at 1 μK and 1 mK. At higher energies, we interpolate $K^{\rm sr}$ on a grid with an energy spacing of 200 mK.

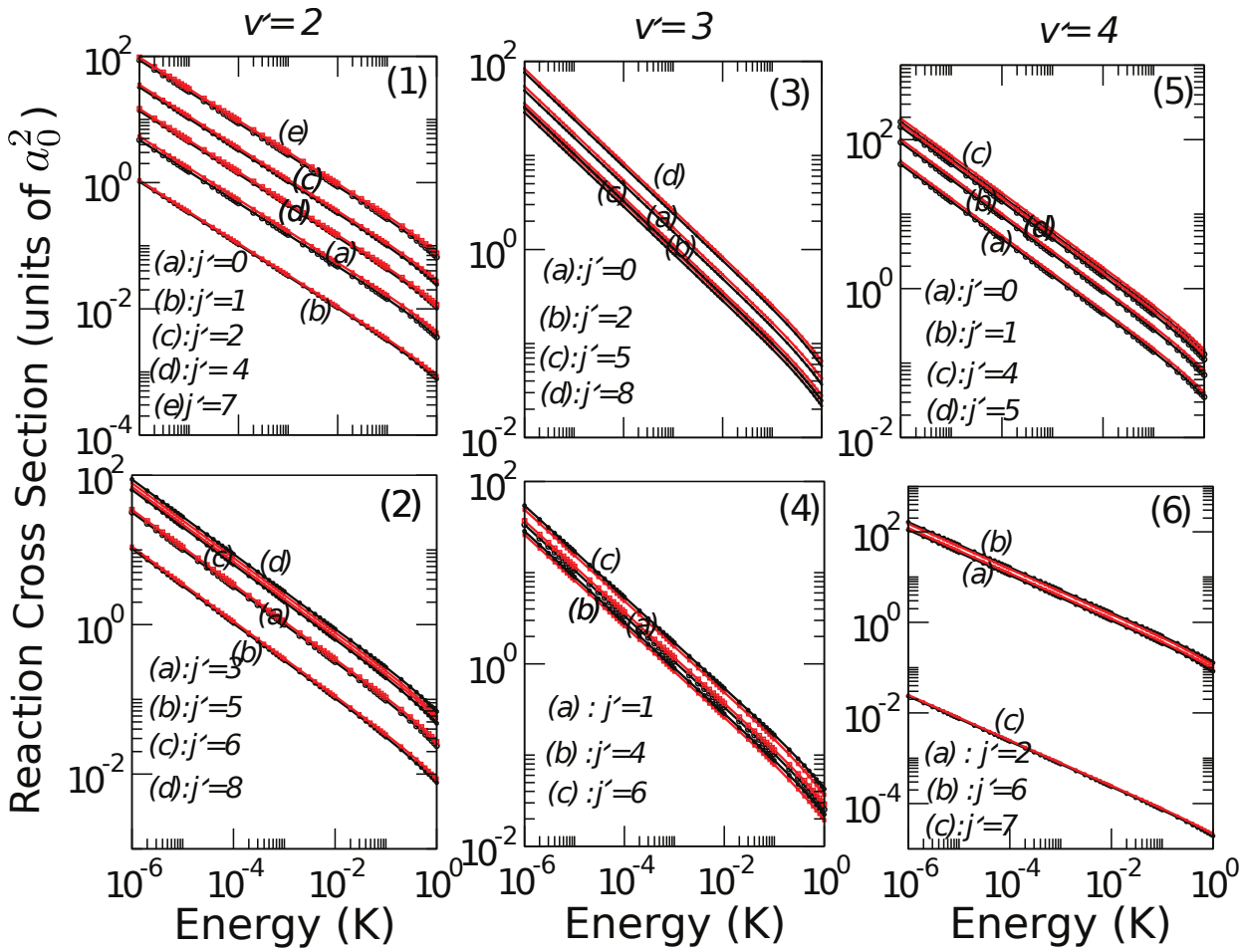

Figure 5.5: This figure compares the FCC calculation and the MQDT calculation of the rotationally resolved reaction cross sections for the HD product in collisions of D + $H_2(v = 4, j = 0)$. The left panels (1 and 2) correspond to HD$(v' = 2, j')$, the middle panels (3 and 4) correspond to HD$(v' = 3, j')$, and the right panels (5 and 6) correspond to HD$(v' = 4, j')$.

The MQDT approach above provides the same full quantum state resolution of reaction products as in FCC calculations, an aspect missing from previous MQDT treatments of ultracold chemistry. As an illustrative example, we choose to study collisions with H_2 in the initial state $(v, j) = (4, 0)$, which allows for the population of several ro-vibrational levels of the HD molecule. Figure 5.5 compares the FCC calculation and the MQDT calculation of the rotationally resolved cross sections for the HD product in different energetically open vibrational levels. The different panels correspond to the rotational distributions in the three highest populated vibrational levels of HD $v' = 2, 3, \text{and } 4$. The black curves are the FCC results, and the red curves are the MQDT results.

The agreement between the FCC calculation and the MQDT calculation is excellent. This clearly indicates that K^{sr} fully characterizes the short-range reaction dynamics. We attribute any small difference between these two calculations to neglecting the anisotropic contribution to the interaction potential in the construction of the MQDT reference functions. In principle, the perturbative MQDT method of chapter 3 can further improve the agreement.

5.5 Summary

We have presented a formulation of MQDT that is able to yield ro-vibrationally resolved cross sections and rate coefficients for ultracold molecular collisions, including chemical reactions. MQDT provided an accuracy comparable to the FCC calculations with far less computational cost. The method has made use of the close-coupling approach but has restricted it to the complex short-range region, where the chemically relevant physics occurs. We have described the long-range physics using the MQDT formalism of chapter 2. We have illustrated the usefulness and robustness of the method by applying it to the benchmark collision $H_2 + H_2$ and to the benchmark chemical reaction $D + H_2 \rightarrow HD + H$. References [87] and [88] show many more results, which all have a comparable accuracy to the results in this chapter.

Chapter 6

Conclusion

As far back as the 4th century BC, adding defects to simple models has greatly aided our understanding of complex physical phenomena. In particular, multichannel quantum defect theory (MQDT) has greatly simplified the study of complex atomic and molecular collisions. MQDT uses simple solutions to accurately describe the long-range interactions that govern many crucial aspects of these collisions. Although these simple solutions are not accurate at short range, MQDT accurately describes the short-range interactions in terms of quantum defects and matches the two regions together. This procedure generates extremely rapid and accurate scattering calculations because a single calculation of the quantum defects can accurately describe the short-range physics over a large range of collision energy and magnetic fields in many cases. MQDT has seen a particularly fruitful application to cold collisions, drastically increasing the numerical efficiency of scattering calculations and aiding the characterization of Fano-Feshbach resonances.

In this thesis, we have described a version of MQDT that is easy to implement and that accurately describes scattering calculations, gaining both numerical efficiency and conceptual insights over other types of calculations. We have defined a standardization of MQDT that allows the long-range QDT parameters to be independent of the short-range interactions, and our unique standardization is able to produce numerical reference wave functions that retain their linear independence at long range, even under centrifugal barriers described by high partial waves. Using these reference wave functions, we were able to calculate QDT parameters that are smooth in energy. Simple power laws described all of these parameters at ultracold energies, and we derived analytic

expressions for these parameters in the threshold regime for potentials dominated by $-C_6/R^6$ at long range. We have also extended MQDT to incorporate long-range anisotropic interactions that are typically ignored in applications of MQDT. To accomplish this, we used a unique distorted wave approximation to generate a perturbed short-range K-matrix that is weakly dependent on energy and field.

We have successfully applied MQDT to the collisions of $^{40}\mathrm{K} + {}^{85}\mathrm{Rb}$ and $^{133}\mathrm{Li} + {}^{6}\mathrm{Cs}$, including non-zero partial waves. We used the efficiency of MQDT to locate and characterize many Fano-Feshbach resonances in these systems. We also explored the ability of the perturbative MQDT method to incorporate the effects of strong magnetic dipole-dipole interactions. We used this method to describe a particular Fano-Feshbach resonance in the ultracold scattering of potassium atoms with an artificially enhanced dipole-dipole interaction. This method achieved sub-G accuracy in the position of this resonance through the entire range of atomic dipole strengths, while retaining the numerical efficiency of the zeroth-order MQDT calculation.

We have provided the modifications to MQDT that molecular scattering and cold chemistry require. We have presented a formulation of MQDT that is able to yield ro-vibrationally resolved cross sections and rate coefficients for ultracold molecular collisions, including chemical reactions. As an example, we applied this extension of MQDT to the benchmark collision $H_2 + H_2$ and the benchmark chemical reaction $D + H_2 \rightarrow HD + H$. MQDT produced accurate results from the interpolation of an energy-smooth K^{sr} in both cases.

In the near future, we plan to apply MQDT to much more exotic atomic and molecular collisions than these example problems. One possible limitation of this method is that K^{sr} may contain resonances from ro-vibrational channels that are locally open at short range and become closed at separations smaller than the matching radius S_{m} [39]. We did not encounter these resonances in our studies of $H_2 + H_2$ and $D + H_2$, which have shallow potential wells. Our immediate goal is to apply MQDT to the benchmark chemical reaction $F + H_2$, including electronic spin states, nuclear spin states, and an external magnetic field. Similar to our study of alkali-atom collisions, our extension of MQDT to molecular collisions may quickly and accurately describe a

whole forest of Fano-Feshbach resonances over a large range of energy and field.

Bibliography

[1] Plato. Plato: Complete Works. Hackett Publishing Company, 1997.

[2] G. E. R. Lloyd. Early Greek Science: Thales to Aristotle. Chatto and Windus, 1974.

[3] T. Bunn. Homocentric spheres: What Eudoxus and Aristotle thought about planetary motion. Web, May 2015. https://facultystaff.richmond.edu/∼ebunn/homocentric/.

[4] J. T. Cushing. Philosophical Concepts in Physics. Cambridge University Press, 1998.

[5] H. Kragh. Niels Bohr and the Quantum Atom: The Bohr Model of Atomic Structure 1913–1925. Oxford Scholarship Online, 2012.

[6] E. Schrödinger. Versuch zur modellmassigen deutung des terms der scharfen nebenserien. Z. Phys., 4:347354, 1921.

[7] N. Bohr. The spectra of helium and hydrogen. Nature, 92:231–2, 1913.

[8] N. Bohr. On the quantum theory of radiaton and the structure of the atom. Phil. Mag., 30:394–415, 1915.

[9] E. Rutherford. The scattering of α and β particles by matter and the structure of the atom. Phil. Mag., 21:669–688, 1911.

[10] N. Bohr and D. Coster. Röntegenspektren and periodisches system der elemente. Z. Phys., 12:342–374, 1923.

[11] A. R. P. Rau and M. Inokuti. The quantum defect: Early history and recent developments. Am. J. Phys., 65:221, 1997.

[12] E. Schrödinger. Die wasserstoffähnlichen spektren vom standpunkte der polarisierbarkeit des atomrumpfes. Ann. Phys., 77:43–70, 1925.

[13] D. R. Hartree. The wave mechanics of an atom with a non-Coulomb central field. Part III: Term values and intensitites in series in optical spectra. Proc. Camb. Phil. Soc., 24:426, 1928.

[14] D. R. Bates and A. Damgaard. The calculation of the abolute strengths of spectral lines. Phil. Trans. R. Soc. A, 242:101, 1949.

[15] A. Burgess and M. J. Seaton. A general formula for the calculation of atomic photoionization cross sections. Mon. Not. R. Astron. Soc., 120:121, 1960.

[16] M. Gailitis. Sov. Phys. JETP, 17:1328, 1963.

[17] F. S. Ham. The quantum defect method. Solid State Phys., 1:127, 1955.

[18] M. J. Seaton. Quantum defect theory. Rep. Prog. Phys., 46:167, 1983.

[19] U. Fano and A. R. P. Rau. Atomic Collisions and Spectra. Orlando: Academic Press, 1986.

[20] O. K. Rice. Predissociation and the crossing of molecular potential energy curves. J. Chem. Phys., 1:375–389, 1933.

[21] U. Fano. On the absorption spectrum of noble gases at the arc spectrum limit. arXiv:cond-mat/0502210 [cond-mat.other], 2005.

[22] U. Fano. Effects of configuration interaction on intensities and phase shifts. Phys. Rev., 124:1866–1878, 1961.

[23] H. Feshbach. A unified theory of nuclear reactions. II. Ann. Phys., 19:287–313, 1962.

[24] U. Fano. Quantum defect theory of l uncoupling in H_2 as an example of channel-interaction treatment. Phys. Rev. A, 2:353, 1970.

[25] U. Fano. Unified treatment of perturbed series, continuous spectra and collisions. J. Opt. Soc., 65:979, 1975.

[26] Ch. Jungen and O. Atabek. Rovibronic interactions in the photoabsorption spectrum of molecular hydrogen and deuterium: An application of multichannel quantum defect methods. J. Chem. Phys., 66:5584–5609, 1977.

[27] C. H. Greene, U. Fano, and G. Strinati. General form of the quantum-defect theory. Phys. Rev. A, 19:1485–1509, 1979.

[28] C. H. Greene, A. R. P. Rau, and U. Fano. General form of the quantum-defect theory. II. Phys. Rev. A, 26:2441–2459, 1982.

[29] F. H. Mies. A multichannel quantum defect analysis of diatomic predissociation and inelastic atomic scattering. J. Chem. Phys., 80:2514, 1984.

[30] A. R. P. Rau. A unified view of collisions and spectra. In J. S. Briggs, H. Kleinpoppen, and H. O. Lutz, editors, Fundamental Processes of Atomic Dynamics, volume 181 of NATO ASI Series, pages 51–77. Springer US, 1988.

[31] Ch. Jungen. Quantum defect theory for molecules. In J. S. Briggs, H. Kleinpoppen, and H. O. Lutz, editors, Fundamental Processes of Atomic Dynamics, volume 181 of NATO ASI Series, pages 79–103. Springer US, 1988.

[32] C. H. Greene. Variational calculation of channel interaction parameters. In J. S. Briggs, H. Kleinpoppen, and H. O. Lutz, editors, Fundamental Processes of Atomic Dynamics, volume 181 of NATO ASI Series, pages 105–127. Springer US, 1988.

[33] A. R. P. Rau. Relationships between the parameters of quantum-defect theory. Phys. Rev. A, 38:2255, 1988.

[34] J. P. Burke, C. H. Greene, and J. L. Bohn. Multichannel cold collisions: Simple dependences on energy and magnetic field. Phys. Rev. Lett., 81:3355, 1998.

[35] I. Fourré and M. Raoult. Application of generalized quantum defect theory to van der Waals complex bound state calculations. J. Chem. Phys., 101:8709, 1994.

[36] Bo Gao. Quantum-defect theory of atomic collisions and molecular vibration spectra. Phys. Rev. A, 58:4222, 1998.

[37] F. H. Mies and M. Raoult. Analysis of threshold effects in ultracold atomic collisions. Phys. Rev. A, 62:012708, 2000.

[38] M. Raoult and F. H. Mies. Feshbach resonance in atomic binary collisions in the Wigner threshold law regime. Phys. Rev. A, 70:012710, 2004.

[39] J. F. E. Croft, A. O. G. Wallis, J. M. Hutson, and P. S. Julienne. Multichannel quantum defect theory for cold molecular collisions. Phys. Rev. A, 84:042703, 2011.

[40] L. Carr and J. Ye. Focus on cold and ultracold molecules. New J. Phys., 11:055009, 2009.

[41] G. Quéméner, J.-M. Launay, and P. Honvault. Ultracold collisions between Li atoms and Li_2 diatoms in high vibrational states. Phys. Rev. A, 75:050701, 2007.

[42] Bo Gao, E. Tiesinga, C. J. Williams, and P. S. Julienne. Multichannel quantum-defect theory for slow atomic collisions. Phys. Rev. A, 72:042719, 2005.

[43] K. Willner and F. A. Gianturco. Low-energy expansion of the Jost function for long-range potentials. Phys. Rev. A, 74:052715, 2006.

[44] Bo Gao. General form of the quantum-defect theory for $-1/r^\alpha$ type of potentials with $\alpha > 2$. Phys. Rev. A, 78:012702, 2008.

[45] T. M. Hanna, E. Tiesinga, and P. S. Julienne. Prediction of Feshbach resonances from three input parameters. Phys. Rev. A, 79(4):040701, 2009.

[46] P. S. Julienne. Ultracold molecules from ultracold atoms: A case study with the KRb molecule. Faraday Discuss., 142:361, 2009.

[47] Z. Idziaszek and P. S. Julienne. Universal rate constants for reactive collisions of ultracold molecules. Phys. Rev. Lett., 104:113202, 2010.

[48] G. Quéméner and J. L. Bohn. Strong dependence of ultracold chemical rates on electric dipole moments. Phys. Rev. A, 81:022702, 2010.

[49] Z. Idziaszek, G. Quéméner, J. L. Bohn, and P. S. Julienne. Simple quantum model of ultracold polar molecule collisions. Phys. Rev. A, 82:020703, 2010.

[50] T.-O. Müller, A. Kaiser, and H. Friedrich. s-wave scattering for deep potentials with attractive tails falling off faster than $-1/r^2$. Phys. Rev. A, 84:032701, 2011.

[51] E. Wille, F. M. Spiegelhalder, G. Kerner, D. Naik, A. Trenkwalder, G. Hendl, F. Schreck, R. Grimm, T. G. Tiecke, J. T. M. Walraven, S. J. J. M. F. Kokkelmans, E. Tiesinga, and P. S. Julienne. Exploring an ultracold Fermi-Fermi mixture: Interspecies Feshbach resonances and scattering properties of ^{6}Li and ^{40}K. Phys. Rev. Lett., 100:053201, 2008.

[52] T. G. Tiecke, M. R. Goosen, A. Ludewig, S. D. Gensemer, S. Kraft, S. J. J. M. F. Kokkelmans, and J. T. M. Walraven. Broad Feshbach resonance in the ^{6}Li–^{40}K mixture. Phys. Rev. Lett., 104:053202, 2010.

[53] T. G. Tiecke, M. R. Goosen, J. T. M. Walraven, and S. J. J. M. F. Kokkelmans. Asymptotic-bound-state model for Feshbach resonances. Phys. Rev. A, 82:042712, 2010.

[54] B. P. Ruzic, C. H. Greene, and J. L. Bohn. Quantum defect theory for high-partial-wave cold collisions. Phys. Rev. A, 87:032706, 2013.

[55] S.-Y. Lee and J. C. Light. On the quantum momentum method for the exact solution of separable multiple well bound state and scattering problems. Chem. Phys. Lett., 25:435–438, 1974.

[56] E. Y. Sidky. The phase-amplitude method of solving the wave equation. Phys. Essays, 13:408, 2000.

[57] B. R. Johnson. The multichannel log-derivative method for scattering calculations. J. Comput. Phys., 13:445–449, 1973.

[58] F. W. J. Oliver, D. W. Lozier, R. F. Boisevert, and C. W. Clark. NIST Handbook of Mathematical Functions. Cambridge University Press, 2010.

[59] A. Pashov, O. Docenko, M. Tamanis, R. Ferber, H. Knöckel, and E. Tiemann. Coupling of the $X\,^1\Sigma^+$ and $a\,^3\Sigma^+$ states of KRb. Phys. Rev. A, 76:022511, 2007.

[60] G. F. Gribakin and V. V. Flambaum. Calculation of the scattering length in atomic collisions using the semiclassical approximation. Phys. Rev. A, 48:546–553, 1993.

[61] Bo Gao. Solutions of the Schrödinger equation for an attractive $1/r^6$ potential. Phys. Rev. A, 58:1728–1734, 1998.

[62] Bo Gao. Binding energy and scattering length for diatomic systems. J. Phys. B, 37:4273, 2004.

[63] Bo Gao. Analytic description of atomic interaction at ultracold temperatures: The case of a single channel. Phys. Rev. A, 80:012702, 2009.

[64] J. R. Taylor. Scattering Theory: The Quantum Theory of Nonrelativistic Collisions. Dover Publications, Inc., 2006.

[65] L. D. Landau and E. M. Lifshitz. Quantum Mechanics Non-Relativistic Theory, Third Edition: Volume 3. Reed Educational and Professional Publishing Ltd., 1977.

[66] N. R. Badnell and M. J. Seaton. Quantum defect theory with long-range multipole potentials. J. Phys. B, 32:3955, 1999.

[67] T. W. Gorczyca and N. R. Badnell. Quantum defect theory with deeply closed channels. J. Phys. B, 33:2511, 2000.

[68] L. Rosenberg. Distorted-wave reaction theory with long-range multipole potentials. Phys. Rev. A, 63:032714, 2001.

[69] P. S. Julienne and F. H. Mies. A multichannel distorted-wave approximation. J. Phys. B, 14:4335–4347, 1981.

[70] J. L. Bohn and P. S. Julienne. Semianalytic theory of laser-assisted resonant cold collisions. Phys. Rev. A, 60:414, 1999.

[71] F. Calogero. Variable phase approach to potential scattering. Academic Press, New York, 1967.

[72] R. Pires, M. Repp, J. Ulmanis, E. D. Kuhnle, M. Weidemüller, T. G. Tiecke, C. H. Greene, B. P. Ruzic, J. L. Bohn, and E. Tiemann. Analyzing Feshbach resonances: A ^{6}Li–^{133}Cs case study. Phys. Rev. A, 90:012710, 2014.

[73] A. Simoni, M. Zaccanti, C. D'Errico, M. Fattori, G. Roati, M. Inguscio, and G. Modugno. Near-threshold model for ultracold KRb dimers from interisotope Feshbach spectroscopy. Phys. Rev. A, 77:052705, 2008.

[74] M. Zaccanti, C. D'Errico, F. Ferlaino, G. Roati, M. Inguscio, and G. Modugno. Control of the interaction in a Fermi-Bose mixture. Phys. Rev. A, 74:041605, 2006.

[75] R. S. Bloom, M.-G. Hu, T. D. Cumby, and D. S. Jin. Tests of universal three-body physics in an ultracold Bose-Fermi mixture. Phys. Rev. Lett., 111:105301, 2013.

[76] Y. V. Suleimanov and R. V. Krems. Efficient numerical method for locating Feshbach resonances of ultracold molecules in external fields. J. Chem. Phys., 134:014101, 2011.

[77] M. Repp, R. Pires, J. Ulmanis, R. Heck, E. D. Kuhnle, M. Weidemüller, and E. Tiemann. Observation of interspecies ^{6}Li–^{133}Cs Feshbach resonances. Phys. Rev. A, 87:010701, 2013.

[78] P. Staanum, A. Pashov, H. Knöckel, and E. Tiemann. $X\ ^{1}\Sigma^{+}$ and $a\ ^{3}\Sigma^{+}$ states of LiCs studied by Fourier-transform spectroscopy. Phys. Rev. A, 75:042513, 2007.

[79] J. M. Hutson. Feshbach resonances in ultracold atomic and molecular collisions: Threshold behaviour and suppression of poles in scattering lengths. New J. Phys., 9:152, 2007.

[80] C. Amiot, J. Vergés, and C. E. Fellows. The long-range potential of the K_2 $X\ ^{1}\Sigma_{g}^{+}$ ground electronic state up to 15 Å. J. Chem. Phys., 103:3350–3356, 1995.

[81] L. Li, A. M. Lyyra, W. T. Luh, and W. C. Stwalley. Observation of the $^{39}K_2$ $a\ ^{3}\Sigma_{u}^{+}$ state by perturbation facilitated optical-optical double resonance resolved fluorescence spectroscopy. J. Chem. Phys., 93:8452–8463, 1990.

[82] W. T. Zemke, C.C. Tsai, and W. C. Stwalley. Analysis of long range dispersion and exchange interactions between two K atoms. J. Chem. Phys., 101:10382–10387, 1994.

[83] G. Zhao, W. T. Zemke, J. T. Kim, B. Ji, H. Wang, J. T. Bahns, W. C. Stwalley, L. Li, A. M. Lyyra, and C. Amiot. New measurements of the $a\ ^{3}\Sigma_{u}^{+}$ state of K_2 and improved analysis of long-range dispersion and exchange interactions between two K atoms. J. Chem. Phys., 105:7976–7985, 1996.

[84] C. A. Regal, C. Ticknor, J. L. Bohn, and D. S. Jin. Tuning p-wave interactions in an ultracold Fermi gas of atoms. Phys. Rev. Lett., 90:053201, 2003.

[85] M. Marinescu, H. R. Sadeghpour, and A. Dalgarno. Dispersion coefficients for alkali-metal dimers. Phys. Rev. A, 49:982, 1994.

[86] J. P. Gaebler. Photoemission Spectroscopy of a Strongly Interacting Fermi Gas. PhD thesis, University of Colorado, Boulder, 2010.

[87] J. Hazra, B. P. Ruzic, N. Balakrishnan, and J. L. Bohn. Multichannel quantum defect theory for rovibrational transitions in ultracold molecule-molecule collisions. Phys. Rev. A, 90:032711, 2014.

[88] J. Hazra, B. P. Ruzic, J. L. Bohn, and N. Balakrishnan. Quantum defect theory for cold chemistry with product-quantum-state resolution. Phys. Rev. A, 90:062703, 2014.

[89] R. V. Krems. Molecules near absolute zero and external field control of atomic and molecular dynamics. Int. Rev. Phys. Chem., 24:99–118, 2005.

[90] P. F. Weck and N. Balakrishnan. Importance of long-range interactions in chemical reactions at cold and ultracold temperatures. Int. Rev. Phys. Chem., 25:283, 2006.

[91] J. M. Hutson and P. Soldán. Molecule formation in ultracold atomic gases. Int. Rev. Phys. Chem., 25:497–526, 2006.

[92] J. M. Hutson and P. Soldán. Molecular collisions in ultracold atomic gases. Int. Rev. Phys. Chem., 26:1–28, 2007.

[93] R. V. Krems. Cold controlled chemistry. Phys. Chem. Chem. Phys., 10:4079, 2008.

[94] K.-K. Ni, S. Ospelkaus, M. H. G. de Miranda, A. Pe'er, B. Neyenhuis, J. J. Zirbel, S. Kotochigova, P. S. Julienne, D. S. Jin, and J. Ye. A high phase-space-density gas of polar molecules. Science, 322:231, 2008.

[95] K.-K. Ni, S. Ospelkaus, D. Wang, G. Quéméner, B. Neyenhuis, M. H. G. de Miranda, J. L. Bohn, J. Ye, and D. S. Jin. Dipolar collisions of polar molecules in the quantum regime. Nature, 464:1324, 2010.

[96] N. Balakrishnan and A. Dalgarno. Chemistry at ultracold temperatures. Chem. Phys. Lett., 341:652–656, 2001.

[97] P. Soldán, M. T. Cvitaš, J. M. Hutson, P. Honvault, and J.-M. Launay. Quantum dynamics of ultracold $Na + Na_2$ collisions. Phys. Rev. Lett., 89:153201, 2002.

[98] G. Quéméner, P. Honvault, and J.-M. Launay. Sensitivity of the dynamics of $Na + Na_2$ collisions on the three-body interaction at ultralow energies. Eur. Phys. J. D, 30:201, 2004.

[99] M. T. Cvitaš, P. Soldán, J. M. Hutson, P. Honvault, and J.-M. Launay. Ultracold collisions involving heteronuclear alkali metal dimers. Phys. Rev. Lett., 94:200402, 2005.

[100] J. C. Juanes-Marcos, G. Quéméner, B. K. Kendrick, and N. Balakrishnan. Ultracold collisions and reactions of vibrationally excited OH radicals with oxygen atoms. Phys. Chem. Chem. Phys., 13:19067–19076, 2011.

[101] G. B. Pradhan, N. Balakrishnan, and B. K. Kendrick. Ultracold collisions of $O(^1D)$ and H_2: The effects of H_2 vibrational excitation on the production of vibrationally and rotationally excited OH. J. Chem. Phys., 138:164310, 2013.

[102] T. V. Tscherbul and R. V. Krems. Quantum theory of chemical reactions in the presence of electromagnetic fields. J. Chem. Phys., 129:034112, 2008.

[103] J. F. E. Croft, J. M. Hutson, and P. S. Julienne. Optimized multichannel quantum defect theory for cold molecular collisions. Phys. Rev. A, 86:022711, 2012.

[104] Bo Gao. Universal model for exoergic bimolecular reactions and inelastic processes. Phys. Rev. Lett., 105:263203, 2010.

[105] G.-R. Wang, T. Xie, Y. Huang, W. Zhang, and S.-L. Cong. Quantum defect theory for the van der Waals plus dipole-dipole interaction. Phys. Rev. A, 86:062704, 2012.

[106] G. Quéméner, N. Balakrishnan, and R. V. Krems. Vibrational energy transfer in ultracold molecule-molecule collisions. Phys. Rev. A, 77:030704, 2008.

[107] L. M. Delves. Tertiary and general-order collisions. Nuc. Phys., 9:391–399, 1958.

[108] R. T. Pack and G. A. Parker. Quantum reactive scattering in three dimensions using hyperspherical (APH) coordinates. Theory. J. Chem. Phys., 87:3888, 1987.

[109] M. A. Woodbury. Inverting modified matrices. MR, 12:4, 1950.

[110] S. L. Mielke, B. C. Garrett, and K. A. Peterson. A hierarchical family of global analytic Born-Oppenheimer potential energy surfaces for the $H + H_2$ reaction ranging in quality from double-zeta to the complete basis set limit. J. Chem. Phys., 116:4142–4161, 2002.

Appendix A

Derivation of the Perturbed Short-range K-matrix

In this appendix, we derive a first-order approximation to the perturbed short-range K-matrix $K^{\mathrm{sr}'}$ that only depends on convergent integrals. We accomplish this by deriving an approximate set of equations for the constants C' and $\tilde{K}'$ that represent $\hat{F}(R)$ at R_{e}. Although this set of equations depends on exponentially divergent integrals, we show that $\tilde{K}'$, from which we derive all scattering observables, only depends on convergent integrals to first order in $V'(R)$. In order to arrive at $K^{\mathrm{sr}'}$, we approximate the behavior of $\hat{F}(R)$ at R_{e} by neglecting the exponentially divergent integrals that do not contribute to $\tilde{K}'$. We use the resulting expression for $\hat{F}(R)$ to derive a first-order expression for $K^{\mathrm{sr}'}$.

The set of equations (3.15 - 3.16) define C' and $\tilde{K}'$,

$$\hat{F}_{\mathrm{P}}(R) = \hat{f}_{\mathrm{P}}(R) - \hat{g}_{\mathrm{P}}(R)\tilde{K}' \quad \text{at } R = R_{\mathrm{e}} \tag{A.1a}$$

$$\hat{F}_{\mathrm{Q}}(R) = \left(\hat{f}_{\mathrm{Q}}(R) + \hat{g}_{\mathrm{Q}}(R)\cot\gamma\right) C' \quad \text{at } R = R_{\mathrm{e}} \tag{A.1b}$$

$$= \chi_{\mathrm{Q}}^{-}(R)\csc\gamma C' \quad \text{at } R = R_{\mathrm{e}}. \tag{A.1c}$$

We derive expressions for C' and $\tilde{K}'$ by finding an approximation to $\hat{F}(R)$ at R_{e} and setting it equal to the representation of $\hat{F}(R)$ in the set of equations (A.1). To this end, we can use equation (3.22)

to approximate the behavior of $\hat{F}(R)$ at $R_{\rm e}$,

$$\begin{aligned}\hat{F}(R) \approx &\left(\hat{f}(R)I(R_{\rm t_1}) - \hat{g}(R)J(R_{\rm t_1})\right)B' \\ &- \hat{f}(R)\int_{R_{\rm t_1}}^{R_{\rm e}} \hat{g}(R')V'(R')\left(\hat{f}(R')I(R_{\rm e}) - \hat{g}(R')J(R_{\rm e})\right)B'\mathrm{d}R' \\ &+ \hat{g}(R)\int_{R_{\rm t_1}}^{R_{\rm e}} \hat{f}(R')V'(R')\left(\hat{f}(R')I(R_{\rm e}) - \hat{g}(R')J(R_{\rm e})\right)B'\mathrm{d}R' \quad \text{at } R = R_{\rm e}. \end{aligned} \tag{A.2}$$

However, because $\hat{f}(R)$ and $\hat{g}(R)$ exponentially diverge in the closed channels beyond their outer classical turning points, some of the integrals in equation (A.2) exponentially diverge with increasing $R_{\rm e}$. Hence, using this equation to approximate the behavior of $\hat{F}(R)$ at $R_{\rm e}$ may lead to values of B', C', and $\tilde{K}'$ that diverge with increasing $R_{\rm e}$ as well.

In order to isolate the divergences in equation (A.2), we define a new set of linearly independent closed-channel reference wave functions $\chi^-(R)$ and $\chi^+(R)$. We rewrite equation (2.16) that defines $\chi^-(R)$,

$$\chi_i^-(R) = \hat{f}_i(R)\sin\gamma_i + \hat{g}_i(R)\cos\gamma_i \xrightarrow{R\to\infty} \propto e^{-\kappa_i R}. \tag{A.3}$$

We force $\chi^+(R)$ to be linearly independent from $\chi^-(R)$ by defining $\chi^+(R)$ as the following linear combination of $\hat{f}(R)$ and $\hat{g}(R)$ in each closed channel i,

$$\chi_i^+(R) = \hat{g}_i(R)\sin\gamma_i - \hat{f}_i(R)\cos\gamma_i. \tag{A.4}$$

Unlike $\chi^-(R)$, which exponentially decays in the limit $R \to \infty$, the reference wave function $\chi^+(R)$ exponentially diverges in this limit. The Wronskian of this new set of reference wave functions is equal to one in each closed channel i, $\mathcal{W}\left(\chi_i^-(R), \chi_i^+(R)\right) = 1$.

Repartitioning all matrices into open (P) channels and closed (Q) channels, $M(R)$ has the following form,

$$M_{\rm XY}(R) = \hat{f}_{\rm X}(R)I_{\rm XY}(R) - \hat{g}_{\rm X}(R)J_{\rm XY}(R), \tag{A.5}$$

where the subscripts X and Y stand for either P or Q. In terms of $\chi_{\rm Q}^-(R)$ and $\chi_{\rm Q}^+(R)$, we represent $M_{\rm QY}(R)$ by the coefficients $X_{\rm QY}(R)$ and $Y_{\rm QY}(R)$,

$$M_{\rm QY}(R) = \chi_{\rm Q}^-(R)X_{\rm QY}(R) - \chi_{\rm Q}^+(R)Y_{\rm QY}(R). \tag{A.6}$$

The matrix $\chi^+_{\rm Q}(R)$ is the $N_{\rm c} \times N_{\rm c}$ diagonal matrix whose diagonal elements consist of the closed channel wave function $\chi^+(R)$. Using equations (A.3) and (A.4) that define $\chi^-(R)$ and $\chi^+(R)$ in terms of $\hat{f}(R)$ and $\hat{g}(R)$, we relate $X_{\rm QY}(R)$ and $Y_{\rm QY}(R)$ to $I_{\rm QY}(R)$ and $J_{\rm QY}(R)$ by,

$$X_{\rm QY}(R) = \sin\gamma I_{\rm QY}(R) - \cos\gamma J_{\rm QY}(R) \tag{A.7a}$$

$$Y_{\rm QY}(R) = \cos\gamma I_{\rm QY}(R) + \sin\gamma J_{\rm QY}(R), \tag{A.7b}$$

with inverse,

$$I_{\rm QY}(R) = \sin\gamma X_{\rm QY}(R) + \cos\gamma Y_{\rm QY}(R) \tag{A.8a}$$

$$J_{\rm QY}(R) = \sin\gamma Y_{\rm QY}(R) - \cos\gamma X_{\rm QY}(R). \tag{A.8b}$$

We substitute the expression for $M_{\rm PY}(R)$ in equation (A.5) and the expression for $M_{\rm QY}(R)$ in equation (A.6) into the open channels and closed channels of the transformation $\hat{F}(R) = M(R)B'$, respectively,

$$\hat{F}_{\rm P}(R) = \hat{f}_{\rm P}(R)\left(I_{\rm PP}(R_{\rm e})B'_{\rm P} + I_{\rm PQ}(R_{\rm e})B'_{\rm Q}\right) - \hat{g}_{\rm P}(R)\left(J_{\rm PP}(R_{\rm e})B'_{\rm P} + J_{\rm PQ}(R_{\rm e})B'_{\rm Q}\right) \tag{A.9a}$$

$$\hat{F}_{\rm Q}(R) = \chi^-_{\rm Q}(R)\left(X_{\rm QP}(R_{\rm e})B'_{\rm P} + X_{\rm QQ}(R_{\rm e})B'_{\rm Q}\right) - \chi^+_{\rm Q}(R)\left(Y_{\rm QP}(R_{\rm e})B'_{\rm P} + Y_{\rm QQ}(R_{\rm e})B'_{\rm Q}\right). \tag{A.9b}$$

This representation of $\hat{F}(R)$ at $R_{\rm e}$ clearly identifies $X_{\rm QP}(R_{\rm e})B'_{\rm P} + X_{\rm QQ}(R_{\rm e})B'_{\rm Q}$ as the coefficient in front of the exponentially decaying reference wave function $\chi^-_{\rm Q}(R)$. This representation also identifies $Y_{\rm QP}(R_{\rm e})B'_{\rm P} + Y_{\rm QQ}(R_{\rm e})B'_{\rm Q}$ as the coefficient in front of the exponentially growing reference wave function $\chi^+_{\rm Q}(R)$. We are, therefore, in a position to zero the latter coefficient so as to preserve acceptable boundary conditions on $\hat{F}(R)$ at $R_{\rm e}$,

$$Y_{\rm QP}(R_{\rm e})B'_{\rm P} + Y_{\rm QQ}(R_{\rm e})B'_{\rm Q} = 0. \tag{A.10}$$

Repartitioning equation (A.2) into open channels and closed channels, produces the following approximations for the coefficients in front of $\hat{f}_{\rm P}(R)$, $\hat{g}_{\rm P}(R)$, $\chi^-_{\rm Q}(R)$, and $\chi^+_{\rm Q}(R)$ in the set of

equations (A.9),

$$\begin{aligned} I_{\mathrm{PP}}(R_{\mathrm{e}})B'_{\mathrm{P}} + I_{\mathrm{PQ}}(R_{\mathrm{e}})B'_{\mathrm{Q}} \approx & I_{\mathrm{PP}}(R_{\mathrm{t}_1})B'_{\mathrm{P}} + I_{\mathrm{PQ}}(R_{\mathrm{t}_1})B'_{\mathrm{Q}} \\ & - \int_{R_{\mathrm{t}_1}}^{R_{\mathrm{e}}} \hat{g}_{\mathrm{P}}(R')V'_{\mathrm{PP}}(R')\hat{f}_{\mathrm{P}}(R') \left(I_{\mathrm{PP}}(R_{\mathrm{e}})B'_{\mathrm{P}} + I_{\mathrm{PQ}}(R_{\mathrm{e}})B'_{\mathrm{Q}}\right) \mathrm{d}R' \\ & + \int_{R_{\mathrm{t}_1}}^{R_{\mathrm{e}}} \hat{g}_{\mathrm{P}}(R')V'_{\mathrm{PP}}(R')\hat{g}_{\mathrm{P}}(R') \left(J_{\mathrm{PP}}(R_{\mathrm{e}})B'_{\mathrm{P}} + J_{\mathrm{PQ}}(R_{\mathrm{e}})B'_{\mathrm{Q}}\right) \mathrm{d}R' \\ & - \int_{R_{\mathrm{t}_1}}^{R_{\mathrm{e}}} \hat{g}_{\mathrm{P}}(R')V'_{\mathrm{PQ}}(R')\chi^{-}_{\mathrm{Q}}(R') \left(X_{\mathrm{QP}}(R_{\mathrm{e}})B'_{\mathrm{P}} + X_{\mathrm{QQ}}(R_{\mathrm{e}})B'_{\mathrm{Q}}\right) \mathrm{d}R' \end{aligned} \tag{A.11a}$$

$$\begin{aligned} J_{\mathrm{PP}}(R_{\mathrm{e}})B'_{\mathrm{P}} + J_{\mathrm{PQ}}(R_{\mathrm{e}})B'_{\mathrm{Q}} \approx & J_{\mathrm{PP}}(R_{\mathrm{t}_1})B'_{\mathrm{P}} + J_{\mathrm{PQ}}(R_{\mathrm{t}_1})B'_{\mathrm{Q}} \\ & - \int_{R_{\mathrm{t}_1}}^{R_{\mathrm{e}}} \hat{f}_{\mathrm{P}}(R')V'_{\mathrm{PP}}(R')\hat{f}_{\mathrm{P}}(R') \left(I_{\mathrm{PP}}(R_{\mathrm{e}})B'_{\mathrm{P}} + I_{\mathrm{PQ}}(R_{\mathrm{e}})B'_{\mathrm{Q}}\right) \mathrm{d}R' \\ & + \int_{R_{\mathrm{t}_1}}^{R_{\mathrm{e}}} \hat{f}_{\mathrm{P}}(R')V'_{\mathrm{PP}}(R')\hat{g}_{\mathrm{P}}(R') \left(J_{\mathrm{PP}}(R_{\mathrm{e}})B'_{\mathrm{P}} + J_{\mathrm{PQ}}(R_{\mathrm{e}})B'_{\mathrm{Q}}\right) \mathrm{d}R' \\ & - \int_{R_{\mathrm{t}_1}}^{R_{\mathrm{e}}} \hat{f}_{\mathrm{P}}(R')V'_{\mathrm{PQ}}(R')\chi^{-}_{\mathrm{Q}}(R') \left(X_{\mathrm{QP}}(R_{\mathrm{e}})B'_{\mathrm{P}} + X_{\mathrm{QQ}}(R_{\mathrm{e}})B'_{\mathrm{Q}}\right) \mathrm{d}R' \end{aligned} \tag{A.11b}$$

$$\begin{aligned} X_{\mathrm{QP}}(R_{\mathrm{e}})B'_{\mathrm{P}} + X_{\mathrm{QQ}}(R_{\mathrm{e}})B'_{\mathrm{Q}} \approx & X_{\mathrm{QP}}(R_{\mathrm{t}_1})B'_{\mathrm{P}} + X_{\mathrm{QQ}}(R_{\mathrm{t}_1})B'_{\mathrm{Q}} \\ & - \int_{R_{\mathrm{t}_1}}^{R_{\mathrm{e}}} \chi^{+}_{\mathrm{Q}}(R')V'_{\mathrm{QP}}(R')\hat{f}_{\mathrm{P}}(R') \left(I_{\mathrm{PP}}(R_{\mathrm{e}})B'_{\mathrm{P}} + I_{\mathrm{PQ}}(R_{\mathrm{e}})B'_{\mathrm{Q}}\right) \mathrm{d}R' \\ & + \int_{R_{\mathrm{t}_1}}^{R_{\mathrm{e}}} \chi^{+}_{\mathrm{Q}}(R')V'_{\mathrm{QP}}(R')\hat{g}_{\mathrm{P}}(R') \left(J_{\mathrm{PP}}(R_{\mathrm{e}})B'_{\mathrm{P}} + J_{\mathrm{PQ}}(R_{\mathrm{e}})B'_{\mathrm{Q}}\right) \mathrm{d}R' \\ & - \int_{R_{\mathrm{t}_1}}^{R_{\mathrm{e}}} \chi^{+}_{\mathrm{Q}}(R')V'_{\mathrm{QQ}}(R')\chi^{-}_{\mathrm{Q}}(R') \left(X_{\mathrm{QP}}(R_{\mathrm{e}})B'_{\mathrm{P}} + X_{\mathrm{QQ}}(R_{\mathrm{e}})B'_{\mathrm{Q}}\right) \mathrm{d}R' \end{aligned} \tag{A.11c}$$

$$\begin{aligned} Y_{\mathrm{QP}}(R_{\mathrm{e}})B'_{\mathrm{P}} + Y_{\mathrm{QQ}}(R_{\mathrm{e}})B'_{\mathrm{Q}} \approx & Y_{\mathrm{QP}}(R_{\mathrm{t}_1})B'_{\mathrm{P}} + Y_{\mathrm{QQ}}(R_{\mathrm{t}_1})B'_{\mathrm{Q}} \\ & - \int_{R_{\mathrm{t}_1}}^{R_{\mathrm{e}}} \chi^{-}_{\mathrm{Q}}(R')V'_{\mathrm{QP}}(R')\hat{f}_{\mathrm{P}}(R') \left(I_{\mathrm{PP}}(R_{\mathrm{e}})B'_{\mathrm{P}} + I_{\mathrm{PQ}}(R_{\mathrm{e}})B'_{\mathrm{Q}}\right) \mathrm{d}R' \\ & + \int_{R_{\mathrm{t}_1}}^{R_{\mathrm{e}}} \chi^{-}_{\mathrm{Q}}(R')V'_{\mathrm{QP}}(R')\hat{g}_{\mathrm{P}}(R') \left(J_{\mathrm{PP}}(R_{\mathrm{e}})B'_{\mathrm{P}} + J_{\mathrm{PQ}}(R_{\mathrm{e}})B'_{\mathrm{Q}}\right) \mathrm{d}R' \\ & - \int_{R_{\mathrm{t}_1}}^{R_{\mathrm{e}}} \chi^{-}_{\mathrm{Q}}(R')V'_{\mathrm{QQ}}(R')\chi^{-}_{\mathrm{Q}}(R') \left(X_{\mathrm{QP}}(R_{\mathrm{e}})B'_{\mathrm{P}} + X_{\mathrm{QQ}}(R_{\mathrm{e}})B'_{\mathrm{Q}}\right) \mathrm{d}R'. \end{aligned} \tag{A.11d}$$

In this equation we have used the exact relationship in equation (A.10) to zero the coefficient $Y_{\mathrm{QP}}(R_{\mathrm{e}})B'_{\mathrm{P}} + Y_{\mathrm{QQ}}(R_{\mathrm{e}})B'_{\mathrm{Q}}$ that would otherwise appear inside the integrals on the right hand side of these equations.

From the structure of equation (A.11), we deduce the following expressions for $I_{\mathrm{PY}}(R_{\mathrm{e}})$, $J_{\mathrm{PY}}(R_{\mathrm{e}})$, $X_{\mathrm{QY}}(R_{\mathrm{e}})$, and $Y_{\mathrm{QY}}(R_{\mathrm{e}})$ that form an approximation to $\hat{F}(R)$ at R_{e},

$$\begin{aligned} I_{\mathrm{PY}}(R_{\mathrm{e}}) \approx & I_{\mathrm{PY}}(R_{\mathrm{t}_1}) - \int_{R_{\mathrm{t}_1}}^{R_{\mathrm{e}}} \hat{g}_{\mathrm{P}}(R')V'_{\mathrm{PP}}(R') \left(\hat{f}_{\mathrm{P}}(R')I_{\mathrm{PY}}(R_{\mathrm{e}}) - \hat{g}_{\mathrm{P}}(R')J_{\mathrm{PY}}(R_{\mathrm{e}})\right) \mathrm{d}R' \\ & - \int_{R_{\mathrm{t}_1}}^{R_{\mathrm{e}}} \hat{g}_{\mathrm{P}}(R')V'_{\mathrm{PQ}}(R')\chi^{-}_{\mathrm{Q}}(R')X_{\mathrm{QP}}(R_{\mathrm{e}})\mathrm{d}R' \end{aligned} \tag{A.12a}$$

$$\begin{aligned} J_{\mathrm{PY}}(R_{\mathrm{e}}) \approx & J_{\mathrm{PY}}(R_{\mathrm{t}_1}) - \int_{R_{\mathrm{t}_1}}^{R_{\mathrm{e}}} \hat{f}_{\mathrm{P}}(R')V'_{\mathrm{PP}}(R') \left(\hat{f}_{\mathrm{P}}(R')I_{\mathrm{PY}}(R_{\mathrm{e}}) - \hat{g}_{\mathrm{P}}(R')J_{\mathrm{PY}}(R_{\mathrm{e}})\right) \mathrm{d}R' \\ & - \int_{R_{\mathrm{t}_1}}^{R_{\mathrm{e}}} \hat{f}_{\mathrm{P}}(R')V'_{\mathrm{PQ}}(R')\chi^{-}_{\mathrm{Q}}(R')X_{\mathrm{QP}}(R_{\mathrm{e}})\mathrm{d}R' \end{aligned} \tag{A.12b}$$

$$\begin{aligned} X_{\mathrm{QY}}(R_{\mathrm{e}}) \approx & X_{\mathrm{QY}}(R_{\mathrm{t}_1}) - \int_{R_{\mathrm{t}_1}}^{R_{\mathrm{e}}} \chi^{+}_{\mathrm{Q}}(R')V'_{\mathrm{QP}}(R') \left(\hat{f}_{\mathrm{P}}(R')I_{\mathrm{PY}}(R_{\mathrm{e}}) - \hat{g}_{\mathrm{P}}(R')J_{\mathrm{PY}}(R_{\mathrm{e}})\right) \mathrm{d}R' \\ & - \int_{R_{\mathrm{t}_1}}^{R_{\mathrm{e}}} \chi^{+}_{\mathrm{Q}}(R')V'_{\mathrm{QQ}}(R')\chi^{-}_{\mathrm{Q}}(R')X_{\mathrm{QP}}(R_{\mathrm{e}})\mathrm{d}R' \end{aligned} \tag{A.12c}$$

$$\begin{aligned} Y_{\mathrm{QY}}(R_{\mathrm{e}}) \approx & Y_{\mathrm{QY}}(R_{\mathrm{t}_1}) - \int_{R_{\mathrm{t}_1}}^{R_{\mathrm{e}}} \chi^{-}_{\mathrm{Q}}(R')V'_{\mathrm{QP}}(R') \left(\hat{f}_{\mathrm{P}}(R')I_{\mathrm{PY}}(R_{\mathrm{e}}) - \hat{g}_{\mathrm{P}}(R')J_{\mathrm{PY}}(R_{\mathrm{e}})\right) \mathrm{d}R' \\ & - \int_{R_{\mathrm{t}_1}}^{R_{\mathrm{e}}} \chi^{-}_{\mathrm{Q}}(R')V'_{\mathrm{QQ}}(R')\chi^{-}_{\mathrm{Q}}(R')X_{\mathrm{QP}}(R_{\mathrm{e}})\mathrm{d}R'. \end{aligned} \tag{A.12d}$$

The right hand side of the set of equations (A.12) includes integrals that contain the coefficients $I_{\mathrm{PY}}(R_{\mathrm{e}})$, $J_{\mathrm{PY}}(R_{\mathrm{e}})$, and $X_{\mathrm{QY}}(R_{\mathrm{e}})$, which are thus far unknown. However, these coefficients differ from their values at R_{t_1} by integrals over $V'(R)$. Therefore, using the approximations $I_{\mathrm{PY}}(R_{\mathrm{e}}) \approx I_{\mathrm{PY}}(R_{\mathrm{t}_1})$, $J_{\mathrm{PY}}(R_{\mathrm{e}}) \approx J_{\mathrm{PY}}(R_{\mathrm{t}_1})$, and $X_{\mathrm{QY}}(R_{\mathrm{e}}) \approx X_{\mathrm{QY}}(R_{\mathrm{t}_1})$ inside the integrals on the right hand side of the set of equations (A.12) is valid to order $V'(R)$. This leads to the following

relations,

$$I_{\mathrm{PY}}(R_{\mathrm{e}}) \approx I_{\mathrm{PY}}(R_{\mathrm{t}_1}) - \int_{R_{\mathrm{t}_1}}^{R_{\mathrm{e}}} \hat{g}_{\mathrm{P}}(R') V'_{\mathrm{PP}}(R') \left(\hat{f}_{\mathrm{P}}(R') I_{\mathrm{PY}}(R_{\mathrm{t}_1}) - \hat{g}_{\mathrm{P}}(R') J_{\mathrm{PY}}(R_{\mathrm{t}_1}) \right) \mathrm{d}R'$$
$$- \int_{R_{\mathrm{t}_1}}^{R_{\mathrm{e}}} \hat{g}_{\mathrm{P}}(R') V'_{\mathrm{PQ}}(R') \chi^{-}_{\mathrm{Q}}(R') X_{\mathrm{QP}}(R_{\mathrm{t}_1}) \mathrm{d}R' \tag{A.13a}$$

$$J_{\mathrm{PY}}(R_{\mathrm{e}}) \approx J_{\mathrm{PY}}(R_{\mathrm{t}_1}) - \int_{R_{\mathrm{t}_1}}^{R_{\mathrm{e}}} \hat{f}_{\mathrm{P}}(R') V'_{\mathrm{PP}}(R') \left(\hat{f}_{\mathrm{P}}(R') I_{\mathrm{PY}}(R_{\mathrm{t}_1}) - \hat{g}_{\mathrm{P}}(R') J_{\mathrm{PY}}(R_{\mathrm{t}_1}) \right) \mathrm{d}R'$$
$$- \int_{R_{\mathrm{t}_1}}^{R_{\mathrm{e}}} \hat{f}_{\mathrm{P}}(R') V'_{\mathrm{PQ}}(R') \chi^{-}_{\mathrm{Q}}(R') X_{\mathrm{QP}}(R_{\mathrm{t}_1}) \mathrm{d}R' \tag{A.13b}$$

$$X_{\mathrm{QY}}(R_{\mathrm{e}}) \approx X_{\mathrm{QY}}(R_{\mathrm{t}_1}) - \int_{R_{\mathrm{t}_1}}^{R_{\mathrm{e}}} \chi^{+}_{\mathrm{Q}}(R') V'_{\mathrm{QP}}(R') \left(\hat{f}_{\mathrm{P}}(R') I_{\mathrm{PY}}(R_{\mathrm{t}_1}) - \hat{g}_{\mathrm{P}}(R') J_{\mathrm{PY}}(R_{\mathrm{t}_1}) \right) \mathrm{d}R'$$
$$- \int_{R_{\mathrm{t}_1}}^{R_{\mathrm{e}}} \chi^{+}_{\mathrm{Q}}(R') V'_{\mathrm{QQ}}(R') \chi^{-}_{\mathrm{Q}}(R') X_{\mathrm{QP}}(R_{\mathrm{t}_1}) \mathrm{d}R' \tag{A.13c}$$

$$Y_{\mathrm{QY}}(R_{\mathrm{e}}) \approx Y_{\mathrm{QY}}(R_{\mathrm{t}_1}) - \int_{R_{\mathrm{t}_1}}^{R_{\mathrm{e}}} \chi^{-}_{\mathrm{Q}}(R') V'_{\mathrm{QP}}(R') \left(\hat{f}_{\mathrm{P}}(R') I_{\mathrm{PY}}(R_{\mathrm{t}_1}) - \hat{g}_{\mathrm{P}}(R') J_{\mathrm{PY}}(R_{\mathrm{t}_1}) \right) \mathrm{d}R'$$
$$- \int_{R_{\mathrm{t}_1}}^{R_{\mathrm{e}}} \chi^{-}_{\mathrm{Q}}(R') V'_{\mathrm{QQ}}(R') \chi^{-}_{\mathrm{Q}}(R') X_{\mathrm{QP}}(R_{\mathrm{t}_1}) \mathrm{d}R'. \tag{A.13d}$$

We equate the coefficients in front of $\hat{f}_{\mathrm{P}}(R)$ and $\hat{g}_{\mathrm{P}}(R)$ in equation (A.9a) with the corresponding coefficients in front of $\hat{f}_{\mathrm{P}}(R)$ and $\hat{g}_{\mathrm{P}}(R)$ in equation (A.1a),

$$\mathcal{I} = I_{\mathrm{PP}}(R_{\mathrm{e}}) B'_{\mathrm{P}} + I_{\mathrm{PQ}}(R_{\mathrm{e}}) B'_{\mathrm{Q}} \tag{A.14a}$$

$$-\tilde{K}' = J_{\mathrm{PP}}(R_{\mathrm{e}}) B'_{\mathrm{P}} + J_{\mathrm{PQ}}(R_{\mathrm{e}}) B'_{\mathrm{Q}}, \tag{A.14b}$$

where $\mathcal{I}$ is the $N_{\mathrm{o}} \times N_{\mathrm{o}}$ identity matrix. In a similar manner, we equate the coefficients in front of $\chi^{-}_{\mathrm{Q}}(R)$ and $\chi^{+}_{\mathrm{Q}}(R)$ in equation (A.9b) with the corresponding coefficients in front of $\chi^{-}_{\mathrm{Q}}(R)$ and $\chi^{+}_{\mathrm{Q}}(R)$ in equation (A.1c),

$$\csc\gamma C' = X_{\mathrm{QP}}(R_{\mathrm{e}}) B'_{\mathrm{P}} + X_{\mathrm{QQ}}(R_{\mathrm{e}}) B'_{\mathrm{Q}} \tag{A.15a}$$

$$0 = Y_{\mathrm{QP}}(R_{\mathrm{e}}) B'_{\mathrm{P}} + Y_{\mathrm{QQ}}(R_{\mathrm{e}}) B'_{\mathrm{Q}}. \tag{A.15b}$$

Equations (A.14) and (A.15) form an exact and complete set of equations for the constants B', C', and $\tilde{K}'$ in terms of the coefficients $I_{\mathrm{PY}}(R_{\mathrm{e}})$, $J_{\mathrm{PY}}(R_{\mathrm{e}})$, $X_{\mathrm{QY}}(R_{\mathrm{e}})$, and $Y_{\mathrm{QY}}(R_{\mathrm{e}})$. Solving the system

of equations (A.14) and (A.15) leads to the following relations,

$$B'_{\mathrm{P}} = \Big(I_{\mathrm{PP}}(R_{\mathrm{e}}) - I_{\mathrm{PQ}}(R_{\mathrm{e}})Y^{-1}_{\mathrm{QQ}}(R_{\mathrm{e}})Y_{\mathrm{QP}}(R_{\mathrm{e}})\Big)^{-1} \tag{A.16a}$$

$$B'_{\mathrm{Q}} = -\,Y^{-1}_{\mathrm{QQ}}(R_{\mathrm{e}})Y_{\mathrm{QP}}(R_{\mathrm{e}})\Big(I_{\mathrm{PP}}(R_{\mathrm{e}}) - I_{\mathrm{PQ}}(R_{\mathrm{e}})Y^{-1}_{\mathrm{QQ}}(R_{\mathrm{e}})Y_{\mathrm{QP}}(R_{\mathrm{e}})\Big)^{-1} \tag{A.16b}$$

$$\csc\gamma C' = \Big(X_{\mathrm{QP}}(R_{\mathrm{e}}) - X_{\mathrm{QQ}}(R_{\mathrm{e}})Y^{-1}_{\mathrm{QQ}}(R_{\mathrm{e}})Y_{\mathrm{QP}}(R_{\mathrm{e}})\Big)\Big(I_{\mathrm{PP}}(R_{\mathrm{e}}) - I_{\mathrm{PQ}}(R_{\mathrm{e}})Y^{-1}_{\mathrm{QQ}}(R_{\mathrm{e}})Y_{\mathrm{QP}}(R_{\mathrm{e}})\Big)^{-1} \tag{A.16c}$$

$$-\tilde{K}' = \Big(J_{\mathrm{PP}}(R_{\mathrm{e}}) - J_{\mathrm{PQ}}(R_{\mathrm{e}})Y^{-1}_{\mathrm{QQ}}(R_{\mathrm{e}})Y_{\mathrm{QP}}(R_{\mathrm{e}})\Big)\Big(I_{\mathrm{PP}}(R_{\mathrm{e}}) - I_{\mathrm{PQ}}(R_{\mathrm{e}})Y^{-1}_{\mathrm{QQ}}(R_{\mathrm{e}})Y_{\mathrm{QP}}(R_{\mathrm{e}})\Big)^{-1}. \tag{A.16d}$$

Substituting the expressions for $I_{\mathrm{PY}}(R_{\mathrm{e}})$, $J_{\mathrm{PY}}(R_{\mathrm{e}})$, $X_{\mathrm{QY}}(R_{\mathrm{e}})$, and $Y_{\mathrm{QY}}(R_{\mathrm{e}})$ from the set of equations (A.13) into the set of equations (A.16d), produces an approximation to $\tilde{K}'$ that does not depend on the integrals that contain $\chi^{+}_{\mathrm{Q}}(R')$ in equation (A.13c). Hence, we have a perturbative expression for $\tilde{K}'$, from which we derive all scattering observables, that only depends on integrals that converge with increasing R_{e}.

However, it is more useful to arrive at $K^{\mathrm{sr}'} = J(R_{\mathrm{e}})I^{-1}(R_{\mathrm{e}})$ because we expect it to be smooth in energy and field. To this end, we further approximate the representation of $\hat{F}(R)$ at R_{e} by neglecting the integrals that contain $\chi^{+}_{\mathrm{Q}}(R')$ in equation (A.13c) without affecting the value of scattering observables within this first-order approximation. We write the corresponding approximation for $X_{\mathrm{QY}}(R_{\mathrm{e}})$ below,

$$X_{\mathrm{QY}}(R_{\mathrm{e}}) \approx X_{\mathrm{QY}}(R_{\mathrm{t}_1}). \tag{A.17}$$

The approximate coefficients in equations (A.13a), (A.13b), (A.13d), and (A.17) represent $\hat{F}(R)$ at R_{e}. In order to derive $K^{\mathrm{sr}'} = J(R_{\mathrm{e}})I^{-1}(R_{\mathrm{e}})$, we translate the coefficients $X_{\mathrm{QY}}(R_{\mathrm{e}})$ and $Y_{\mathrm{QY}}(R_{\mathrm{e}})$ into $I_{\mathrm{QY}}(R_{\mathrm{e}})$ and $J_{\mathrm{QY}}(R_{\mathrm{e}})$ using the relations in the set of equations (A.8). This produces

the following set of approximations for $I(R_\mathrm{e})$ and $J(R_\mathrm{e})$ in block form,

$$\begin{aligned}
I_{\mathrm{PY}}(R_\mathrm{e}) \approx & I_{\mathrm{PY}}(R_{\mathrm{t}_1}) - \int_{R_{\mathrm{t}_1}}^{R_\mathrm{e}} \hat{g}_\mathrm{P}(R') V'_{\mathrm{PP}}(R') \left(\hat{f}_\mathrm{P}(R') I_{\mathrm{PY}}(R_{\mathrm{t}_1}) - \hat{g}_\mathrm{P}(R') J_{\mathrm{PY}}(R_{\mathrm{t}_1}) \right) \mathrm{d}R' \\
& - \int_{R_{\mathrm{t}_1}}^{R_\mathrm{e}} \hat{g}_\mathrm{P}(R') V'_{\mathrm{PQ}}(R') \chi^-_\mathrm{Q}(R') \left(\sin\gamma I_{\mathrm{QY}}(R_{\mathrm{t}_1}) - \cos\gamma J_{\mathrm{QY}}(R_{\mathrm{t}_1}) \right) \mathrm{d}R' \qquad \text{(A.18a)} \\
J_{\mathrm{PY}}(R_\mathrm{e}) \approx & J_{\mathrm{PY}}(R_{\mathrm{t}_1}) - \int_{R_{\mathrm{t}_1}}^{R_\mathrm{e}} \hat{f}_\mathrm{P}(R') V'_{\mathrm{PP}}(R') \left(\hat{f}_\mathrm{P}(R') I_{\mathrm{PY}}(R_{\mathrm{t}_1}) - \hat{g}_\mathrm{P}(R') J_{\mathrm{PY}}(R_{\mathrm{t}_1}) \right) \mathrm{d}R' \\
& - \int_{R_{\mathrm{t}_1}}^{R_\mathrm{e}} \hat{f}_\mathrm{P}(R') V'_{\mathrm{PQ}}(R') \chi^-_\mathrm{Q}(R') \left(\sin\gamma I_{\mathrm{QY}}(R_{\mathrm{t}_1}) - \cos\gamma J_{\mathrm{QY}}(R_{\mathrm{t}_1}) \right) \mathrm{d}R' \qquad \text{(A.18b)} \\
I_{\mathrm{QY}}(R_\mathrm{e}) \approx & I_{\mathrm{QY}}(R_{\mathrm{t}_1}) - \cos\gamma \int_{R_{\mathrm{t}_1}}^{R_\mathrm{e}} \chi^-_\mathrm{Q}(R') V'_{\mathrm{QP}}(R') \left(\hat{f}_\mathrm{P}(R') I_{\mathrm{PY}}(R_{\mathrm{t}_1}) - \hat{g}_\mathrm{P}(R') J_{\mathrm{PY}}(R_{\mathrm{t}_1}) \right) \mathrm{d}R' \\
& - \cos\gamma \int_{R_{\mathrm{t}_1}}^{R_\mathrm{e}} \chi^-_\mathrm{Q}(R') V'_{\mathrm{QQ}}(R') \chi^-_\mathrm{Q}(R') \left(\sin\gamma I_{\mathrm{QY}}(R_{\mathrm{t}_1}) - \cos\gamma J_{\mathrm{QY}}(R_{\mathrm{t}_1}) \right) \mathrm{d}R' \qquad \text{(A.18c)} \\
J_{\mathrm{QY}}(R_\mathrm{e}) \approx & J_{\mathrm{QY}}(R_{\mathrm{t}_1}) - \sin\gamma \int_{R_{\mathrm{t}_1}}^{R_\mathrm{e}} \chi^-_\mathrm{Q}(R') V'_{\mathrm{QP}}(R') \left(\hat{f}_\mathrm{P}(R') I_{\mathrm{PY}}(R_{\mathrm{t}_1}) - \hat{g}_\mathrm{P}(R') J_{\mathrm{PY}}(R_{\mathrm{t}_1}) \right) \mathrm{d}R' \\
& - \sin\gamma \int_{R_{\mathrm{t}_1}}^{R_\mathrm{e}} \chi^-_\mathrm{Q}(R') V'_{\mathrm{QQ}}(R') \chi^-_\mathrm{Q}(R') \left(\sin\gamma I_{\mathrm{QY}}(R_{\mathrm{t}_1}) - \cos\gamma J_{\mathrm{QY}}(R_{\mathrm{t}_1}) \right) \mathrm{d}R', \qquad \text{(A.18d)}
\end{aligned}$$

where we have used equation (A.7a) to replace $X_{\mathrm{QY}}(R_{\mathrm{t}_1})$ with $\sin\gamma I_{\mathrm{QY}}(R_{\mathrm{t}_1}) - \cos\gamma J_{\mathrm{QY}}(R_{\mathrm{t}_1})$.

To simplify this result, we write the set of equations (A.18) in full matrix notation,

$$\begin{aligned}
I(R_\mathrm{e}) \approx & I(R_{\mathrm{t}_1}) - \int_{R_{\mathrm{t}_1}}^{R_\mathrm{e}} \begin{pmatrix} \hat{g}_\mathrm{P}(R') & 0 \\ 0 & \cos\gamma\chi^-_\mathrm{Q}(R') \end{pmatrix} V'(R') \begin{pmatrix} \hat{f}_\mathrm{P}(R') & 0 \\ 0 & \sin\gamma\chi^-_\mathrm{Q}(R') \end{pmatrix} I(R_{\mathrm{t}_1}) \mathrm{d}R' \\
& + \int_{R_{\mathrm{t}_1}}^{R_\mathrm{e}} \begin{pmatrix} \hat{g}_\mathrm{P}(R') & 0 \\ 0 & \cos\gamma\chi^-_\mathrm{Q}(R') \end{pmatrix} V'(R') \begin{pmatrix} \hat{g}_\mathrm{P}(R') & 0 \\ 0 & \cos\gamma\chi^-_\mathrm{Q}(R') \end{pmatrix} J(R_{\mathrm{t}_1}) \mathrm{d}R' \qquad \text{(A.19a)} \\
J(R_\mathrm{e}) \approx & J(R_{\mathrm{t}_1}) - \int_{R_{\mathrm{t}_1}}^{R_\mathrm{e}} \begin{pmatrix} \hat{f}_\mathrm{P}(R') & 0 \\ 0 & \sin\gamma\chi^-_\mathrm{Q}(R') \end{pmatrix} V'(R') \begin{pmatrix} \hat{f}_\mathrm{P}(R') & 0 \\ 0 & \sin\gamma\chi^-_\mathrm{Q}(R') \end{pmatrix} I(R_{\mathrm{t}_1}) \mathrm{d}R' \\
& + \int_{R_{\mathrm{t}_1}}^{R_\mathrm{e}} \begin{pmatrix} \hat{f}_\mathrm{P}(R') & 0 \\ 0 & \sin\gamma\chi^-_\mathrm{Q}(R') \end{pmatrix} V'(R') \begin{pmatrix} \hat{g}_\mathrm{P}(R') & 0 \\ 0 & \cos\gamma\chi^-_\mathrm{Q}(R') \end{pmatrix} J(R_{\mathrm{t}_1}) \mathrm{d}R'. \qquad \text{(A.19b)}
\end{aligned}$$

These equations involve integrals that contain the open-channel wave functions $\hat{f}_\mathrm{P}(R')$ and $\hat{g}_\mathrm{P}(R')$ and the physically acceptable closed-channel wave function $\chi^-_\mathrm{Q}(R')$. The exponentially divergent wave function $\chi^+_\mathrm{Q}(R')$ does not appear in these expressions for $I(R_\mathrm{e})$ and $J(R_\mathrm{e})$.

We approximate $K^{\mathrm{sr}'}$ by directly substituting the expressions for the coefficients $I(R_{\mathrm{e}})$ and $J(R_{\mathrm{e}})$ in the set of equations (A.19) into the equation $K^{\mathrm{sr}'} = J(R_{\mathrm{e}})I(R_{\mathrm{e}})^{-1}$ and by only keeping terms that are first-order in $V'(R)$. We define the first-order quantities ΔI and ΔJ below,

$$\Delta I = I(R_{\mathrm{e}}) - I(R_{\mathrm{t}_1}) \tag{A.20a}$$

$$\Delta J = J(R_{\mathrm{e}}) - J(R_{\mathrm{t}_1}). \tag{A.20b}$$

We assume that $\Delta I << I(R_{\mathrm{t}_1})$, and we make the following approximations,

$$\begin{aligned} K^{\mathrm{sr}'} &= \left(J(R_{\mathrm{t}_1}) + \Delta J\right)\left(I(R_{\mathrm{t}_1}) + \Delta I\right)^{-1} \\ &\approx \left(J(R_{\mathrm{t}_1}) + \Delta J\right)\left(I^{-1}(R_{\mathrm{t}_1}) - I^{-1}(R_{\mathrm{t}_1})\Delta I I^{-1}(R_{\mathrm{t}_1})\right) \qquad \text{(A.21a)} \\ &\approx \mathcal{K}(R_{\mathrm{t}_1}) - \mathcal{K}(R_{\mathrm{t}_1})\Delta I I^{-1}(R_{\mathrm{t}_1}) + \Delta J I^{-1}(R_{\mathrm{t}_1}). \qquad \text{(A.21b)} \end{aligned}$$

By replacing $-\Delta I$ and $-\Delta J$ in equation (A.21b) by the integrals on the right hand side of the set of equations (A.19) for which they stand, we produce the following approximation for $K^{\mathrm{sr}'}$,

$$\begin{aligned} K^{\mathrm{sr}'} \approx &\mathcal{K}(R_{\mathrm{t}_1}) - \int_{R_{\mathrm{t}_1}}^{R_{\mathrm{e}}} \begin{pmatrix} \hat{f}_{\mathrm{P}}(R') & 0 \\ 0 & \sin\gamma\chi_{\mathrm{Q}}^{-}(R') \end{pmatrix} V'(R') \begin{pmatrix} \hat{f}_{\mathrm{P}}(R') & 0 \\ 0 & \sin\gamma\chi_{\mathrm{Q}}^{-}(R') \end{pmatrix} \mathrm{d}R' \\ &+ \int_{R_{\mathrm{t}_1}}^{R_{\mathrm{e}}} \begin{pmatrix} \hat{f}_{\mathrm{P}}(R') & 0 \\ 0 & \sin\gamma\chi_{\mathrm{Q}}^{-}(R') \end{pmatrix} V'(R') \begin{pmatrix} \hat{g}_{\mathrm{P}}(R') & 0 \\ 0 & \cos\gamma\chi_{\mathrm{Q}}^{-}(R') \end{pmatrix} \mathcal{K}(R_{\mathrm{t}_1})\mathrm{d}R' \\ &+ \mathcal{K}(R_{\mathrm{t}_1}) \int_{R_{\mathrm{t}_1}}^{R_{\mathrm{e}}} \begin{pmatrix} \hat{g}_{\mathrm{P}}(R') & 0 \\ 0 & \cos\gamma\chi_{\mathrm{Q}}^{-}(R') \end{pmatrix} V'(R') \begin{pmatrix} \hat{f}_{\mathrm{P}}(R') & 0 \\ 0 & \sin\gamma\chi_{\mathrm{Q}}^{-}(R') \end{pmatrix} \mathrm{d}R' \\ &- \mathcal{K}(R_{\mathrm{t}_1}) \int_{R_{\mathrm{t}_1}}^{R_{\mathrm{e}}} \begin{pmatrix} \hat{g}_{\mathrm{P}}(R') & 0 \\ 0 & \cos\gamma\chi_{\mathrm{Q}}^{-}(R') \end{pmatrix} V'(R') \begin{pmatrix} \hat{g}_{\mathrm{P}}(R') & 0 \\ 0 & \cos\gamma\chi_{\mathrm{Q}}^{-}(R') \end{pmatrix} \mathcal{K}(R_{\mathrm{t}_1})\mathrm{d}R' \end{aligned} \tag{A.22a}$$

$$\begin{aligned} =&\mathcal{K}(R_{\mathrm{t}_1}) - \int_{R_{\mathrm{t}_1}}^{R_{\mathrm{e}}} \begin{pmatrix} \hat{f}_{\mathrm{P}}(R') - \hat{g}_{\mathrm{P}}(R')\mathcal{K}_{\mathrm{PP}}(R_{\mathrm{t}_1}) & -\hat{g}_{\mathrm{P}}(R')\mathcal{K}_{\mathrm{PQ}}(R_{\mathrm{t}_1}) \\ -\chi_{\mathrm{Q}}^{-}(R')\cos\gamma\mathcal{K}_{\mathrm{QP}}(R_{\mathrm{t}_1}) & \chi_{\mathrm{Q}}^{-}(R')\left(\sin\gamma - \cos\gamma\mathcal{K}_{\mathrm{QQ}}(R_{\mathrm{t}_1})\right) \end{pmatrix}^{T} \\ &\times V'(R) \begin{pmatrix} \hat{f}_{\mathrm{P}}(R') - \hat{g}_{\mathrm{P}}(R')\mathcal{K}_{\mathrm{PP}}(R_{\mathrm{t}_1}) & -\hat{g}_{\mathrm{P}}(R')\mathcal{K}_{\mathrm{PQ}}(R_{\mathrm{t}_1}) \\ -\chi_{\mathrm{Q}}^{-}(R')\cos\gamma\mathcal{K}_{\mathrm{QP}}(R_{\mathrm{t}_1}) & \chi_{\mathrm{Q}}^{-}(R')\left(\sin\gamma - \cos\gamma\mathcal{K}_{\mathrm{QQ}}(R_{\mathrm{t}_1})\right) \end{pmatrix} \mathrm{d}R'. \end{aligned} \tag{A.22b}$$

From equation (A.22b) we see that this approximation to $K^{\mathrm{sr}'}$ is symmetric.

To ease the implementation of this approximation to $K^{\mathrm{sr}'}$, we approximate $\mathcal{K}(R_{\mathrm{t}_1})$ by K^{sr} inside the integral on the right hand side of the set of equations (A.22). Even though this approximation may be less accurate than the approximation to $K^{\mathrm{sr}'}$ in the set of equations (A.22), the difference is small when $\mathcal{K}(R_{\mathrm{t}_1}) \approx K^{\mathrm{sr}}$. Hence, we identify a physically reasonable perturbation expansion for $K^{\mathrm{sr}'}$ in terms of the wave function matrix $\tilde{M}^{(0)}(R)$,

$$\tilde{M}^{(0)}(R) = \begin{pmatrix} \hat{f}_{\mathrm{P}}(R) - \hat{g}_{\mathrm{P}}(R) K^{\mathrm{sr}}_{\mathrm{PP}} & -\hat{g}_{\mathrm{P}}(R) K^{\mathrm{sr}}_{\mathrm{PQ}} \\ -\chi^{-}_{\mathrm{Q}}(R) \cos\gamma K^{\mathrm{sr}}_{\mathrm{QP}} & \chi^{-}_{\mathrm{Q}}(R) \left(\sin\gamma - \cos\gamma K^{\mathrm{sr}}_{\mathrm{QQ}} \right) \end{pmatrix} \tag{A.23}$$

In terms of $\tilde{M}^{(0)}(R')$, we write the final approximation to $K^{\mathrm{sr}'}$,

$$K^{\mathrm{sr}'} \approx \mathcal{K}(R_{\mathrm{t}_1}) - \int_{R_{\mathrm{t}_1}}^{R_{\mathrm{e}}} \tilde{M}^{(0)T}(R') V'(R') \tilde{M}^{(0)}(R') \mathrm{d}R'. \tag{A.24}$$